Title

Novel Single Atom Catalysts (SACs) Design Based on First Principles

Author

Xiong, Chuanye

Publication Date

2023

UNIVERSITY OF CALIFORNIA
RIVERSIDE

Novel Single-Atom Catalysts (SACs) Design Based on First Principles

A Dissertation submitted in partial satisfaction
of the requirements for the degree of

Doctor of Philosophy

In

Chemical and Environmental Engineering

by

Chuanye Xiong

June 2024

Dissertation Committee:
Dr. De-en Jiang, Chairperson
Dr. Jianzhong Wu
Dr. Kandis Leslie Abdul-Aziz

The Dissertation of Chuanye Xiong is approved:

____

____

____

Committee Chairperson

University of California, Riverside

COPYRIGHT ACKNOWLEDGEMENT

The text and figures in Chapter 3, in part or full, are a reprint of the material as it appears in “Single-Atoms Anchored in Hexagonal Boron Nitride for Propane Dehydrogenation from First Principles”, ***ChemCatChem*, 14(9), e202200133** by Chuanye Xiong, Prof. Sheng Dai, Dr. Zili Wu and Prof. De-en Jiang. The coauthor (Dr. De-en Jiang) listed in that publication directed and supervised the research that forms the basis of this chapter.

The text and figures in Chapter 4, in part or full, are a reprint of the material as it appears in “First-Principles investigation of the Stability and CH_4 activation capability of defective h-BN”, **(*In preparation*)** by Chuanye Xiong and Prof. De-en Jiang. The coauthor (Dr. De-en Jiang) listed in that publication directed and supervised the research that forms the basis of this chapter.

The text and figures in Chapter 5, in part or full, are a reprint of the material as it appears in “Selective Formation of Acetic Acid and Methanol by Direct Methane Oxidation Using Rhodium Single-Atom Catalysts”, ***J. Am. Chem. Soc.* 2023, 145, 20, 11415–11419** by Haoyi Li, Chuanye Xiong, Muchun Fei, Lu Ma, Hongna Zhang, Xingxu Yan, Peter Tieu, Yucheng Yuan, Yuhan Zhang, James Nyakuchena, Jier Huang, Xiaoqing Pan, Matthias M. Waegele, De-en Jiang*, and Dunwei Wang*. The coauthor (Dr. Dunwei Wang and Dr. De-en Jiang) listed in that publication directed and supervised the research that forms the basis of this chapter.

ACKNOWLEDGMENTS

It really took me a long time before I could write the first opening word for this section. Pursuing a Ph.D. is a long voyage, and I can’t help but close my eyes and savor every precious moment along the way. Indeed, memories are priceless, but even more precious are the people who have helped me throughout this journey. I cannot begin to express my earnest appreciation for everyone along with me.

To start with, I owe a tremendous debt of gratitude to my advisor, Prof. De-en Jiang, for his unwavering guidance and support to me. Thanks to the nurturing academic atmosphere created by my advisor, my passion for computational chemistry has dramatically deepened, leading me to conduct research with strong motivation. Pursuing the truth is like finding a needle in the haystack. Prof. Jiang served as my lighthouse through this long journey and always guided me in the right direction. Again, I would like to extend my heartfelt gratitude for your solid support over the past years.

Furthermore, it’s also my pleasure to thank Prof. Kandis Leslie Abdul-Aziz and Prof. Jianzhong Wu. Serving as my committee members, they provided invaluable suggestions for my research project and helped greatly improve the quality of my thesis. I could still vividly recall the moments when Prof. Abdul-Aziz instructed me in the experimental techniques for synthesizing and characterizing the catalysts in the group meeting. Still, in the Advanced Chemical Engineering thermodynamics class, Prof. Jianzhong Wu spared no efforts in teaching us thermodynamics theories and this knowledge fortifies my foundation background as a simulation and modeling researcher. Prof. Wu always can explain the complicated quantum chemistry equations in an easy-to-understand way.

Secondly, I would like to express my profound appreciation to everyone in the Computational Chemical Sciences and Materials Laboratory. Your dedication and commitment dramatically helped me on my research project and fostered the growth of my research interests. I wish to thank Dr. Song Wang and Prof. Victor Fung for teaching me the basic knowledge of machine learning assisted catalyst design. I also would like to thank Dr. Lihua Xu and Dr. Yangyunli Sun for teaching me coding and programming skills. Still, I would like to thank Dr. Tongyu Liu for instructing me in using TURBOMOLE software. Moreover, I would like to express my gratitude to Yuqing Fu for her generous assistance for my Teaching Assignment. Furthermore, A special appreciation to Dr. Tao Wu and Dr. Lu Wang for taking care of me after I did the medical surgery. Without your help, my recovery process wouldn't have been smooth, and I wouldn't have returned to work on time. Also, I wish to extend my heartfelt thanks to all my group members for your kind support and your patience in addressing all my questions and concerns during this journey.

Thirdly, I wish to thank Dr. Haoyi Li, Dr. Xiang Li and Prof. Dunwei Wang for your insightful suggestions from experimental aspect, which facilitate my understanding for the MOF catalysts. Moreover, I would like to appreciate for Dr. Zhenzhen Yang, Dr. Hao Chen, Dr. Aditya Savara, and Prof. Sheng Dai from Surface Chemistry and Catalysis Group in Oak Ridge National Lab for your unwavering commitment to helping me finish the project regarding to the Boron Nitride catalyst design. In a nutshell, I'm deeply appreciative of all my collaborators who have stood by me and supported me in these years.

Fourthly, I wish to extend my heartfelt gratitude to the National Science Foundation (NSF), Department of Energy (DOE) office of Office of Science User Facility, and the University of California, Riverside for their funding support. Furthermore, I would like to convey my profound appreciation to High-Performance Computing Center (HPCC) at UCR and the National Energy Research Scientific Computing Center (NERSC) for the computational resources support.

My deepest gratitude goes out to my parents. Life has ups and downs. Their consistent love and backing have been supporting me to finish my Ph.D. Finally, I would thank everyone who accompanied me and helped me along this long journey.

ABSTRACT OF THE DISSERTATION

Novel Single-Atom Catalysts (SACs) Design Based on First Principles

by

Chuanye Xiong

Doctor of Philosophy, Graduate Program in Chemical and Environmental Engineering
University of California, Riverside, December 2023
Dr. De-en Jiang, Chairperson

The development of Single-Atom Catalysts (SACs) is a milestone in the catalysis industry. SACs usually have unique electronic properties and ultrahigh reactivity for chemical reactions. The Turnover frequency (TOF) values of SACs are generally much larger than that of regular nanoparticle catalyst. However, due to the high surface energy of the SACs, the aggregation effect restrains the researchers from further increasing the loading of the Single-Atoms on the supports. The aggregation, unlike coking which could be easily solved by reoxidation of the catalyst, is irreversible and would also lead to the deactivation of the catalyst. This conundrum prevents the implementation of SACs in industrial usage. To solve this problem, scientists usually leverage the Strong Metal-Support interaction (SIMI) effect to anchor the Single-Atoms by the defect sites on the support (e.g., vacancies, hydroxyl group). In this dissertation, the first part of our work is to conduct the rational design of the SACs on the 2-dimensional (2D) hexagonal boron nitride (h-BN) material. We assessed the possibility of noble metals Ru, Pt, and Au loaded on h-BN as SACs from three aspects (i.e., stability, activity, and selectivity). Both *ab initio* Molecular Dynamics (AIMD) simulations and anchoring energy calculations suggested that Au is not stable over the defect sites of h-BN. From the reaction energy plot of the propane dehydrogenation (PDH), we found that the Pt over B vacancy and Ru over N vacancy are promising for PDH reactions with low dehydrogenation barriers. We also noticed that there is a trade-off for the C-H bond activation and C_3H_6 desorption. This trade-off relationship let the researchers make a compromise between the activity and selectivity when conducting the catalyst design. The second part of this thesis focuses on the activity of the defect sites of the h-BN, we selected a set of vacancy sites with different sizes. From the defect formation energy calculations, we found that the normalized formation energy decreases with the increase of defect size. Also, we probed the CH_4 activation over these vacancies and we found that the B-B pair over the N vacancy and B-N pair over the BN_2 vacancy have excellent reactivity for CH_4 activation. The third part of our work is to examine the activity and selectivity of CH_4 oxidation to acetic acid over Single-Atom Rh dispersed Porphyrin-based Metal Organic Framework (pMOF) catalyst. We found that the Rh in-plane model favors the CH_3OH formation while the Rh out-of-plane model favors the CH_3COOH formation. This thesis gives the interpretation of the reaction mechanism of Single-Atom catalysts over h-BN and pMOF catalysts.

TABLE OF CONTENTS

LIST OF FIGURES

LIST OF TABLES

Chapter 1. Introduction

1.1 Single-Atom catalyst

At present, with the increasingly rapid development of the catalyst industry, researchers gradually focus on the molecular-level catalysis, aiming at fine-tuning the structure-performance relationships of the catalysis and achieving better economic effectiveness. The development of Single-Atom catalysts (SAC) is a milestone along the way of probing molecular-level catalysis. The concept of the Single-Atom catalysis was first put forward by Dr. Tao Zhang in 2011 when they successfully anchored the Single-Atom Pt over the iron oxide[1]. Single-Atom catalyst usually exhibits significantly higher Turnover Frequency (TOF) than the nanoparticles[2, 3]. Still, SAC could achieve 100% atom efficiency in that each atom of the catalysts plays a vital important role in the reaction. The atomic efficiency is crucial for developing noble metal catalyst like Pt[4], Au[5] and Ru[6] owing to the high cost when synthesizing the catalyst. Achieving isolated dispersion not only reduces the loading of the previous metal but also maximizes the potential catalytic performance of each active site. The high ultrahigh activity of the SAC is attributed to the exposure of every active atom to the reactants and the unique electronic properties due to the quantum confinement effect which could lead to the higher energy level and larger band gap[7,8]. At present, the SAC has been broadly utilized in the hydrocarbon hydrogenation/dehydration reactions[9-11], water splitting reactions (i.e., HER and OER)[12, 13], selective oxidation reactions[14, 15], etc.

Owing to the high surface energy of SAC metals compared to metal clusters[16], the migration and aggregation of the Single-Atom metals are common issues especially at high temperatures. Unlike coking[17], which is reversible and could be resolved by thermal regeneration of the catalysts. Catalysts aggregation is irreversible and leads to deactivation of the catalysts. To tackle the aggregation issue, researchers leveraged Strong Metal-Support Interaction (SMSI) to anchor the Single-Atoms by the defects site of the support[18-20]. Although defect site greatly facilitate the stabilization of Single-Atom, researchers still found the reducible iron oxide could also stabilize the isolated Pt via the Strong Covalent Metal-support Interaction (CMSI) without defect[21]. In this section we will briefly talk about the Single-Atom supported by metals, metal oxides, 2 dimensional materials and Metal-organic Frameworks (MOFs).

1.1.1 Single-Atom catalysts over metals

Single-Atom metals dispersed on other metals or Single-Atom alloys have attracted the attention of the academia as a result of their higher stability, induced by strong metal-metal interaction, compared to Single-Atoms dispersed on other supports[22]. The Single-Atoms are generally stabilized over the step sites or grain boundaries of the hosting metals[22]. So far, Single-Atom alloys have been extensively investigated including Pt/Cu[23], Pd/Cu[24], Pt/Ag[25] and cheap metal alloy Ni/Cu[26]. In 2018, Dr. Maria Flytzani-Stephanopoulos collaborated with Dr. Michail Stamatakis and Dr. E. Charles Sykes and developed Pt/Cu Single-Atom alloy catalyst which can reduce the coke formation for methane and butane activation reaction, Density functional Theory (DFT) simulations also found that Pt/Cu Single-Atom alloy model would suppress the deep dehydrogenation step with higher barrier compared with Pt (111) surface[23]. Moreover, Dr. Gong's group developed the Pt/Cu Single-Atom alloy via co-impregnation method by mixing Pt precursor with Cu precursor, and their catalysts possesses excellent C-H bond activation capabilities and prevents selectivity by suppressing the deep dehydrogenation reaction. Their SAC breaks the trade-off relationship between the catalytic activity and the selectivity[27].

1.1.2 Single-Atom catalysts over metal oxides

Metal oxides are one of the most prevalent supports for dispersing Single-Atoms owing to the fact that metal oxides have complex surface structures. The steps sites, vacancies, surface hydroxyl groups over metal oxides can be utilized to anchor the Single-Atoms[28]. Furthermore, some properties of the metal oxides (e.g., surface acidity/basicity, crystalline phase) are easy to be tuned in the catalyst preparation process, the interactions between the metal and support could be manipulated by these tunable properties as well. Currently, SAC supported by reducible oxides are most widely investigated owing to the abundant vacancies existing on the surface. Dr. Roger Rousseau and Dr. Zdenek Dohnálek found that the iron vacancies in the reconstructed Fe_3O_4(001) surface which are the ideal spots for anchoring isolated Pd atoms[29]. Researchers also found that the defects on the FeO_x could anchor the isolated Pt atoms and the Single-Atom Pt/FeO_x catalyst has high performance on CO oxidation[1] and NO reduction[30] reactions. CeO_2 is another popular reducible metal oxide support for dispersing the Single-Atoms due to its high vacancy density. Dr. Emiel J. M. Hensen's group developed Single-Atom Pd catalyst dispersed on CeO_2 (111) and found the catalyst is highly active for low-temperature CO oxidation[31]. By utilizing DFT calculations, Dr. Qingfeng Ge also found that Single-Atom doped CeO_2 catalyst has promising performance on acetic acid formation via direct C-C coupling by the insertion of CO_2[32]. Moreover, many other metals like Pt[33], Ru[34], Rh[35], Cu[36] dispersed on CeO_2 support have been widely studied in recent years. As a superstar semiconductor material used in electrochemistry and photochemistry, TiO_2 also serves as a prototype for anchoring Single-Atoms. Dr. Gianfranco Pacchioni unveiled the atomistic property of Pt Single-Atom dispersed on TiO_2 surface by combining experimental characterizations with DFT simulations[37]. Apart from noble metal, some cheap metals (e.g., Fe[38], V[39]) were also developed as the Single-Atom catalysts dispersed on TiO_2.

1.1.3 Single-Atom catalysts over 2 dimensional materials

2-dimensional (2D) materials have been brought to the attention of the research community since the discovery and rise of the graphene[40]. Serving as the exemplary model catalyst, Single-Atom dispersed on 2D materials have been extensively investigated by the scientists. In this section, we will briefly talk about SAC over graphene, MoS_2 and hexagonal boron nitride (h-BN). As the most well-known 2D material, graphene has been utilized in electronic devices[41], energy storage[42] and catalysis[43] thanks to its amazing electronic conductivity, elasticity and flexibility. At present, Atomic layer deposition (ALD)[44], Electroplating deposition[45] and Iced-photochemical reduction[46] are three major methods to load Single-Atoms over graphene. The Single-Atoms dispersed over graphene are mostly studied as electrocatalysts[47] owing to the relatively low reaction temperature compared to thermal catalysts, which would extensively avoid the migration and aggregation of the Single-Atoms. Theoretical works have investigated the metal anchored on pristine graphene[48, 49] (i.e., the bridge, top and hollow sites of the pristine graphene), the defects of graphene[50] and decorated graphene[51]. The pristine graphene is not capable of anchoring Single-Atom metals compared to the graphene with defects sites (i.e., vacancies, nonmetal atom decorations) owing to the relatively weak non-covalent bond between Single-Atom metal and graphene[52]. A group of researchers (Dr. Xianghua Kong, Dr. Xiaojun Wu and Dr. Hengxing Ji, etc.) developed the Co SAC dispersed on nitrogen-doped graphene (Co-N/G)[53]. By combining the experimental characterization and DFT simulations, they found that the Co-N-C local structure serves as the active site for both Li_2S formation and breakdown reactions, greatly promoting the efficiency of the electrode. Molybdenum Disulfide (MoS_2) is another prevalent 2D material for supporting Single-Atoms owing to its 3-layer sandwich-like structure, which introduced more options for anchoring sites of Single-Atoms. Dr. Jingyue Liu’s group, in collaboration with Dr. Kyeongjae Cho’s group, successfully synthesized the Single-Atom Rh_1/MoS_2 catalyst[54] by the adsorption method[55]. By utilizing HAADF-STEM techniques, EXAFS characterizations, and DFT simulations, they found that the Rh Single-Atoms are anchored on the edge sites of the MoS_2 substituting Mo atom sites[54]. Via assessing the catalytic performance of Crotonaldehyde Hydrogenation reaction, they observed that their Rh_1/MoS_2 catalyst can achieve 100% selectivity towards crotyl alcohol formation[54]. In recent years, the utilization of hexagonal boron nitride (h-BN) has attracted the attention of researchers because of its high thermal stability compared to graphene. Theoretical simulations have been applied to probe the possibility of Single-Atom doped h-BN for electrochemistry reaction (i.e., Electrochemical Nitrogen Fixation[56]) and thermal catalytic reaction (i.e., CO oxidation[57]). Recently, Dr. Denis V. Leybo's group developed the Single-Atom Fe_1/h-BN catalyst by using phthalocyanine as the precursor, and they found the catalyst has great potential for CO_2 hydrogenation reaction[58].

1.1.4 Single-Atom catalysts over the Metal Organic Frameworks

Metal Organic Frameworks (MOFs) materials are promising candidates for catalytic reactions due to its large specific surface area and amorphous structure, which provides numerous sites for functionalization[59]. The basicity and acidity of the MOFs catalysts could be easily tuned by the preparation methods. Dr. Suojiang Zhang's group developed the acidic UiO-67 type MOFs by introducing bipyridyl nitrogen, and they found that the strong acidic active sites facilitate the esterification reaction[60]. Their achieved conversion rate of isooctyl alcohol is as high as 85%[60]. In terms of the basic sites in MOF catalysts, they can originate not only from the intrinsic metal sites or ligands but also from subsequent functional decorations[59]. MOFs consist of nodes and linkers. The metal sites located at the nodes could be functionalized by the amine groups[61, 62], which contribute to the formation of basic active sites. The ligand located at the linkers could also be functionalized via the direct amination process. Dr. Norbert Stock's group developed the direct amination method of Cr-MIL-101–NO_2 by conducting the hydrothermal reaction between nitroterephthalic acid and $CrCl_3$[63]. Due to the limited categories of functional groups of the direct functionalization methods, Post-Synthetic Modification (PSM) became more and more popular in recent years. Dr. Andrew D. Burrows's group utilized the one-step sulfur oxidation for the PSM of the IRMOF-9[64].

Owing to the tunable properties and the well-defined spatial structure of MOFs, more and more researchers began to probe the feasibility of SACs stabilized by MOFs. Dr. Yadong Li's group leveraged the pyrolysis process and synthesized the Zn/Co MOFs materials[65]. By combining Extended X-ray Absorption Fine Structure (EXAFS) and spherical aberration correct high-angle annular dark-field scanning transmission electron microscope (HAADF-STEM), they found that Co atoms are truly isolated dispersed on the N-doped carbon skeleton over the linkers[65]. Also, the authors found the Co single sites have comparable performance with state-of-art commercial Pt/C catalyst for ORR reaction[65]. Dr. Jiang's group also found that the porphyrin structures located at linker positions in Al-TCPP could effectively anchor the Single-Atom Pt, and their catalysts can achieve ultrahigh TOF values, which is 30 times higher than the TOF of Pt nanoparticle catalysts[66]. Apart from the linkers, the SACs can also be dispersed over the metal node structures on the MOF. A group of researchers (Dr. Christopher J. Cramer, Dr. Laura Gagliardi, Dr. Joseph T. Hupp and Dr. Omar K. Farha) leveraged the atomic layer deposition method to introduce the Single-Atom Ni on the Zr-based nodes MOF and the catalyst has great stability against sintering in the ethylene hydrogenation reaction[67,68].

1.2 Computational Catalyst Design

The Computational Catalyst Design refers to the field of probing the mechanism of chemical reactions and designing the catalysis with high activity, selectivity, and stability by combining the Density Functional Theory[69], Molecular dynamics[70], and Combined Quantum Mechanical/Molecular mechanics methods (QM/MM)[71]. It’s an interdisciplinary research field merging Computer Science, Chemical Reaction Engineering and Quantum Chemistry. Without the help of the computational catalyst design, even if the cutting-edge characterization methods (i.e., STM, EXAFS, HAADF-STEM) could not assist human fully understand the chemistry reaction mechanism and the molecular level structural changes of the catalyst with the reaction time on stream. In this section, we will break down the whole discussion into the following parts: (1) State-Of-Art prevalent Computational Catalyst models. (2) Procedures for the computational catalyst design. (3) Finding the descriptors for boosting catalyst design.

1.2.1 State-of-Art prevalent Computational Catalyst models

Bulk and slab models.

Bulk and slab models are generally utilized to represent the heterogeneous catalysts (e.g., Crystals). These models have repetitive structures and when software conducting the calculation on these models, the periodic boundary conditions are implemented for simplifying the calculation process. The periodic models can be divided into bulk models[72] and surface slab models[73].

The bulk models refer to the bulk phase of the materials which are repetitive along the x, y and z directions in the 3-dimensional coordination system. As for the metals bulk phase, there are three most common types of crystalline structures discovered in metals: (1) Body-Centered Cubic (BCC)[74]. In this structure, all the eight atoms are located at the 8 conners of the cube, which is a unit cell, and one atom is located at the center of the cube. (2) Face-Centered Cubic (FCC)[75]. In this structure, 8 atoms are located at each of the corners and 6 atoms are located at the centers of each cube face. (3) Hexagonal Close-Packed (HCP)[76]. In this structure, the basic unit cell is a hexagon rather than cubic. 6 atoms are located at each of the corners of the hexagon and one additional atom is in the middle. The HCP structure is packed layer by layer with close packing. The bulk structures of metal oxides are much more complex compared to pure metals or metal alloys. Some metal oxides may occur phase transitions under certain conditions. The titanium oxide has two common phases[77]: (a) Rutile phase, which is stable at high temperatures; (b) Anatase phase, which is a sub stable phase. The properties (e.g., band gap, lattice constant, reactivity, etc.) of these two phases significantly differ from each other[77, 78]. The perovskite material (ABO_3) series are another complex metal oxide series, the physical/electronical properties of these materials vary significantly with the changing of the A/B sites of the metals and the doping effects[79, 80]. Amorphous materials could also be represented by the period bulk model, Dr. Gong's group leveraged the periodic bulk model to simulated the substance diffusion in the tunnels of sodalite zeolite (SOD)[81]. Also, Dr. Mathieu Digne collaborated with Dr. Philippe Sautet built the γ-Al_2O_3 bulk phase super cell by stacking 8 Al_2O_3 units[82].

The surface slab models are utilized to represent the surface of the materials, which typically represent the catalyst surfaces in computational catalysis. Similar to the bulk models, the metal surfaces are simpler than that of metal oxides. The slab models are generally achieved by cleaving the bulk models along certain direction of the plane. As for transitional metals, (111) surfaces are the most well-known surface for simulating surface reactions. (e.g., propane dehydrogenation[83], acetylene hydrogenation[84], Fischer–Tropsch reaction[85], etc.). (211) surfaces are believed to have high activity for surface reactions owing to the existence of the coordinatively unsaturated atoms over the edge/step sites of the (211) surfaces[86]. In terms of metal oxides, the surface conditions are more complicated than that of metals. The hydroxyl groups (-OH) on metal oxides could tune the surface properties of metal oxides[87]. Moreover, the oxygen vacancies are crucial for conducting the chemical loop related reactions[88, 89]. Therefore, when simulating the metal oxides surface, it's of vital importance to consider the effects of hydroxyl group coverages[90] and oxygen vacancy coverages[91] on the performance of the catalysts when illuminating the reaction mechanism.

Cluster Models

Cluster models are generally utilized to represent nano particles or molecules. In contrast to the bulk models or surfaces models, cluster models generally are isolated systems, and they are usually surrounded by the gas phase. As for the nanoparticles, the properties of the nanoparticles greatly depend on the size of the particles. Dr. Jens K. Nørskov's group built a series of Pt cluster models, comprising 13 to 1415 Pt atoms, to simulate nanoparticles of varying sizes with diameters ranging from 0.7nm to 3.5nm. They found that with the increase of the particle size, the properties (i.e., adsorption energy, density of states) converge towards the values observed in slab surfaces (i.e., 211 surface, 111 surface). They also found that the critical particle size for Pt is around 1.6 nm; below this size, the properties of the particles begin to diverge from those of the surface, while the critical particle size for Au is 2.7nm[92, 93]. Moreover, researchers also utilized cluster models to simulate the metal oxides, Dr. Elena Jakubikova conducted the Gaussian simulations on small V_xO_y clusters and found that cyclic and cage-like structures are preferred by the isomer vanadium oxide owing to the lower energy[94]. Also, some other scientists leveraged the $[(\equiv Si—O)_3V^{III}(OH_2)]$ models to represent the vanadium oxides supported on Silica catalyst[95]. In their work, they illuminated the Mars–van Krevelen mechanism for light alcohol partial oxidation reactions. Furthermore, the cluster models are also widely used in the enzyme reactions as biocatalysts[96]. Dr. Klaus E. Hermann's group utilized the density functional theory calculations to study the geometric and electronic properties of $K[VO(O_2)Hheida]$ complex. They found that there is no strong covalent bond between K and $[VO(O_2)Hheida]$, while the K exists as caption to balance out the negative charge of $(VO(O_2)Hheida)^-$. Also, their calculated O 1s excitation spectra are consistent with the experimental characterization results, which validates the correctness of their models[97]. Still, Dr. Fahmi Himo, with Polina Georgieva, probed the methyl transfer reaction catalyzed by the lysine methyltransferase (HKMT) SET7/9 enzyme, and their calculated energy barrier is very close to the experimental results[98].

1.2.2 Procedures for the computational catalyst design.

The targets of the computational catalysis can be divided into two aspects from a high-level perspective: (1) Assisting the experiments to understand the behaviors and mechanisms of chemical reactions at atomic level; (2) To build-up the intrinsic structural relationships of the catalysts for rational design of the catalysts. The computational catalyst design is based on the sufficient understanding of the properties of the catalysts surface and the reaction mechanisms. In this part we generally talk about the technical procedures for conducting the computational catalyst design[99]:

(1) The first step is to choose the catalyst system (e.g., metal catalysts, metal oxides catalysts, enzyme catalysts) based on the industrial requirements. Furthermore, we would need to build catalyst models for representing the catalysts. Although the real structural condition for catalysts is extremely complicated, computational

scientists still can make some implications to simulate the catalyst under ideal conditions to focus mainly on the reactions over the active sites. The state-of-art prevalent models for representing catalysts consists of surface slab model, bulk model, and cluster model. Consider the capability of the modern computers, the model consists of less than 200 atoms are tolerable when conducting the DFT and ab *initio* Molecular dynamics (AIMD)[100] calculations.

(2) After we figured out the models for the catalyst, we would conduct thermal dynamics calculations to figure out the surface conditions of the catalysts. Dr. Jiang’s group utilized the surface diagram to find the stable surface terminations for Perovskite Oxyhydride materials by calculating the Surface Grand potential (SGP)[101]. In this step, it’s necessary to validate the surface model by making comparisons with experimental studies. For example, by comparing the CO vibration frequencies over the surface with the experimental diffuse reflectance infrared Fourier transform spectroscopy (CO-DRIFTS) would validate the actual existence of the active sites represented by simulation models[102].

(3) The third step is to investigate the reaction pathways by simulating each elementary step, which includes the initial state, transitional state, and final state along with the reaction coordinate. By combining all the reaction pathways for all possible reactants, intermediates, products, we could map out the reaction networks. The reaction networks generally consist of the pathways to the desired products, side products. Based on the information obtained from the reaction

networks, we can illuminate the reaction mechanisms and conduct some basic analysis of the modification methods to improve the performance of the catalysts. Dr. Joachim Sauer's group constructed the reaction network for propane dehydrogenation reactions over monomeric vanadium oxides supported on silica, based on the analysis toward the reaction network, they found that the peroxovanadate local structure is the main contributor for the overoxidation reactions, which would reduce the selectivity of the propylene[103].

(4) On the condition that the reaction energy plot has been obtained, the micro-kinetic studies[104, 105] are supposed to be conducted for getting the reaction rate and selectivity. Also, we could carry out the sensitivity analysis by leveraging the Degree of Rate Control method (DRC). By utilizing these results, we can directly compare with the experiments values and guide the catalyst design.

(5) The last step is to find descriptors based on the understanding we've obtained from the catalysts simulations. The descriptors are mainly used to determine the properties that are expensive or time-consuming for computational or experimental methods to achieve by the relatively cheap properties which could be easily get. The decent descriptors would greatly boost the prediction accuracy of the catalysts by using computational methods.

1.2.3 Descriptors in computational catalysis

Nowadays, the appearance of the descriptors dramatically increases the efficiency of the catalysts screenings in that computational scientists depend on the descriptors to make predictions for the performance of catalysts. Generally, an outstanding descriptor should possess two characteristics: (1) the format of the descriptor is supposed to be as simple as possible; (2) the descriptor should have physical foundations behind it. In this section, we divided the current prevalent descriptors into energy descriptors, electronic descriptors, and geometric descriptors.

The energy descriptors aim at utilizing computationally inexpensive energy variables to predict those that are computationally expensive. The Brønsted–Evans–Polanyi Relationship (BEP)[106, 107] is an exemplary model among these descriptors, which illustrates a linear relationship between the reaction activation energy and the reaction energy. At present, researchers still are utilizing the BEP relationships for metals[108], metal oxides and metal carbides[109]. In 2016, Dr. Jens K. Nørskov's group developed a similar descriptor for predicting the C-H bond activation energy by the hydrogen affinities and C-H bond strength, and they test their predictions among various catalysts system (e.g., metals, metal oxides, MOFs, and Graphene) and found their fitting relationships will always stand[110].

The electronic descriptors mainly focus on the electronic structures of the materials. Most important descriptor among these is the d-band theory developed by Dr. B. Hammer and Dr. Jens K. Nørskov, which describing the adsorption strength of metals[111]. In their work, they found that when the adsorbates attach on the metal surfaces, the orbitals of adsorbates will interact with the s and d orbitals of the metal surfaces, which lead to the formation of the anti-bonding states and bonding states. Apart from the d-band theory, Dr. Jinlong Gong's group recently developed the ionization energies as the descriptor, to predict the adsorption of oxygen (*O) and hydroxyl (OH*) groups over a variety of materials (i.e., metal oxides, graphene, metal alloys, and zeolites)[112].

The geometric descriptors are generally focused on the spatial structure of the catalyst models. The Generalize Coordination Numbers (GCN) are the most prevalent geometric descriptor. The GCN is defined as the following equation:

$$\overline{CN}(i) = \sum_{j=1}^{n_i} \frac{cn(j)}{cn_{max}} \tag{1.1}$$

Where $\overline{CN}(i)$ is the GCN of atom i, the $cn(j)$ refers to the coordination numbers of the neighboring atoms of i, cn_{max} refers to the previous work[113]. As we can see from the equation (1.1), the GCN not only considers the coordination number of the centering atom but also considers the coordination of surrounding atoms. The GCN could be utilized to predict the adsorption energies of various adsorbates (e.g., OH*, OOH*)[113], and this relationship could be applied to not only the metal cluster models with different sizes but also the surface slab models.

Apart from the following descriptors, with the development of the computer hardware and machine learning methods, the machine learnings techniques have been widely used to predict the performance of the materials[114]. Some researchers leveraged the Convolutional network to learn the molecular fingerprint[115]. Also, Dr. Fung collaborated with Dr. Jiang utilized several machine learning methods (e.g., kernel-ridge regression, neural network) to predict the H adsorption energies of 2D materials[116]. However, it’s still hard to unveil the black-box effects when applying the machine learning models to predict the behaviors chemical reactions without the physical chemistry foundation for the materials.

1.3 References

(1) Qiao, B.; Wang, A.; Yang, X.; Allard, L. F.; Jiang, Z.; Cui, Y.; Liu, J.; Li, J.; Zhang, T. Single-atom catalysis of CO oxidation using Pt_1/FeO_x. *Nature Chemistry* **2011**, *3* (8), 634-641. DOI: 10.1038/nchem.1095.

(2) Xiao, M.; Zhu, J.; Li, G.; Li, N.; Li, S.; Cano, Z. P.; Ma, L.; Cui, P.; Xu, P.; Jiang, G.; et al. A Single-Atom Iridium Heterogeneous Catalyst in Oxygen Reduction Reaction. *Angewandte Chemie International Edition* **2019**, *58* (28), 9640-9645. DOI: 10.1002/anie.201905241.

(3) Zhou, H.; Hong, S.; Zhang, H.; Chen, Y.; Xu, H.; Wang, X.; Jiang, Z.; Chen, S.; Liu, Y. Toward biomass-based single-atom catalysts and plastics: Highly active single-atom Co on N-doped carbon for oxidative esterification of primary alcohols. *Applied Catalysis B: Environmental* **2019**, *256*, 117767. DOI: 10.1016/j.apcatb.2019.117767.

(4) Han, B.; Guo, Y.; Huang, Y.; Xi, W.; Xu, J.; Luo, J.; Qi, H.; Ren, Y.; Liu, X.; Qiao, B.; et al. Strong Metal–Support Interactions between Pt Single-Atoms and TiO_2. *Angewandte Chemie International Edition* **2020**, *59* (29), 11824-11829. DOI: 10.1002/anie.202003208.

(5) Zhou, X.; Shen, Q.; Yuan, K.; Yang, W.; Chen, Q.; Geng, Z.; Zhang, J.; Shao, X.; Chen, W.; Xu, G.; et al. Unraveling Charge State of Supported Au Single-Atoms during CO Oxidation. *Journal of the American Chemical Society* **2018**, *140* (2), 554-557. DOI: 10.1021/jacs.7b10394.

(6) Tiwari, J. N.; Harzandi, A. M.; Ha, M.; Sultan, S.; Myung, C. W.; Park, H. J.; Kim, D. Y.; Thangavel, P.; Singh, A. N.; Sharma, P.; et al. High-Performance Hydrogen Evolution by Ru Single-Atoms and Nitrided-Ru Nanoparticles Implanted on N-Doped Graphitic Sheet. *Advanced Energy Materials* **2019**, *9* (26), 1900931. DOI: 10.1002/aenm.201900931.

(7) Liu, J. Catalysis by Supported Single Metal Atoms. *ACS Catalysis* **2017**, *7* (1), 34-59. DOI: 10.1021/acscatal.6b01534.

(8) Lai, W.-H.; Miao, Z.; Wang, Y.-X.; Wang, J.-Z.; Chou, S.-L. Atomic-Local Environments of Single-Atom Catalysts: Synthesis, Electronic Structure, and Activity. *Advanced Energy Materials* **2019**, *9* (43), 1900722. DOI: aenm.201900722.

(9) Song, X.; Shao, F.; Zhao, Z.; Li, X.; Wei, Z.; Wang, J. Single-Atom Ni-Modified Al_2O_3-Supported Pd for Mild-Temperature Semi-hydrogenation of Alkynes. *ACS Catalysis* **2022**, *12* (24), 14846-14855. DOI: 10.1021/acscatal.2c04883.

(10) Nakaya, Y.; Hirayama, J.; Yamazoe, S.; Shimizu, K.-i.; Furukawa, S. Single-atom Pt in intermetallics as an ultrastable and selective catalyst for propane dehydrogenation. *Nature Communications* **2020**, *11* (1), 2838. DOI: 10.1038/s41467-020-16693-9.

(11) Li, X.; Surkus, A.-E.; Rabeah, J.; Anwar, M.; Dastigir, S.; Junge, H.; Brückner, A.; Beller, M. Cobalt Single-Atom Catalysts with High Stability for Selective Dehydrogenation of Formic Acid. *Angewandte Chemie International Edition* **2020**, *59* (37), 15849-15854. DOI: 10.1002/anie.202004125.

(12) Zhu, C.; Shi, Q.; Feng, S.; Du, D.; Lin, Y. Single-Atom Catalysts for Electrochemical Water Splitting. *ACS Energy Letters* **2018**, *3* (7), 1713-1721. DOI: 10.1021/acsenergylett.8b00640.

(13) Wang, Y.; Huang, X.; Wei, Z. Recent developments in the use of single-atom catalysts for water splitting. *Chin. J. Catal.* **2021**, *42* (8), 1269-1286. DOI: 10.1016/S1872-2067(20)63619-1.

(14) Yang, H.; Li, G.; Jiang, G.; Zhang, Z.; Hao, Z. Heterogeneous selective oxidation over supported metal catalysts: From nanoparticles to Single-Atoms. *Applied Catalysis B: Environmental* **2023**, *325*, 122384. DOI: 10.1016/j.apcatb.2023.122384.

(15) Li, M.; Wu, S.; Yang, X.; Hu, J.; Peng, L.; Bai, L.; Huo, Q.; Guan, J. Highly efficient Single-Atom cobalt catalyst for selective oxidation of alcohols. *Applied Catalysis A: General* **2017**, *543*, 61-66. DOI: 10.1016/j.apcata.2017.06.018.

(16) Zhang, H.; Liu, G.; Shi, L.; Ye, J. Single-Atom Catalysts: Emerging Multifunctional Materials in Heterogeneous Catalysis. *Advanced Energy Materials* **2018**, *8* (1), 1701343. DOI: 10.1002/aenm.201701343.

(17) Zhou, J.; Zhao, J.; Zhang, J.; Zhang, T.; Ye, M.; Liu, Z. Regeneration of catalysts deactivated by coke deposition: A review. *Chin. J. Catal.* **2020**, *41* (7), 1048-1061. DOI: 10.1016/S1872-2067(20)63552-5.

(18) Zhang, Y.; Guo, L.; Tao, L.; Lu, Y.; Wang, S. Defect-Based Single-Atom Electrocatalysts. *Small Methods* **2019**, *3* (9), 1800406. DOI: 10.1002/smtd.201800406.

(19) Zhang, L.; Zhao, X.; Yuan, Z.; Wu, M.; Zhou, H. Oxygen defect-stabilized heterogeneous Single-Atom catalysts: preparation, properties and catalytic application. *Journal of Materials Chemistry A* **2021**, *9* (7), 3855-3879. DOI: 10.1039/D0TA10541D.

(20) He, J.; Li, N.; Li, Z.-G.; Zhong, M.; Fu, Z.-X.; Liu, M.; Yin, J.-C.; Shen, Z.; Li, W.; Zhang, J.; et al. Strategic Defect Engineering of Metal–Organic Frameworks for Optimizing the Fabrication of Single-Atom Catalysts. *Advanced Functional Materials* **2021**, *31* (41), 2103597. DOI: 10.1002/adfm.202103597.

(21) Lang, R.; Xi, W.; Liu, J.-C.; Cui, Y.-T.; Li, T.; Lee, A. F.; Chen, F.; Chen, Y.; Li, L.; Li, L.; et al. Non defect-stabilized thermally stable single-atom catalyst. *Nature Communications* **2019**, *10* (1), 234. DOI: 10.1038/s41467-018-08136-3.

(22) Qi, K.; Chhowalla, M.; Voiry, D. Single-Atom is not alone: Metal–support interactions in single-atom catalysis. *Materials Today* **2020**, *40*, 173-192. DOI: 10.1016/j.mattod.2020.07.002.

(23) Marcinkowski, M. D.; Darby, M. T.; Liu, J.; Wimble, J. M.; Lucci, F. R.; Lee, S.; Michaelides, A.; Flytzani-Stephanopoulos, M.; Stamatakis, M.; Sykes, E. C. H. Pt/Cu single-atom alloys as coke-resistant catalysts for efficient C–H activation. *Nature Chemistry* **2018**, *10* (3), 325-332. DOI: 10.1038/nchem.2915.

(24) Boucher, M. B.; Zugic, B.; Cladaras, G.; Kammert, J.; Marcinkowski, M. D.; Lawton, T. J.; Sykes, E. C. H.; Flytzani-Stephanopoulos, M. Single-Atom alloy surface analogs in $Pd_{0.18}Cu_{15}$ nanoparticles for selective hydrogenation reactions. *Physical Chemistry Chemical Physics* **2013**, *15* (29), 12187-12196. DOI: 10.1039/C3CP51538A.

(25) Patel, D. A.; Kress, P. L.; Cramer, L. A.; Larson, A. M.; Sykes, E. C. H. Elucidating the composition of PtAg surface alloys with atomic-scale imaging and spectroscopy. *The Journal of Chemical Physics* **2019**, *151* (16). DOI: 10.1063/1.5124687.

(26) Patel, D. A.; Hannagan, R. T.; Kress, P. L.; Schilling, A. C.; Çınar, V.; Sykes, E. C. H. Atomic-Scale Surface Structure and CO Tolerance of NiCu Single-Atom Alloys. *The Journal of Physical Chemistry C* **2019**, *123* (46), 28142-28147. DOI: 10.1021/acs.jpcc.9b07513.

(27) Sun, G.; Zhao, Z.-J.; Mu, R.; Zha, S.; Li, L.; Chen, S.; Zang, K.; Luo, J.; Li, Z.; Purdy, S. C.; et al. Breaking the scaling relationship via thermally stable Pt/Cu Single-Atom alloys for catalytic dehydrogenation. *Nature Communications* **2018**, *9* (1), 4454. DOI: 10.1038/s41467-018-06967-8.

(28) Lang, R.; Du, X.; Huang, Y.; Jiang, X.; Zhang, Q.; Guo, Y.; Liu, K.; Qiao, B.; Wang, A.; Zhang, T. Single-Atom Catalysts Based on the Metal–Oxide Interaction. *Chemical Reviews* **2020**, *120* (21), 11986-12043. DOI: 10.1021/acs.chemrev.0c00797.

(29) Marcinkowski, M. D.; Yuk, S. F.; Doudin, N.; Smith, R. S.; Nguyen, M.-T.; Kay, B. D.; Glezakou, V.-A.; Rousseau, R.; Dohnálek, Z. Low-Temperature Oxidation of Methanol to Formaldehyde on a Model Single-Atom Catalyst: Pd Atoms on Fe_3O_4(001). *ACS Catalysis* **2019**, *9* (12), 10977-10982. DOI: 10.1021/acscatal.9b03891.

(30) Lin, J.; Qiao, B.; Li, N.; Li, L.; Sun, X.; Liu, J.; Wang, X.; Zhang, T. Little do more: a highly effective Pt_1/FeO_x single-atom catalyst for the reduction of NO by H_2. *Chemical Communications* **2015**, *51* (37), 7911-7914. DOI: 10.1039/C5CC00714C.

(31) Spezzati, G.; Su, Y.; Hofmann, J. P.; Benavidez, A. D.; DeLaRiva, A. T.; McCabe, J.; Datye, A. K.; Hensen, E. J. M. Atomically Dispersed Pd–O Species on CeO_2(111) as Highly Active Sites for Low-Temperature CO Oxidation. *ACS Catalysis* **2017**, *7* (10), 6887-6891. DOI: 10.1021/acscatal.7b02001.

(32) Zhao, Y.; Cui, C.; Han, J.; Wang, H.; Zhu, X.; Ge, Q. Direct C-C Coupling of CO_2 and the Methyl Group from CH_4 Activation through Facile Insertion of CO_2 into Zn-CH_3 sigma-Bond. *Journal of American Chemical Society* **2016**, *138* (32), 10191-10198. DOI: 10.1021/jacs.6b04446.

(33) Daelman, N.; Capdevila-Cortada, M.; López, N. Dynamic charge and oxidation state of Pt/CeO2 single-atom catalysts. *Nature Materials* **2019**, *18* (11), 1215-1221. DOI: 10.1038/s41563-019-0444-y.

(34) Guo, Y.; Mei, S.; Yuan, K.; Wang, D.-J.; Liu, H.-C.; Yan, C.-H.; Zhang, Y.-W. Low-Temperature CO_2 Methanation over CeO_2-Supported Ru Single-Atoms, Nanoclusters, and Nanoparticles Competitively Tuned by Strong Metal–Support Interactions and H-Spillover Effect. *ACS Catalysis* **2018**, *8* (7), 6203-6215. DOI: 10.1021/acscatal.7b04469.

(35) Wu, D.; Liu, S.; Zhong, M.; Zhao, J.; Du, C.; Yang, Y.; Sun, Y.; Lin, J.; Wan, S.; Wang, S.; et al. Nature and Dynamic Evolution of Rh Single-Atoms Trapped by CeO_2 in CO Hydrogenation. *ACS Catalysis* **2022**, *12* (19), 12253-12267. DOI: 10.1021/acscatal.2c02103.

(36) Wang, Y.; Chen, Z.; Han, P.; Du, Y.; Gu, Z.; Xu, X.; Zheng, G. Single-Atomic Cu with Multiple Oxygen Vacancies on Ceria for Electrocatalytic CO_2 Reduction to CH_4. *ACS Catalysis* **2018**, *8* (8), 7113-7119. DOI: 10.1021/acscatal.8b01014.

(37) Thang, H. V.; Pacchioni, G.; DeRita, L.; Christopher, P. Nature of stable Single-Atom Pt catalysts dispersed on anatase TiO_2. *Journal of Catalysis* **2018**, *367*, 104-114. DOI: 10.1016/j.jcat.2018.08.025.

(38) Shen, G.; Zhang, R.; Pan, L.; Hou, F.; Zhao, Y.; Shen, Z.; Mi, W.; Shi, C.; Wang, Q.; Zhang, X.; et al. Regulating the Spin State of Fe^{III} by Atomically Anchoring on Ultrathin Titanium Dioxide for Efficient Oxygen Evolution Electrocatalysis. *Angewandte Chemie International Edition* **2020**, *59* (6), 2313-2317. DOI: 10.1002/anie.201913080.

(39) Koust, S.; Arnarson, L.; Moses, P. G.; Li, Z.; Beinik, I.; Lauritsen, J. V.; Wendt, S. Facile embedding of single vanadium atoms at the anatase TiO_2(101) surface. *Physical Chemistry Chemical Physics* **2017**, *19* (14), 9424-9431. DOI: 10.1039/C6CP06965G.

(40) Wang, Y.; Mao, J.; Meng, X.; Yu, L.; Deng, D.; Bao, X. Catalysis with Two-Dimensional Materials Confining Single-Atoms: Concept, Design, and Applications. *Chemical Reviews* **2019**, *119* (3), 1806-1854. DOI: 10.1021/acs.chemrev.8b00501.

(41) Sun, B.; Pang, J.; Cheng, Q.; Zhang, S.; Li, Y.; Zhang, C.; Sun, D.; Ibarlucea, B.; Li, Y.; Chen, D.; et al. Synthesis of Wafer-Scale Graphene with Chemical Vapor Deposition for Electronic Device Applications. *Advanced Materials Technologies* **2021**, *6* (7), 2000744. DOI: 10.1002/admt.202000744.

(42) Raccichini, R.; Varzi, A.; Passerini, S.; Scrosati, B. The role of graphene for electrochemical energy storage. *Nature Materials* **2015**, *14* (3), 271-279. DOI: 10.1038/nmat4170.

(43) Huang, C.; Li, C.; Shi, G. Graphene based catalysts. *Energy & Environmental Science* **2012**, *5* (10), 8848-8868. DOI: 10.1039/C2EE22238H.

(44) Yan, H.; Cheng, H.; Yi, H.; Lin, Y.; Yao, T.; Wang, C.; Li, J.; Wei, S.; Lu, J. Single-Atom Pd1/Graphene Catalyst Achieved by Atomic Layer Deposition: Remarkable Performance in Selective Hydrogenation of 1,3-Butadiene. *Journal of the American Chemical Society* **2015**, *137* (33), 10484-10487. DOI: 10.1021/jacs.5b06485.

(45) Xuan, N.; Chen, J.; Shi, J.; Yue, Y.; Zhuang, P.; Ba, K.; Sun, Y.; Shen, J.; Liu, Y.; Ge, B.; et al. Single-Atom Electroplating on Two Dimensional Materials. *Chemistry of Materials* **2019**, *31* (2), 429-435. DOI: 10.1021/acs.chemmater.8b03796.

(46) Sun, Z.; Yang, Y.; Fang, C.; Yao, Y.; Qin, F.; Gu, H.; Liu, Q.; Xu, W.; Tang, H.; Jiang, Z.; et al. Atomic-Level Pt Electrocatalyst Synthesized via Iced Photochemical Method for Hydrogen Evolution Reaction with High Efficiency. *Small* **2022**, *18* (33), 2203422. DOI: 10.1002/smll.202203422.

(47) Fei, H.; Dong, J.; Chen, D.; Hu, T.; Duan, X.; Shakir, I.; Huang, Y.; Duan, X. Single-Atom electrocatalysts supported on graphene or graphene-like carbons. *Chemical Society Reviews* **2019**, *48* (20), 5207-5241. DOI: 10.1039/C9CS00422J.

(48) Nakada, K.; Ishii, A. DFT Calculation for Adatom Adsorption on Graphene. *Graphene Simulation*, **2011**, 1-19. DOI: 10.5772/20477

(49) Mao, Y.; Yuan, J.; Zhong, J. Density functional calculation of transition metal adatom adsorption on graphene. *Journal of Physics: Condensed Matter* **2008**, *20* (11), 115209. DOI: 10.1088/0953-8984/20/11/115209.

(50) Ni, J.; Quintana, M.; Song, S. Adsorption of small gas molecules on transition metal (Fe, Ni and Co, Cu) doped graphene: A systematic DFT study. *Physica E: Low-dimensional Systems and Nanostructures* **2020**, *116*, 113768. DOI: 10.1016/j.physe.2019.113768.

(51) Liu, Z.; Zhang, D.; Wei, T.; Wang, L.; Li, X.; Liu, B. Adsorption characteristics of formaldehyde on nitrogen doped graphene-based Single-Atom adsorbents: A DFT study. *Applied Surface Science* **2019**, *493*, 1260-1267. DOI: 10.1016/j.apsusc.2019.07.114.

(52) Zhuo, H.-Y.; Zhang, X.; Liang, J.-X.; Yu, Q.; Xiao, H.; Li, J. Theoretical Understandings of Graphene-based Metal Single-Atom Catalysts: Stability and Catalytic Performance. *Chemical Reviews* **2020**, *120* (21), 12315-12341. DOI: 10.1021/acs.chemrev.0c00818.

(53) Du, Z.; Chen, X.; Hu, W.; Chuang, C.; Xie, S.; Hu, A.; Yan, W.; Kong, X.; Wu, X.; Ji, H.; et al. Cobalt in Nitrogen-Doped Graphene as Single-Atom Catalyst for High-Sulfur Content Lithium–Sulfur Batteries. *Journal of the American Chemical Society* **2019**, *141* (9), 3977-3985. DOI: 10.1021/jacs.8b12973.

(54) Lou, Y.; Zheng, Y.; Li, X.; Ta, N.; Xu, J.; Nie, Y.; Cho, K.; Liu, J. Pocketlike Active Site of Rh_1/MoS_2 Single-Atom Catalyst for Selective Crotonaldehyde Hydrogenation. *Journal of the American Chemical Society* **2019**, *141* (49), 19289-19295. DOI: 10.1021/jacs.9b06628.

(55) Qiao, B.; Liu, J.; Wang, Y.-G.; Lin, Q.; Liu, X.; Wang, A.; Li, J.; Zhang, T.; Liu, J. Highly Efficient Catalysis of Preferential Oxidation of CO in H_2-Rich Stream by Gold Single-Atom Catalysts. *ACS Catalysis* **2015**, *5* (11), 6249-6254. DOI: 10.1021/acscatal.5b01114.

(56) Zhao, J.; Chen, Z. Single Mo Atom Supported on Defective Boron Nitride Monolayer as an Efficient Electrocatalyst for Nitrogen Fixation: A Computational Study. *Journal of the American Chemical Society* **2017**, *139* (36), 12480-12487. DOI: 10.1021/jacs.7b05213.

(57) Esrafili, M. D.; Rad, F. A. A DFT Study of Single-Atom Catalysis of CO Oxidation Using Carbon-Embedded Hexagonal Boron Nitride Monolayer. *ChemistrySelect* **2018**, *3* (25), 7402-7409. DOI: 10.1002/slct.201801317.

(58) Leybo, D. V.; Ryzhova, A. A.; Matveev, A. T.; Firestein, K. L.; Tarakanov, P. A.; Konopatsky, A. S.; Trigub, A. L.; Sukhanova, E. V.; Popov, Z. I.; Golberg, D. V.; et al. Iron phthalocyanine derived Fe_1/h-BN Single-Atom catalysts for CO_2 hydrogenation. *Journal of Materials Chemistry A* **2023**, *11* (22), 11874-11888. DOI: 10.1039/D3TA00356F.

(59) Zhu, L.; Liu, X.-Q.; Jiang, H.-L.; Sun, L.-B. Metal–Organic Frameworks for Heterogeneous Basic Catalysis. *Chemical Reviews* **2017**, *117* (12), 8129-8176. DOI: 10.1021/acs.chemrev.7b00091.

(60) Xu, Z.; Zhao, G.; Ullah, L.; Wang, M.; Wang, A.; Zhang, Y.; Zhang, S. Acidic ionic liquid based UiO-67 type MOFs: a stable and efficient heterogeneous catalyst for esterification. *RSC Advances* **2018**, *8* (18), 10009-10016. DOI: 10.1039/C8RA01119B.

(61) Ahmed, I.; Hasan, Z.; Khan, N. A.; Jhung, S. H. Adsorptive denitrogenation of model fuels with porous metal-organic frameworks (MOFs): Effect of acidity and basicity of MOFs. *Applied Catalysis B: Environmental* **2013**, *129*, 123-129. DOI: 10.1016/j.apcatb.2012.09.020.

(62) Chen, J.; Liu, R.; Gao, H.; Chen, L.; Ye, D. Amine-functionalized metal-organic frameworks for the transesterification of triglycerides. *Journal of Materials Chemistry A* **2014**, *2* (20), 7205-7213. DOI: 10.1039/C4TA00253A.

(63) Bernt, S.; Guillerm, V.; Serre, C.; Stock, N. Direct covalent post-synthetic chemical modification of Cr-MIL-101 using nitrating acid. *Chemical Communications* **2011**, *47* (10), 2838-2840. DOI: 10.1039/C0CC04526H.

(64) Burrows, A. D.; Frost, C. G.; Mahon, M. F.; Richardson, C. Sulfur-tagged metal–organic frameworks and their post-synthetic oxidation. *Chemical Communications* **2009**, (28), 4218-4220. DOI: 10.1039/B906170C.

(65) Yin, P.; Yao, T.; Wu, Y.; Zheng, L.; Lin, Y.; Liu, W.; Ju, H.; Zhu, J.; Hong, X.; Deng, Z.; et al. Single Cobalt Atoms with Precise N-Coordination as Superior Oxygen Reduction Reaction Catalysts. *Angewandte Chemie International Edition* **2016**, *55* (36), 10800-10805. DOI: 10.1002/anie.201604802.

(66) Fang, X.; Shang, Q.; Wang, Y.; Jiao, L.; Yao, T.; Li, Y.; Zhang, Q.; Luo, Y.; Jiang, H.-L. Single Pt Atoms Confined into a Metal–Organic Framework for Efficient Photocatalysis. *Advanced Materials* **2018**, *30* (7), 1705112. DOI: 10.1002/adma.201705112.

(67) Li, Z.; Schweitzer, N. M.; League, A. B.; Bernales, V.; Peters, A. W.; Getsoian, A. B.; Wang, T. C.; Miller, J. T.; Vjunov, A.; Fulton, J. L.; et al. Sintering-Resistant Single-Site Nickel Catalyst Supported by Metal–Organic Framework. *Journal of the American Chemical Society* **2016**, *138* (6), 1977-1982. DOI: 10.1021/jacs.5b12515.

(68) Otake, K.; Cui, Y.; Buru, C. T.; Li, Z.; Hupp, J. T.; Farha, O. K. Single-Atom-Based Vanadium Oxide Catalysts Supported on Metal-Organic Frameworks: Selective Alcohol Oxidation and Structure-Activity Relationship. *Journal of the American Chemical Society* **2018**, *140* (28), 8652-8656. DOI: 10.1021/jacs.8b05107.

(69) Sperger, T.; Sanhueza, I. A.; Kalvet, I.; Schoenebeck, F. Computational Studies of Synthetically Relevant Homogeneous Organometallic Catalysis Involving Ni, Pd, Ir, and Rh: An Overview of Commonly Employed DFT Methods and Mechanistic Insights. *Chemical Reviews* **2015**, *115* (17), 9532-9586. DOI: 10.1021/acs.chemrev.5b00163.

(70) Liu, X.; Wen, X.; Hoffmann, R. Surface Activation of Transition Metal Nanoparticles for Heterogeneous Catalysis: What We Can Learn from Molecular Dynamics. *ACS Catalysis* **2018**, *8* (4), 3365-3375. DOI: 10.1021/acscatal.7b04468.

(71) Tvaroška, I. Atomistic insight into the catalytic mechanism of glycosyltransferases by combined quantum mechanics/molecular mechanics (QM/MM) methods. *Carbohydrate Research* **2015**, *403*, 38-47. DOI: 10.1016/j.carres.2014.06.017.

(72) Piskunov, S.; Heifets, E.; Eglitis, R. I.; Borstel, G. Bulk properties and electronic structure of $SrTiO_3$, $BaTiO_3$, $PbTiO_3$ perovskites: an ab initio HF/DFT study. *Computational Materials Science* **2004**, *29* (2), 165-178. DOI: 10.1016/j.commatsci.2003.08.036.

(73) Zhu, W.; Wu, P. Surface energetics of hydroxyapatite: a DFT study. *Chemical Physics Letters* **2004**, *396* (1), 38-42. DOI: 10.1016/j.cplett.2004.08.006.

(74) Fernández-Pello, D.; Fernández-Díaz, J. M.; Cerdeira, M. A.; González, C.; Iglesias, R. Energetic, electronic and structural DFT analysis of point defects in refractory BCC metals. *Materials Today Communications* **2020**, *24*, 101323. DOI: 10.1016/j.mtcomm.2020.101323.

(75) Park, J.; Yu, B. D.; Hong, S. Van der Waals density functional theory study for bulk solids with BCC, FCC, and diamond structures. *Current Applied Physics* **2015**, *15* (8), 885-891. DOI: 10.1016/j.cap.2015.03.028.

(76) Wu, X.; Wang, R.; Wang, S. Generalized-stacking-fault energy and surface properties for HCP metals: A first-principles study. *Applied Surface Science* **2010**, *256* (11), 3409-3412. DOI: 10.1016/j.apsusc.2009.12.042.

(77) Masayoshi Mikami, M. M.; Shinichiro Nakamura, S. N.; Osamu Kitao, O. K.; Hironori Arakawa, H. A.; Xavier Gonze, X. G. First-Principles Study of Titanium Dioxide: Rutile and Anatase. *Japanese Journal of Applied Physics* **2000**, *39* (8B), L847. DOI: 10.1143/JJAP.39.L847.

(78) Li, H.; Zha, S.; Zhao, Z.-J.; Tian, H.; Chen, S.; Gong, Z.; Cai, W.; Wang, Y.; Cui, Y.; Zeng, L.; et al. The Nature of Loading-Dependent Reaction Barriers over Mixed RuO_2/TiO_2 Catalysts. *ACS Catalysis* **2018**, *8* (6), 5526-5532. DOI: 10.1021/acscatal.8b00797.

(79) Tripkovic, V.; Hansen, H. A.; Garcia-Lastra, J. M.; Vegge, T. Comparative DFT+U and HSE Study of the Oxygen Evolution Electrocatalysis on Perovskite Oxides. *The Journal of Physical Chemistry C* **2018**, *122* (2), 1135-1147. DOI: 10.1021/acs.jpcc.7b07660.

(80) Ezbiri, M.; Takacs, M.; Stolz, B.; Lungthok, J.; Steinfeld, A.; Michalsky, R. Design principles of perovskites for solar-driven thermochemical splitting of CO_2. *Journal of Materials Chemistry A* **2017**, *5* (29), 15105-15115. DOI: 10.1039/c7ta02081c.

(81) Wang, S.; Zhao, Z.-J.; Chang, X.; Zhao, J.; Tian, H.; Yang, C.; Li, M.; Fu, Q.; Mu, R.; Gong, J. Activation and Spillover of Hydrogen on Sub-1 nm Palladium Nanoclusters Confined within Sodalite Zeolite for the Semi-Hydrogenation of Alkynes. *Angewandte Chemie International Edition* **2019**, *58* (23), 7668-7672. DOI: 10.1002/anie.201903827.

(82) Digne, M.; Sautet, P.; Raybaud, P.; Euzen, P.; Toulhoat, H. Hydroxyl Groups on γ-Alumina Surfaces: A DFT Study. *Journal of Catalysis* **2002**, *211* (1), 1-5. DOI: 10.1006/jcat.2002.3741.

(83) Saerens, S.; Sabbe, M. K.; Galvita, V. V.; Redekop, E. A.; Reyniers, M.-F.; Marin, G. B. The Positive Role of Hydrogen on the Dehydrogenation of Propane on Pt(111). *ACS Catalysis* **2017**, *7* (11), 7495-7508. DOI: 10.1021/acscatal.7b01584.

(84) Zhao, Z.-J.; Zhao, J.; Chang, X.; Zha, S.; Zeng, L.; Gong, J. Competition of C-C bond formation and C-H bond formation For acetylene hydrogenation on transition metals: A density functional theory study. *AIChE Journal* **2019**, *65* (3), 1059-1066. DOI: 10.1002/aic.16492.

(85) Jiao, Y.; Ma, H.; Ren, P.; Li, T.; Li, Y.-W.; Wen, X.-D.; Jiao, H. Exploring coverage-dependent chain-growth mechanisms on Ru(111) for Fischer–Tropsch synthesis. *Catalysis Science & Technology* **2023**, *13* (2), 437-456. DOI: 10.1039/D2CY01279K.

(86) Orita, H.; Inada, Y. DFT Investigation of CO Adsorption on Pt(211) and Pt(311) Surfaces from Low to High Coverage. *The Journal of Physical Chemistry B* **2005**, *109* (47), 22469-22475. DOI: 10.1021/jp052583a.

(87) Chizallet, C.; Costentin, G.; Che, M.; Delbecq, F.; Sautet, P. Infrared Characterization of Hydroxyl Groups on MgO: A Periodic and Cluster Density Functional Theory Study. *Journal of the American Chemical Society* **2007**, *129* (20), 6442-6452. DOI: 10.1021/ja068720e.

(88) Cheng, Z.; Qin, L.; Guo, M.; Xu, M.; Fan, J. A.; Fan, L.-S. Oxygen vacancy promoted methane partial oxidation over iron oxide oxygen carriers in the chemical looping process. *Physical Chemistry Chemical Physics* **2016**, *18* (47), 32418-32428. DOI: 10.1039/C6CP06264D.

(89) Cheng, Z.; Baser, D. S.; Nadgouda, S. G.; Qin, L.; Fan, J. A.; Fan, L.-S. C_2 Selectivity Enhancement in Chemical Looping Oxidative Coupling of Methane over a Mg–Mn Composite Oxygen Carrier by Li-Doping-Induced Oxygen Vacancies. *ACS Energy Letters* **2018**, *3* (7), 1730-1736. DOI: 10.1021/acsenergylett.8b00851.

(90) Hyde, E.; Beck, M. Comprehensive DFT study of hydroxyl coverage on titania surfaces. *Applied Surface Science* **2019**, *498*, 143893. DOI: 10.1016/j.apsusc.2019.143893.

(91) Hinuma, Y.; Toyao, T.; Kamachi, T.; Maeno, Z.; Takakusagi, S.; Furukawa, S.; Takigawa, I.; Shimizu, K.-i. Density Functional Theory Calculations of Oxygen Vacancy Formation and Subsequent Molecular Adsorption on Oxide Surfaces. *The Journal of Physical Chemistry C* **2018**, *122* (51), 29435-29444. DOI: 10.1021/acs.jpcc.8b11279.

(92) Li, L.; Larsen, A. H.; Romero, N. A.; Morozov, V. A.; Glinsvad, C.; Abild-Pedersen, F.; Greeley, J.; Jacobsen, K. W.; Nørskov, J. K. Investigation of Catalytic Finite-Size-Effects of Platinum Metal Clusters. *The Journal of Physical Chemistry Letters* **2013**, *4* (1), 222-226. DOI: 10.1021/jz3018286.

(93) Kleis, J.; Greeley, J.; Romero, N. A.; Morozov, V. A.; Falsig, H.; Larsen, A. H.; Lu, J.; Mortensen, J. J.; Dułak, M.; Thygesen, K. S.; et al. Finite Size Effects in Chemical Bonding: From Small Clusters to Solids. *Catalysis Letters* **2011**, *141* (8), 1067-1071. DOI: 10.1007/s10562-011-0632-0.

(94) Jakubikova, E.; Rappé, A. K.; Bernstein, E. R. Density Functional Theory Study of Small Vanadium Oxide Clusters. *The Journal of Physical Chemistry A* **2007**, *111* (50), 12938-12943. DOI: 10.1021/jp0745844.

(95) Zhang, T.; Solé-Daura, A.; Hostachy, S.; Blanchard, S.; Paris, C.; Li, Y.; Carbó, J. J.; Poblet, J. M.; Proust, A.; Guillemot, G. Modeling the Oxygen Vacancy at a Molecular Vanadium(III) Silica-Supported Catalyst. *Journal of the American Chemical Society* **2018**, *140* (44), 14903-14914. DOI: 10.1021/jacs.8b09048.

(96) Sheng, X.; Himo, F. The Quantum Chemical Cluster Approach in Biocatalysis. *Accounts of Chemical Research* **2023**, *56* (8), 938-947. DOI: 10.1021/acs.accounts.2c00795.

(97) Sun, L. L.; Hermann, K. E.; Noack, J.; Timpe, O.; Teschner, D.; Hävecker, M.; Trunschke, A.; Schlögl, R. DFT Studies and Experiments on Biocatalytic Centers:

Structure, Vibrations, and Core Excitations of the K[VO(O_2)Hheida] Complex. *The Journal of Physical Chemistry C* **2014**, *118* (42), 24611-24622. DOI: 10.1021/jp5081719.

(98) Georgieva, P.; Himo, F. Quantum chemical modeling of enzymatic reactions: The case of histone lysine methyltransferase. *Journal of computational chemistry* **2010**, *31* (8), 1707-1714. DOI: 10.1002/jcc.21458.

(99) Zhao, Z. J.; Chiu, C. C.; Gong, J. Molecular understandings on the activation of light hydrocarbons over heterogeneous catalysts. *Chem Sci* **2015**, *6* (8), 4403-4425. DOI: 10.1039/c5sc01227a.

(100) Tuckerman, M. E.; Ungar, P. J.; von Rosenvinge, T.; Klein, M. L. Ab Initio Molecular Dynamics Simulations. *The Journal of Physical Chemistry* **1996**, *100* (31), 12878-12887. DOI: 10.1021/jp960480+.

(101) Wang, K.; Fung, V.; Wu, Z.; Jiang, D.-e. Stable Surface Terminations of a Perovskite Oxyhydride from First-Principles. *The Journal of Physical Chemistry C* **2020**, *124* (34), 18557-18563. DOI: 10.1021/acs.jpcc.0c03956.

(102) Li, H.; Xiong, C.; Fei, M.; Ma, L.; Zhang, H.; Yan, X.; Tieu, P.; Yuan, Y.; Zhang, Y.; Nyakuchena, J.; et al. Selective Formation of Acetic Acid and Methanol by Direct Methane Oxidation Using Rhodium Single-Atom Catalysts. *Journal of the American Chemical Society* **2023**, *145* (20), 11415-11419. DOI: 10.1021/jacs.3c03113.

(103) Liu, J.; Mohamed, F.; Sauer, J. Selective oxidation of propene by vanadium oxide monomers supported on silica. *Journal of Catalysis* **2014**, *317*, 75-82. DOI: 10.1016/j.jcat.2014.06.003.

(104) Filot, I. A. W.; van Santen, R. A.; Hensen, E. J. M. The Optimally Performing Fischer–Tropsch Catalyst. *Angewandte Chemie International Edition* **2014**, *53* (47), 12746-12750. DOI: 10.1002/anie.201406521.

(105) Filot, I. A. W.; Broos, R. J. P.; van Rijn, J. P. M.; van Heugten, G. J. H. A.; van Santen, R. A.; Hensen, E. J. M. First-Principles-Based Microkinetics Simulations of Synthesis Gas Conversion on a Stepped Rhodium Surface. *ACS Catalysis* **2015**, *5* (9), 5453-5467. DOI: 10.1021/acscatal.5b01391.

(106) Cheng, J.; Hu, P.; Ellis, P.; French, S.; Kelly, G.; Lok, C. M. Brønsted−Evans−Polanyi Relation of Multistep Reactions and Volcano Curve in Heterogeneous Catalysis. *The Journal of Physical Chemistry C* **2008**, *112* (5), 1308-1311. DOI: 10.1021/jp711191j.

(107) Bligaard, T.; Nørskov, J. K.; Dahl, S.; Matthiesen, J.; Christensen, C. H.; Sehested, J. The Brønsted–Evans–Polanyi relation and the volcano curve in heterogeneous catalysis. *Journal of Catalysis* **2004**, *224* (1), 206-217. DOI: 10.1016/j.jcat.2004.02.034.

(108) Munter, T. R.; Bligaard, T.; Christensen, C. H.; Nørskov, J. K. BEP relations for N_2 dissociation over stepped transition metal and alloy surfaces. *Physical Chemistry Chemical Physics* **2008**, *10* (34), 5202-5206. DOI: 10.1039/B720021H.

(109) Viñes, F.; Vojvodic, A.; Abild-Pedersen, F.; Illas, F. Brønsted–Evans–Polanyi Relationship for Transition Metal Carbide and Transition Metal Oxide Surfaces. *The Journal of Physical Chemistry C* **2013**, *117* (8), 4168-4171. DOI: 10.1021/jp312671z.

(110) Latimer, A. A.; Kulkarni, A. R.; Aljama, H.; Montoya, J. H.; Yoo, J. S.; Tsai, C.; Abild-Pedersen, F.; Studt, F.; Nørskov, J. K. Understanding trends in C-H bond activation in heterogeneous catalysis. *Nature Materials* **2017**, *16* (2), 225-229. DOI: 10.1038/nmat4760.

(111) Hammer, B.; Nørskov, J. K. Why gold is the noblest of all the metals. *Nature* **1995**, *376* (6537), 238-240. DOI: 10.1038/376238a0.

(112) Zha, S.; Zhao, Z.-J.; Chen, S.; Liu, S.; Liu, T.; Studt, F.; Gong, J. Predicting the Catalytic Activity of Surface Oxidation Reactions by Ionization Energies. *CCS Chemistry* **2020**, *2* (4), 262-270. DOI: 10.31635/ccschem.020.201900096.

(113) Calle-Vallejo, F.; Tymoczko, J.; Colic, V.; Vu, Q. H.; Pohl, M. D.; Morgenstern, K.; Loffreda, D.; Sautet, P.; Schuhmann, W.; Bandarenka, A. S. Finding optimal surface sites on heterogeneous catalysts by counting nearest neighbors. *Science* **2015**, *350* (6257), 185-189. DOI: 10.1126/science.aab3501.

(114) Singh, S.; Sunoj, R. B. Molecular Machine Learning for Chemical Catalysis: Prospects and Challenges. *Accounts of Chemical Research* **2023**, *56* (3), 402-412. DOI: 10.1021/acs.accounts.2c00801.

(115) Duvenaud, D. K.; Maclaurin, D.; Iparraguirre, J.; Bombarell, R.; Hirzel, T.; Aspuru-Guzik, A.; Adams, R. P. Convolutional networks on graphs for learning molecular fingerprints. *Advances in neural information processing systems* **2015**, *28*. DOI: 10.48550/arXiv.1509.09292

(116) Fung, V.; Hu, G.; Wu, Z.; Jiang, D.-e. Descriptors for Hydrogen Evolution on Single-Atom Catalysts in Nitrogen-Doped Graphene. *The Journal of Physical Chemistry C* **2020**, *124* (36), 19571-19578. DOI: 10.1021/acs.jpcc.0c04432.

Chapter 2. Computational Theories

2.1 The birth of Schrödinger equation

Newton's laws of motion and the law of universal gravitation (Newton's classical mechanics) have had a profound influence on human society since they were first put forward in the 17th century in that Newton's classical mechanics is capable of successfully explaining the celestial bodies motion and dynamic property of everyday object.

However, with the increasing demand for probing the nature of the atom structures by the late 19th century, scientists gradually realized that Newton’s classical mechanics could not well-explain the behavior of microscopic particles. Later, German scientist Werner Heisenberg first put forward the uncertainty principle, which states that for quantum particles, the accuracy of the momentum measurement is inversely correlated to the accuracy of the position measurement. This theory challenges the basics of Newton’s classical mechanics, which assumes that the quantum states (e.g., position, momentum) of particles can be measured concurrently with any accuracy. In the 1920s, Prince Louis de Broglie introduced the concept of matter waves, extending the wave-particle duality from photons to all other quantum particles. Inspired by Louis de Broglie's theory on matter waves, Austrian and naturalized Irish physicist Erwin Schrödinger developed an equation to describe the behavior and property of quantum particles in a wave-like way, this linear partial differential equation is named as Schrödinger equation. The birth of the Schrödinger equation is a milestone in the history of physics, initiating the development of quantum mechanics. The development of Schrödinger equation also opened up a way to better understand the nature and insights of the materials.

2.2 The formula of Schrödinger equation

The Schrödinger equation is a fundamental equation in quantum mechanics, which is a pivot to illuminate the behavior of system at atomic or quantum scales. The foundation of the Schrödinger equation was built on several assumptions: (1) Operator hypothesis, which states that every observable physical quantity in quantum mechanics could be described by the operator. (2) Wave function hypothesis, which claims that the state of the quantum system could be depicted by the wave function, which should be finite and continuous. (3) Identical particles assumption, which refers to the postulation that quantum particles with the same state (wave function) cannot be distinguished from each other. The formula of the Schrödinger equation can be divided into the time-dependent form and time independent form[1]:

2.2.1 Time Dependent Schrödinger equation

The time-dependent form Schrödinger equation depicts the evolution of state of a system with time in the quantum view, which is shown as equation (2.1).

$$\hat{\mathrm{H}}\Psi = \mathrm{i}\hbar\frac{\partial}{\partial \mathrm{t}}\Psi \tag{2.1}$$

This equation is the general form of time-dependent Schrödinger equation for the quantum system. Where the $\hat{\mathrm{H}}$ is Hamiltonian operator, i is the imaginary operator, $\hbar$

refers to reduced Planck constant, t is the time and ψ is the wave function describing the states of the quantum system. ψ is a function of the position of every element in the system and the time.

The expansion of the equation of (2.1) for a single quantum particle can be written as the following equation:

$$i\hbar\frac{\partial}{\partial t}\Psi(x,t) = -\frac{\hbar^2}{2m}\nabla^2\Psi(x,t) + V(x)\Psi(x,t) \qquad (2.2)$$

Where $V(x)$ is the potential energy and it's the time independent function of the particle position x. m refers to the mass of the particle, $\Psi(x,t)$ refers to the wave function and it's the function of the quantum particle position x and the time t.

By conducting the separation of the variables, we can rewrite $\Psi(x,t)$ as $\varphi(x)f(t)$. Where the $\varphi(x)$ is the function of position x only and $f(t)$ is the function of time t only. Thus, the equation (2.2) could be rewritten as the following equation (2.3):

$$-\frac{\hbar^2}{2m}\frac{1}{\varphi(x)}\nabla^2\varphi(x) + V(x) = i\hbar\frac{1}{f(t)}\frac{\partial f(t)}{\partial t} \qquad (2.3)$$

The left side of the equation is solely dependent on the position x while the left side of the equation is solely dependent on the time t. Both sides of the equation would be equal to the energy of the system, which is a constant value.

2.2.2 Time Independent Schrödinger Equation:

To solve the Schrödinger Equation in a simpler way, we would assume that when the wave function at the stationary states. We can derive the time independent version of the Schrödinger Equation by focusing on the left side of (2.3) and multiplying the wave function. Therefore, the (2.3) could be rewritten as time independent form:

$$-\frac{\hbar^2}{2\mathrm{m}}\nabla^2\varphi(\mathrm{x}) + \mathrm{V}(\mathrm{x})\varphi(\mathrm{x}) = \mathrm{E}\varphi(\mathrm{x}) \tag{2.4}$$

Where the E term refers to the total energy of the system and $\varphi(\mathrm{x})$ is the separated wave function and it's only dependent on the position of the particle in the system. Under the situation that the Hamiltonian operator $\widehat{\mathrm{H}}$ is not explicitly dependent on time and the energy of the system is conserved, we would leverage the stationary time independent version. The general form of the Schrödinger Equation was shown as equation (2.5):

$$\widehat{\mathrm{H}}\varphi(\mathrm{x}) = \mathrm{E}\varphi(\mathrm{x}) \tag{2.5}$$

2.3 Solution for the Schrödinger equation

Owing to the complexity of the wave function, it's impossible for the modern computer to solve the exact solution of wave function in that the dimension of the wave function grows exponentially with the number of the particles in the quantum system. Also, for the many-body system, the electrons interact with each other in a complex way and it's hard for scientists to solve for the electron interaction term and the potential energy term. Therefore, researchers are required to make postulations and simplify the Schrödinger Equation to solve it. Aiming at tackling this issue, American physicist Julius Robert Oppenheimer and his Advisor Max Born put forward the Born-Oppenheimer approximation in 1927[2]. Considering that the mass of the nucleus is much larger than electrons, the speed of the electron would be dramatically faster than that of nucleus. Therefore, the nucleus is relatively stationary compared to electrons. Also, the behavior of a single electron won't affect the nucleus. This approximation allows researchers to divide the wave function into electronic wave function and nuclear wave function. Based on the Born-Oppenheimer approximation, Hartree-Fock developed the mean field theory, suggested that the quantum particle in the system experiences the average force field generated by other particles, Hartree-Fork method significantly simplify the complex Schrödinger Equation and utilized the slater determinant to depict the wave function[3]. However, the Hartree-Fork method neglected the interaction between the electrons, and it can lead to the deviation from actual experimental results on the system Energy. To address these deficiencies of the Hartree-Fock method, scientists developed several Post-Hartree-Fock method by adding the electron correction terms between electrons, including the Coupled Cluster (CC) technique[4], Møller–Plesset perturbation theory[5]. Other than post Post-Hartree-Fock method, some methods including N-electron Valence State Perturbation theory[6] and Multireference Configuration Interaction[7] are also prevalent in streamlining the Hartree-Fock method.

2.4 Kohn-Sham equation and Density functional Theory

Owing to the high computing demand of the post Hartree-Fork method and with the increase of the number of electrons and size of the basis set, it's unrealistic to solve the wave function for large systems using expensive basic sets. To tackle this issue, density functional theory transforms the target of solving the wave function into solving the electronic density problem. The concept of the density of electrons can be dated back to the 1920s when Llewellyn Thomas and Enrico Fermi developed the Thomas–Fermi (TF) model[8-10]. However, it was not until Walter Kohn and Pierre Hohenberg put forward the Hohenberg–Kohn theorems, that density functional theory began to have a theoretical foundation[11]. The first Hohenberg–Kohn theorem states that the ground state system energy is a unique function of the electronic density, and the second theorem claims that the energy of a system reaches to the minimum when the electron density is the ground state density. Inspired by the Hohenberg–Kohn theorems, Walter Kohn and Lu Jeu Sham put forward the Kohn–Sham equation[12], developing the exact version of the density function:

$$\left(-\frac{\hbar^2}{2\mathrm{m}}\nabla^2 + \mathrm{v}_{\mathrm{effective}}(\mathrm{x})\right)\psi_{\mathrm{i}}(\mathrm{x}) = \varepsilon_{\mathrm{i}}\psi_{\mathrm{i}}(\mathrm{x}) \tag{2.6}$$

Where $\psi_{\mathrm{i}}(\mathrm{x})$ refers to the Kohn-Sham orbital and ε_{i} refers to the corresponding orbital Energy. $\mathrm{v}_{\mathrm{effective}}(\mathrm{x})$ is named as the Kohn-Sham potential and it could be expanded into three terms as is shown in equation (2.7):

$$v_{eff}(x) = v_{external}(x) + e^2 \int \frac{\rho(r')}{|r-r'|} dr' + \frac{\delta E_{xc}[\rho]}{\delta\rho(r)} \tag{2.7}$$

Where $v_{external}(x)$ is the external potential, $e^2 \int \frac{\rho(r')}{|r-r'|} dr'$ is the term related to Coulomb interaction and $\frac{\delta E_{xc}[\rho]}{\delta\rho(r)}$ refers to the exchange-correlation potential. Once the orbital functions of the system containing N electrons are obtained, the electron density of the system could be calculated using the following equation:

$$n(x) = \sum_{i=1}^{N} |\psi_i(x)|^2 \tag{2.8}$$

Where $n(x)$ is the electron density of the system and it's a function of the coordinates. The procedure to solve for the Kohn-Sham equation is shown as the following steps:(1) Set an initial value for the electron density and utilize it as input for the Kohn-Sham equation to solve for the orbital function $\psi_i(x)$; (2) Leverage the equation (2.8) to obtain the electron density; (3) Compare the electron density obtained by equation (2.8) with previous electron density, if the difference is within the tolerance the process can be terminated; otherwise, we would continue the iteration process for achieving the converged electron density.

2.5 Jacob's Ladder and density functional approximations

The accuracy of the Kohn-Sham equation depends on the specific formula of the exchange-correlation function. If the exchange-correlation term were accurate, researchers would obtain the accurate electron density. However, approximations were made in the real case of solving the exchange-correlation term. The levels of different exchange-correlation functions are shown as the 'Jacob Ladder' classification[13, 14]. The ladder starts from the Hartree World referring to the Hartree Approximation[15] which describing the simple none interacting system where electrons are emerged in the average potential field contributed by other electrons.

With the increasing level of rungs, the method becomes more accurate. The first rung of the ladder refers to the earliest Local Spin-Density Approximation[16] (LSD) that the exchange-correlation function is only related to the spatial distribution of electron density. The LSD is not accurate to account for the bulk and surface properties of metals[16].

To make up the defeats of LSD when solving for the system with inhomogeneous electronic distribution, researcher began to leverage the Generalized Gradient Approximation (GGA)[17] including the gradients of electron density into the exchange-correlation function, which is represented on the second rung of the ladder. GGA dramatically improves the accuracy of predicting the properties of molecules and solids when dealing with the inhomogeneities in electrons distribution, among which the Perdew-Burke-Ernzerhof (PBE)[18] exchange-correlation function is most prevalent. Until now, PBE is still a good option for surface chemistry simulation and this method has been utilized to simulate a variety of materials, like metals[19, 20], metal oxides[21, 22], MOFs[23, 24], etc. PBE offers a good trade-off between calculation efficiency and accuracy of the results. Meta-Generalized Gradient Approximation (Meta-GGA) is a more advanced method than GGA, by incorporating the second order of the derivative and calculating the Laplacian of the electron density[25]. The state-of-art prevalent Meta-GGA methods are TPSS[26], M05-2X/M06-2X[27] and the recent developed SCAN[28] function which has been demonstrated high accuracy in predicting the properties of layered materials.

Although GGA and some advanced Meta-GGA methods dramatically improve the accuracy compared to LSD, it's not accurate enough for simulating the non-covalent interactions[29], which are common in biomolecules when researchers predict the behavior protein-ligand binding. In order to further improve the accuracy especially when dealing with system strong electron correlation effects (i.e., transition metals), scientists began to explore hybrid functions (fourth rung of the ladder in **Figure 2.1**), which mixed a fraction of Hartree-Fock exchange energy terms with LSD or GGA to boost the accuracy of regular DFT. Among these hybrid methods HSE[30] is commonly used to predict the band gap and other electronic properties, PBE0[31] and X3LYP[32] are prevalent in simulating clusters. On the fifth rung of the ladder are the Random Phase Approximation (RPA)[33] and Double Hybrid Approximation (DHA)[34], and both of them utilized the unoccupied Kohn-Sham orbitals in the exchanged correlation function, owing to the large basis sets required, both RPA and DHA demand substantial computing resources, making them impractical for real-world material simulations at current stage. However, in recent years, Dr. Georg Kresse group utilized the direct RPA (dRPA) to predict the Si system and achieve high consistency with the experiment results[35]. Also, Dr. Xu's group developed several DHA models (e.g., xDH-PBE0[36], XYGJ-OS[37]) and achieved high accuracy in predicting the properties of small molecules. Although at present, methods starting from the fourth rung of the ladder (Hybrid, RPA&DHA) are computationally so expensive that it’s almost impossible to leverage them for conducting structure optimization of the materials, with the increasingly rapid development of the GPU computing Hardware and High-performance computing technology, these methods are becoming promising in the future.

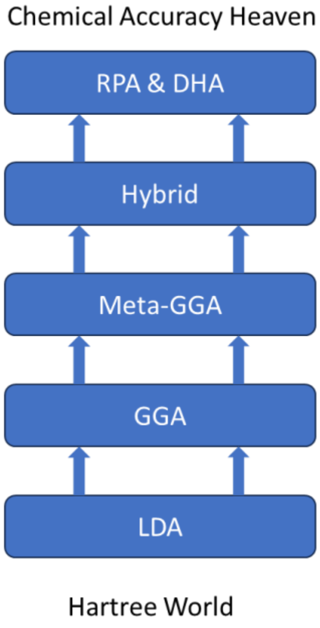

Figure 2.1 Demonstration of Jacob Ladder of DFT[14]

2.6 Basis set

In quantum chemistry calculations, owing to the high-dimensional nature of the electron wave function, obtaining the exact geometry solution of wave function is challenging. Therefore, researchers utilized the basis set, consisting of a set of functions to depict the electronic wave function. The basis set transforms the problem of finding analytical solution of partial differential equations into obtaining numerical solution of algebraic equations which could be easily handled by the computing program. The general equation for the basis set is shown as follows:

$$\psi_i = \sum_{\alpha=1}^{n} c_\alpha f_\alpha \tag{2.9}$$

Where ψ_i is the wave function, c_α is the coefficient for the corresponding basis function f_α. Incorporating more basis function will lead to more accurate results. Based on the exact formula, the basis set can be divided into atomic orbitals (i.e., Gaussian-type orbitals[38]), plane waves[39] and real-space approach[40], that directly focuses on the discrete physical space. Among these gaussian-type basis set and plane waves basis set are prevalent.

2.6.1 Gaussian basis set

Gaussian basis sets are linear combinations of gaussian functions, which are more efficient for molecular integrals computing than slater basis function. Gaussian bases are most used for molecules and clusters. The prevalent minimal Gaussian basis sets are the Slater-type Orbitals (STO-nG) series[41], where n in the notation refers to the number of Gaussian primitive functions incorporated. Although the STO-nG basis sets have high efficiency, the accuracy of the results is relatively low in that these methods only incorporate one contracted gaussian orbitals. In 1970, Dr. John Anthony Pople developed the split-valence basis sets[42] considering the fact that valence electrons participating the formation of chemical bonds. The method depicts each valence electron orbital by a linear combination of Gaussian functions. Among split-valence bases, the 6-31G*[43, 44] is a standard that balance the efficiency and accuracy as a medium basis set. To improve the accuracy when simulating the Core-to-Core or Core-to-Valence interaction using correlated wave functions, researchers developed the Correlation-consistent basis sets[45, 46], in which cc-pVNZ[47] were utilized for lighter elements while cc-pVXZ/cc-pVXZ-PP[48, 49] were adopted for heavier elements.

2.6.2 Plane wave basis set

In contrast to Gaussian basis set, the plane wave basis sets are most commonly used for simulating the periodic boundary models (i.e., solid materials). In the plane wave basis set, each wave function is generally represented by a linear combination of periodic functions, which are named as plane waves. The plane wave functions are orthogonal to each other, and these functions are not correlated to specific atoms. The accuracy of the plane wave basis set in DFT calculations depends on the choice of the cut-off energy, or truncate energy. Dr. Blöchl put forward the Projector-Augmented-Wave method[50, 51], which incorporates both linear augmented-plane-wave (LAPW) method and pseudopotential method. The wave functions near nucleus in Hilbert space have strong oscillations, which make the numeric computing low efficient. The PAW method transfers the oscillating wave functions into smooth functions, significantly improving the speed of the numeric computation.

2.7 Pseudopotential (PP)

When simulating the system containing heavy elements (i.e., transition metals), solving for the wave functions and electron density for all the electrons is time consuming and cumbersome. In 1934, Dr. Hans Gustav Adolf Hellmann introduced the idea of pseudopotential which leverage the effective potential to represent the effect of the core electrons[52]. By using the PP, DFT calculations will only solve for the density of the valence electrons, and this approximation dramatically reduces the size of the basis set. At present, there are 2 most prevalent Pseudopotentials: Norm-conserving PP[53] and Ultrasoft PP[54]. Norm-conserving requires larger basis sets than Ultrasoft PP, therefore it’s very cumbersome when dealing with transitional metals. In contrast, Ultrasoft PP releases the strictly norm-conserving restraint, greatly reduce the basis set requirement.

2.8 Dispersion Correction of Density Functional Theory (DFT+D)

The accuracy of the density functional Theory depends on the choice of the exchange-correlation function. Local Spin-Density Approximation (LSD) and semi-local generalized Gradient Approximation (GGA) still didn’t consider the non-covalent interactions. These long-range interactions are of vital importance in simulating layered materials, surface chemistry, and biomolecules. Therefore, incorporating dispersion correction is necessary to DFT for accurately simulating the properties of both solid materials and molecules. To handle the deficiency of the LSD and GGA for the long-range electron interactions. Dr. Stefan Grimme’s group developed the empirical dispersion corrections (DFT+D)[55-57]. The DFT+D dispersion theory combines the Kohn-Sham energy $\mathrm{E_{KS\text{-}DFT}}$ from DFT with the dispersion energy $\mathrm{E_{disp}}$ to form the total energy $\mathrm{E_{DFT\text{-}D}}$, which is shown as the following equation[55]:

$$\mathrm{E_{DFT\text{-}D} = E_{KS\text{-}DFT} + E_{disp}} \tag{2.10}$$

In DFT+D2[55], the strategy is to limit the DFT energy to focus mainly on the short-range interactions while leave the long-range interactions to the damped $\mathrm{\frac{C_6^{mn}}{R_{mn}^6}}$ part. Where the $\mathrm{E_{disp}}$ is the empirical term representing the dispersion energy and this correction term could be calculated as the equation shown below[55]:

$$\mathrm{E_{disp} = \text{-}s_6 \sum_{m=1}^{N_{atom}\text{-}1} \sum_{n=m+1}^{N_{atom}} \frac{C_6^{mn}}{R_{mn}^6} f_{dmp}(R_{mn})} \tag{2.11}$$

Where $\mathrm{s_6}$ is the global scaling factor, $\mathrm{N_{atom}}$ refers to the total number of atoms in the system, $\mathrm{C_6^{mn}}$ is the dispersion coefficient between atom m and n, $\mathrm{R_{mn}}$ is the distance between atom m and n, the fermi-type damping function $\mathrm{f_{dmp}}$ was utilized as the equation (2.12):

$$\mathrm{f_{dmp}\left(R_{ij}\right) = \frac{1}{1 + e^{\text{-}d(\frac{R_{ij}}{R_r}\text{-}1)}}} \tag{2.12}$$

Where the $\mathrm{R_r}$ is the sum of the atomic van der Waals radius of atom m and n:

$$\mathrm{R_r = R_{0m} + R_{0n}} \tag{2.13}$$

Also, the dispersion coefficient C_6^{mn} would be calculated using the combination rules:

$$C_6^{mn} = \sqrt{C_6^m C_6^n} \tag{2.14}$$

To further improve the accuracy of the DFT+D2 method, Dr. Grimme combined the three-body energy term with the two-body term in the dispersion energy:

$$E_{disp} = E_{twoBody} + E_{threeBody} \tag{2.15}$$

For the 2-body term, higher-ranked multipole term $n = 8$ is also considered, the two-body term could be represented as follows:

$$E_{twoBody} = - \sum_{m=1}^{N_{atom}-1} \sum_{n=m+1}^{N_{atom}} \left(s_6 \frac{C_6^{mn}}{R_{mn}^6} f_{dmp,6}(R_{mn}) + s_8 \frac{C_8^{mn}}{R_{mn}^8} f_{dmp,8}(R_{mn})\right) \tag{2.16}$$

For the 3-body term, the dispersion energy is derived from the Axilrod–Teller–Muto nonadditive term by using the third-order perturbation theory[58]:

$$E^{ABC} = \frac{C_9^{ABC}(\cos\theta_a \cos\theta_b \cos\theta_c + 1)}{(r_{AB} r_{BC} r_{AC})^3} \tag{2.17}$$

As is shown by the Scheme of the three-body system (**Figure 2.2**), the θ_a, θ_b and θ_c refers to the angle BAC, ACB and CBA, respectively. And the C_9^{ABC} is the triple-dipole coefficient.

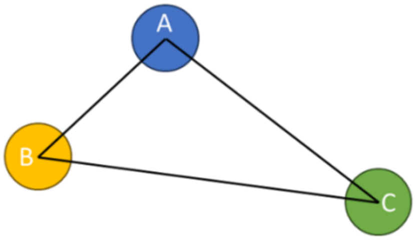

Figure 2.2 Scheme of the three-body system

By adopting the damping function to the 3-body energy the ultimate 3-body term could be written as:

$$E_{twoBody} = - \sum_{k=1}^{N_{threeBodyPairs}} f_{dmp,threeBody} E^{ABC} \qquad (2.18)$$

The DFT+D3 method could obtain around CCSD(T) level of accuracy and solve the issue of overestimation of midrange dispersion encountered by DFT-D2 when dealing with the carbon systems. The high accuracy of DFT+D3 sacrifices the efficiency since incorporating the three-body term require the computing time complexity of $O(n^3)$.[57]

2.9 Transition State Theory (TST)

TST is used to describe the speed of the chemical elementary reactions. In 1889, inspired by the Van't Hoff equation, which built the relationships between the equilibrium constant and the temperature, Swedish scientist Svante August Arrhenius proposed the Arrhenius rate law[59] which could be used to obtain the chemical reaction rate constant based on the absolute temperature, the formula of the Arrhenius law is shown as the equation (2.19):

$$k = Ae^{\frac{-E_a}{RT}} \tag{2.19}$$

Where k is the rate constant, A is the pre-exponential factor and E_a refers to the activation energy. Arrhenius law is based on the empirical experimental observations since both pre-exponential factor and activation energy are obtained from microscopic measurements, which lack mechanical understanding at atomic level. To illuminate the physical nature of the pre-exponential factor and the activation energy, Henry Eyring, Michael Polanyi and Meredith Gwynne Evans proposed the Transition State theory[60,61] . Later, the Arrhenius equation were modified to the following form:[62]:

$$k = \frac{\kappa k_B T}{h} e^{\frac{\Delta S_a}{R}} e^{\frac{-\Delta H_a}{RT}} \tag{2.20}$$

Where κ refers to the transmission coefficient, k_B is the Boltzmann constant, h refers to the Planck constant and ΔS_a , ΔH_a is the entropy difference, enthalpy difference between the reactants and transition state, respectively. By incorporating theΔS_a, ΔH_a into the Gibbs free energy term equation (2.21) could be obtained, and ΔG_a refers to the activation Gibbs free energy.

$$k = \frac{\kappa k_B T}{h} e^{\frac{-\Delta G_a}{RT}} \tag{2.21}$$

The transition state theory describes an intermediate static state which exists between the initial state structure (reactant) and the final state structure (product) along the potential energy surface. This intermediate state lies on the saddle point of the potential energy surface and the Hessian matrix at this point has only one negative eigenvalue. This state is called transitional state and the energy difference between the transitional state and the initial state is the activation energy, which can determine the reaction rate constant.

The transition state search is a set of techniques or methods utilized in computational chemistry to locate the transitional state and the corresponding energy. The state-of-art transition state search method could mainly be divided into single-ended techniques and double-ended techniques[63]. The single-ended techniques take the input initial guess on the transitional structure and optimize for the converged state, including the eigenvector following method[64] in which the optimization direction is along with the that of the negative eigenvectors. The double-ended methods take both the initial reactant structure and the final product structure as input to obtain the transition state, including the climbing image nudged elastic band method (CI-NEB)[65] in which a set of intermediate state images are generated by the linear interpolation between the initial structure and the final structure, one of the images is set to climb up along the elastic band to reach to the saddle point.

2.10 References

(1) Iqbal, A. Some aspects on the Schrödinger equation. **2012**.

(2) Born, M.; Oppenheimer, R. Zur Quantentheorie der Molekeln. *Annalen der Physik* **1927**, *389* (20), 457-484. DOI: 10.1002/andp.19273892002.

(3) Hartree, D. R.; Hartree, W. Self-consistent field, with exchange, for beryllium. *Proceedings of the Royal Society of London. Series A - Mathematical and Physical Sciences* **1935**, *150* (869), 9-33. DOI: 10.1098/rspa.1935.0085.

(4) KÜMMEL, H. G. A BIOGRAPHY OF THE COUPLED CLUSTER METHOD. *International Journal of Modern Physics B* **2003**, *17* (28), 5311-5325. DOI: 10.1142/s0217979203020442.

(5) Møller, C.; Plesset, M. S. Note on an Approximation Treatment for Many-Electron Systems. *Physical Review* **1934**, *46* (7), 618-622. DOI: 10.1103/PhysRev.46.618.

(6) Angeli, C.; Cimiraglia, R.; Evangelisti, S.; Leininger, T.; Malrieu, J.-P. Introduction of n-electron valence states for multireference perturbation theory. *The Journal of Chemical Physics* **2001**, *114* (23), 10252-10264. DOI: 10.1063/1.1361246.

(7) Buenker, R. J.; Peyerimhoff, S. D.; Butscher, W. Applicability of the multi-reference double-excitation CI (MRD-CI) method to the calculation of electronic wavefunctions and comparison with related techniques. *Molecular Physics* **1978**, *35* (3), 771-791. DOI: 10.1080/00268977800100581.

(8) Fermi, E. Eine statistische Methode zur Bestimmung einiger Eigenschaften des Atoms und ihre Anwendung auf die Theorie des periodischen Systems der Elemente. *Zeitschrift für Physik* **1928**, *48* (1), 73-79. DOI: 10.1007/BF01351576.

(9) Thomas, L. H. The calculation of atomic fields. *Mathematical Proceedings of the Cambridge Philosophical Society* **2008**, *23* (5), 542-548. DOI: 10.1017/S0305004100011683.

(10) Baker, E. B. The Application of the Fermi-Thomas Statistical Model to the Calculation of Potential Distribution in Positive Ions. *Physical Review* **1930**, *36* (4), 630-647. DOI: 10.1103/PhysRev.36.630.

(11) Hohenberg, P.; Kohn, W. Inhomogeneous Electron Gas. *Physical Review* **1964**, *136* (3B), B864-B871. DOI: 10.1103/PhysRev.136.B864.

(12) Kohn, W.; Sham, L. J. Self-Consistent Equations Including Exchange and Correlation Effects. *Physical Review* **1965**, *140* (4A), A1133-A1138. DOI: 10.1103/PhysRev.140.A1133.

(13) Perdew, J. P.; Ruzsinszky, A.; Tao, J.; Staroverov, V. N.; Scuseria, G. E.; Csonka, G. I. Prescription for the design and selection of density functional approximations: More

constraint satisfaction with fewer fits. *The Journal of Chemical Physics* **2005**, *123* (6). DOI: 10.1063/1.1904565.

(14) Zhang, I. Y.; Xu, X. On the top rung of Jacob's ladder of density functional theory: Toward resolving the dilemma of SIE and NCE. *WIREs Computational Molecular Science* **2021**, *11* (1), e1490. DOI: 10.1002/wcms.1490.

(15) Lykos, P.; Pratt, G. W. Discussion on The Hartree-Fock Approximation. *Reviews of Modern Physics* **1963**, *35* (3), 496-501. DOI: 10.1103/RevModPhys.35.496.

(16) Kurth, S.; Perdew, J. P.; Blaha, P. Molecular and solid-state tests of density functional approximations: LSD, GGAs, and meta-GGAs. *International Journal of Quantum Chemistry* **1999**, *75* (4-5), 889-909. DOI: 10.1002/(SICI)1097-461X(1999)75:4/5<889::AID-QUA54>3.0.CO;2-8.

(17) Perdew, J. P. Generalized gradient approximations for exchange and correlation: A look backward and forward. *Physica B: Condensed Matter* **1991**, *172* (1), 1-6. DOI: 10.1016/0921-4526(91)90409-8.

(18) Perdew, J. P.; Burke, K.; Ernzerhof, M. Generalized Gradient Approximation Made Simple. *Physical Review Letters* **1996**, *77* (18), 3865-3868. DOI: 10.1103/PhysRevLett.77.3865.

(19) Yuk, S. F.; Lee, M.-S.; Akhade, S. A.; Nguyen, M.-T.; Glezakou, V.-A.; Rousseau, R. First-principle investigation on catalytic hydrogenation of benzaldehyde over Pt-group metals. *Catalysis Today* **2022**, *388-389*, 208-215. DOI: 10.1016/j.cattod.2020.07.039.

(20) Liu, C.; Cundari, T. R.; Wilson, A. K. CO_2 Reduction on Transition Metal (Fe, Co, Ni, and Cu) Surfaces: In Comparison with Homogeneous Catalysis. *The Journal of Physical Chemistry C* **2012**, *116* (9), 5681-5688. DOI: 10.1021/jp210480c.

(21) Sun, G.; Alexandrova, A. N.; Sautet, P. Structural Rearrangements of Subnanometer Cu Oxide Clusters Govern Catalytic Oxidation. *ACS Catalysis* **2020**, *10* (9), 5309-5317. DOI: 10.1021/acscatal.0c00824.

(22) Getsoian, A. B.; Bell, A. T. The Influence of Functionals on Density Functional Theory Calculations of the Properties of Reducible Transition Metal Oxide Catalysts. *The Journal of Physical Chemistry C* **2013**, *117* (48), 25562-25578. DOI: 10.1021/jp409479h.

(23) Schweitzer, B.; Archuleta, C.; Seong, B.; Anderson, R.; Gómez-Gualdrón, D. A. Electronic effects due to organic linker-metal surface interactions: implications on screening of MOF-encapsulated catalysts. *Physical Chemistry Chemical Physics* **2020**, *22* (4), 2475-2487. DOI: 10.1039/C9CP05380H.

(24) Whitford, C. L.; Stephenson, C. J.; Gómez-Gualdrón, D. A.; Hupp, J. T.; Farha, O. K.; Snurr, R. Q.; Stair, P. C. Elucidating the Nanoparticle–Metal Organic Framework Interface of Pt@ZIF-8 Catalysts. *The Journal of Physical Chemistry C* **2017**, *121* (45), 25079-25091. DOI: 10.1021/acs.jpcc.7b06773.

(25) Adamo, C.; Ernzerhof, M.; Scuseria, G. E. The meta-GGA functional: Thermochemistry with a kinetic energy density dependent exchange-correlation functional. *The Journal of Chemical Physics* **2000**, *112* (6), 2643-2649. DOI: 10.1063/1.480838.

(26) Tao, J.; Perdew, J. P.; Staroverov, V. N.; Scuseria, G. E. Climbing the Density Functional Ladder: Nonempirical Meta--Generalized Gradient Approximation Designed for Molecules and Solids. *Physical Review Letters* **2003**, *91* (14), 146401. DOI: 10.1103/PhysRevLett.91.146401.

(27) Hohenstein, E. G.; Chill, S. T.; Sherrill, C. D. Assessment of the Performance of the M05−2X and M06−2X Exchange-Correlation Functionals for Noncovalent Interactions in Biomolecules. *Journal of Chemical Theory and Computation* **2008**, *4* (12), 1996-2000. DOI: 10.1021/ct800308k.

(28) Sun, J.; Remsing, R. C.; Zhang, Y.; Sun, Z.; Ruzsinszky, A.; Peng, H.; Yang, Z.; Paul, A.; Waghmare, U.; Wu, X.; et al. Accurate first-principles structures and energies of diversely bonded systems from an efficient density functional. *Nature Chemistry* **2016**, *8* (9), 831-836. DOI: 10.1038/nchem.2535.

(29) Černý, J.; Hobza, P. Non-covalent interactions in biomacromolecules. *Physical Chemistry Chemical Physics* **2007**, *9* (39), 5291-5303. DOI: 10.1039/B704781A.

(30) Heyd, J.; Scuseria, G. E. Efficient hybrid density functional calculations in solids: Assessment of the Heyd–Scuseria–Ernzerhof screened Coulomb hybrid functional. *The Journal of Chemical Physics* **2004**, *121* (3), 1187-1192. DOI: 10.1063/1.1760074.

(31) Elm, J.; Bilde, M.; Mikkelsen, K. V. Assessment of binding energies of atmospherically relevant clusters. *Physical Chemistry Chemical Physics* **2013**, *15* (39), 16442-16445. DOI: 10.1039/C3CP52616J.

(32) Su, J. T.; Xu, X.; Goddard, W. A. Accurate Energies and Structures for Large Water Clusters Using the X3LYP Hybrid Density Functional. *The Journal of Physical Chemistry A* **2004**, *108* (47), 10518-10526. DOI: 10.1021/jp047502+.

(33) Anderson, P. W. Random-Phase Approximation in the Theory of Superconductivity. *Physical Review* **1958**, *112* (6), 1900-1916. DOI: 10.1103/PhysRev.112.1900.

(34) Toulouse, J.; Sharkas, K.; Brémond, E.; Adamo, C. Communication: Rationale for a new class of double-hybrid approximations in density-functional theory. *The Journal of Chemical Physics* **2011**, *135* (10). DOI: 10.1063/1.3640019.

(35) Kaltak, M.; Klimeš, J.; Kresse, G. Cubic scaling algorithm for the random phase approximation: Self-interstitials and vacancies in Si. *Physical Review B* **2014**, *90* (5), 054115. DOI: 10.1103/PhysRevB.90.054115.

(36) Zhang, I. Y.; Su, N. Q.; Brémond, É. A. G.; Adamo, C.; Xu, X. Doubly hybrid density functional xDH-PBE0 from a parameter-free global hybrid model PBE0. *The Journal of Chemical Physics* **2012**, *136* (17). DOI: 10.1063/1.3703893.

(37) Zhang, I. Y.; Xu, X.; Jung, Y.; Goddard, W. A. A fast doubly hybrid density functional method close to chemical accuracy using a local opposite spin ansatz. *Proceedings of the National Academy of Sciences* **2011**, *108* (50), 19896-19900. DOI: 10.1073/pnas.1115123108.

(38) Gill, P. M. W. Molecular integrals Over Gaussian Basis Functions. In *Advances in Quantum Chemistry* **1994**, 25, 141-205. DOI: 10.1016/S0065-3276(08)60019-2.

(39) Paier, J.; Hirschl, R.; Marsman, M.; Kresse, G. The Perdew–Burke–Ernzerhof exchange-correlation functional applied to the G2-1 test set using a plane-wave basis set. *The Journal of Chemical Physics* **2005**, *122* (23). DOI: 10.1063/1.1926272.

(40) Andrade, X.; Aspuru-Guzik, A. Real-Space Density Functional Theory on Graphical Processing Units: Computational Approach and Comparison to Gaussian Basis Set Methods. *Journal of Chemical Theory and Computation* **2013**, *9* (10), 4360-4373. DOI: 10.1021/ct400520e.

(41) Pietro, W. J.; Levi, B. A.; Hehre, W. J.; Stewart, R. F. Molecular orbital theory of the properties of inorganic and organometallic compounds. 1. STO-NG basis sets for third-row main-group elements. *Inorganic Chemistry* **1980**, *19* (8), 2225-2229. DOI: 10.1021/ic50210a005

(42) Ditchfield, R.; Hehre, W. J.; Pople, J. A. Self-Consistent Molecular-Orbital Methods. IX. An Extended Gaussian-Type Basis for Molecular-Orbital Studies of Organic Molecules. *The Journal of Chemical Physics* **2003**, *54* (2), 724-728. DOI: 10.1063/1.1674902.

(43) Rassolov, V. A.; Pople, J. A.; Ratner, M. A.; Windus, T. L. 6-31G* basis set for atoms K through Zn. *The Journal of Chemical Physics* **1998**, *109* (4), 1223-1229. DOI: 10.1063/1.476673.

(44) Rassolov, V. A.; Ratner, M. A.; Pople, J. A.; Redfern, P. C.; Curtiss, L. A. 6-31G* basis set for third-row atoms. *Journal of computational chemistry* **2001**, *22* (9), 976-984. DOI: 10.1002/jcc.1058.

(45) Dunning, T. H., Jr. Gaussian basis sets for use in correlated molecular calculations. I. The atoms boron through neon and hydrogen. *The Journal of Chemical Physics* **1989**, *90* (2), 1007-1023. DOI: 10.1063/1.456153.

(46) Hill, J. G.; Mazumder, S.; Peterson, K. A. Correlation consistent basis sets for molecular core-valence effects with explicitly correlated wave functions: The atoms B–Ne and Al–Ar. *The Journal of Chemical Physics* **2010**, *132* (5). DOI: 10.1063/1.3308483.

(47) Bready, C. J.; Fowler, V. R.; Juechter, L. A.; Kurfman, L. A.; Mazaleski, G. E.; Shields, G. C. The driving effects of common atmospheric molecules for formation of prenucleation clusters: the case of sulfuric acid, formic acid, nitric acid, ammonia, and dimethyl amine. *Environmental Science: Atmospheres* **2022**, *2* (6), 1469-1486. DOI: 10.1039/D2EA00087C.

(48) Peterson, K. A.; Yousaf, K. E. Molecular core-valence correlation effects involving the post-d elements Ga–Rn: Benchmarks and new pseudopotential-based correlation consistent basis sets. *The Journal of Chemical Physics* **2010**, *133* (17). DOI: 10.1063/1.3503659.

(49) Woon, D. E.; Dunning, T. H., Jr. Gaussian basis sets for use in correlated molecular calculations. III. The atoms aluminum through argon. *The Journal of Chemical Physics* **1993**, *98* (2), 1358-1371. DOI: 10.1063/1.464303.

(50) Blöchl, P. E. Projector augmented-wave method. *Physical Review B* **1994**, *50* (24), 17953-17979. DOI: 10.1103/PhysRevB.50.17953.

(51) Blöchl, P. E.; Först, C. J.; Schimpl, J. Projector augmented wave method:ab initio molecular dynamics with full wave functions. *Bulletin of Materials Science* **2003**, *26* (1), 33-41. DOI: 10.1007/BF02712785.

(52) Schwerdtfeger, P. The Pseudopotential Approximation in Electronic Structure Theory. *ChemPhysChem* **2011**, *12* (17), 3143-3155. DOI: 10.1002/cphc.201100387.

(53) Hamann, D. R.; Schlüter, M.; Chiang, C. Norm-Conserving Pseudopotentials. *Physical Review Letters* **1979**, *43* (20), 1494-1497. DOI: 10.1103/PhysRevLett.43.1494.

(54) Kresse, G.; Joubert, D. From ultrasoft pseudopotentials to the projector augmented-wave method. *Physical Review B* **1999**, *59* (3), 1758-1775. DOI: 10.1103/PhysRevB.59.1758.

(55) Grimme, S. Semiempirical GGA-type density functional constructed with a long-range dispersion correction. *Journal of computational chemistry* **2006**, *27* (15), 1787-1799. DOI: 10.1002/jcc.20495.

(56) Grimme, S. Accurate description of van der Waals complexes by density functional theory including empirical corrections. *Journal of computational chemistry* **2004**, *25* (12), 1463-1473. DOI: 10.1002/jcc.20078.

(57) Grimme, S.; Antony, J.; Ehrlich, S.; Krieg, H. A consistent and accurate ab initio parametrization of density functional dispersion correction (DFT-D) for the 94 elements H-Pu. *The Journal of Chemical Physics* **2010**, *132* (15). DOI: 10.1063/1.3382344.

(58) Axilrod, B.; Teller, E. Interaction of the van der Waals type between three atoms. *The Journal of Chemical Physics* **1943**, *11* (6), 299-300. DOI: 10.1063/1.1723844

(59) Arrhenius, S. Über die Dissociationswärme und den Einfluss der Temperatur auf den Dissociationsgrad der Elektrolyte. *Zeitschrift für Physikalische Chemie* **1889**, *4U* (1), 96-116. DOI: 10.1515/zpch-1889-0408.

(60) Eyring, H. The Activated Complex in Chemical Reactions. *The Journal of Chemical Physics* **1935**, *3* (2), 107-115. DOI: 10.1063/1.1749604.

(61) Evans, M. G.; Polanyi, M.; Some applications of the transition state method to the calculation of reaction velocities, especially in solution. *Transactions of the Faraday Society* **1935**, *31*, 875-894. DOI: 10.1039/TF9353100875.

(62) Laidler, K. J.; King, M. C. Development of transition-state theory. *The Journal of Physical Chemistry* **1983**, *87* (15), 2657-2664. DOI: 10.1021/j100238a002.

(63) Schlegel, H. B. Geometry optimization. *WIREs Computational Molecular Science* **2011**, *1* (5), 790-809. DOI: 10.1002/wcms.34.

(64) Kumeda, Y.; Wales, D. J.; Munro, L. J. Transition states and rearrangement mechanisms from hybrid eigenvector-following and density functional theory.: Application to C10H10 and defect migration in crystalline silicon. *Chemical Physics Letters* **2001**, *341* (1), 185-194. DOI: 10.1016/S0009-2614(01)00334-7.

(65) Henkelman, G.; Uberuaga, B. P.; Jónsson, H. A climbing image nudged elastic band method for finding saddle points and minimum energy paths. *The Journal of Chemical Physics* **2000**, *113* (22), 9901-9904. DOI: 10.1063/1.1329672.

Chapter 3. Single-Atoms Anchored in Hexagonal Boron Nitride for Propane Dehydrogenation from First Principles

3.1 Abstract

Single-atom catalysts embedded in N-doped graphene have attracted great interest recently, but the hexagonal boron nitride (h-BN) is much less explored as a support. Using first principles density function theory and molecular dynamics, here we investigate the stability of Pt, Au, and Ru Single-Atoms anchored at B and N vacancies on h-BN. We find that Pt and Ru Single-Atoms are much more stable than Au on h-BN. We further examine propane dehydrogenation on these single-atom catalysts and find that Pt_1 at the B vacancy in h-BN and Ru_1 at the N vacancy in h-BN show excellent activity for propane dehydrogenation, as evidenced by low energy barriers for both dehydrogenation steps. Our work suggests that Pt and Ru Single-Atoms anchored at vacancy sites in h-BN could be promising for propane dehydrogenation.

3.2 Introduction

Single-Atom catalysis has attracted great interest in heterogeneous catalysis in the past decade.[1] Doped graphene is a widely used substrate to support metal Single-Atoms due to the excellent metal-support interaction,[2] high specific surface area,[3] and high electron conductivity.[4] For example, it was found that the FeN_4 center and the N-group in graphene can enhance oxygen reduction reaction,[5] while Co Single-Atoms on N-doped graphene show high activity and stability in hydrogen evolution reaction.[6]

As two prototypical 2D materials, graphene and hexagonal boron nitride (h-BN) share many properties. Hence, h-BN can be a potential candidate for anchoring Single-Atoms, especially at high temperatures due to its high thermal stability. In fact, Hermans and co-workers reported that boron nitride itself is an excellent catalyst for alkane oxidative dehydrogenation with a high propene selectivity.[7, 8] Moreover, Uosaki et al. found that the interface between Au(111) and boron nitride nanosheet can promote oxygen reduction reaction.[9] Researchers also were able to resolve defect sites in boron nitride.[10] Dai and coworkers synthesized ultrathin h-BN sheets with plenty of vacancies sites and found that the h-BN supported Pt nanoparticles have higher activity for CO oxidation than silica-supported Pt.[11, 12]

Although h-BN-supported Single-Atoms have not been reported experimentally, researchers have computationally examined them for catalytic reactions, such as CO oxidation.[13-18] More interestingly, Zhao and Chen predicted that h-BN-supported Mo Single-Atom is a potential catalyst for electrocatalytic N_2 reduction,[19] while Deng et al. suggested that Co embedded in h-BN may be promising for oxygen reduction reaction.[20] One thing to note is that these studies focused on only the B vacancy, but N vacancy has been observed experimentally in h-BN as well.[21]

Recently the h-BN nanosheets have also been explored as a support for Pt nanoparticles[22] and Pt/Cu nanoclusters[23] for direct dehydrogenation of propane on a benchtop scale. Oxide-supported Pt nanoparticles are used commercially in direct dehydrogenation of propane[24] which has been subject to a plethora of experimental studies. It has been shown that Pt exists as nanoclusters of 15 – 25 atoms on the oxide support.[25] Owing to its high surface area and good thermal stability, γ-Al_2O_3 is the most commonly used support for Pt nanoparticles, but its acid sites can contribute to coke formation.[26] Therefore, alloying elements such as Sn have been used to form intermetallic nanoparticles with Pt to avoid coking.[24] Moreover, Pt Single-Atoms have been observed together with larger clusters on oxide support,[25] prompting the speculation that they might be able to catalyze propane dehydrogenation (PDH).[24] Indeed, recent studies have demonstrated the excellent performance of Pt Single-Atoms for PDH, either as single-atom alloys on oxides[27] or isolated atoms anchored in dealuminated zeolite.[28]

The experimental findings of Pt Single-Atoms for PDH have inspired many recent computational studies in exploring Pt Single-Atoms for PDH beyond the oxide supports. Density function theory calculations predicted that Single-Atom Pt on N-doped graphene enhances the Pt's activity in direct dehydrogenation of propane.[29] On the other hand, using Pt Single-Atoms can maximize atomic efficiency[1] and boost turnover[30]. In addition to Pt,[1, 31] Au,[32, 33] and Ru[34, 35] are also popular single-atom systems. When combined with a thermally stable support such as h-BN, these SACs may offer attractive advantages for dehydrogenation of propane, especially in anti-coking and in improving the turnover frequency per Pt atom, as coke formation[36] is a known problem for the conventional Pt/alumina catalyst where Pt exists as nanoclusters of 15 – 25 atoms.[25] Answering these questions computationally can help guide the experimental discovery of h-BN-supported

Single-Atoms for PDH. Hence, herein we investigate from first principles the stability of these Single-Atoms anchored on both N and B vacancies on h-BN and their activity for propane dehydrogenation. Below we first present the stability results of SACs on h-BN, show their PDH energetics, and detail our computational approach. We further explain the trend from the analyses of partial charges, d-band center, and density of states.

3.3 Results and Discussion

3.3.1 Static stability of Pt, Au, and Ru Single-Atoms on h-BN

Since stability is a critical factor for assessing a catalyst, we first examine the stability of Pt, Au, and Ru Single-Atoms on B/N vacancy sites of the h-BN support. Their optimized structures are shown in **Figure 3.1**. One can see that the Single-Atom is slightly above the plane of h-BN. Judging from the distances of the Single-Atoms to their first coordination shell and their height above the h-BN plane (**Table 3.1**), one can conclude that on the B vacancy Ru has the closest interaction with h-BN and Au the least; on the N vacancy, Au still has the least interaction. The anchoring energies of the Single-Atoms indeed confirm this interaction trend (**Figure 3.2**): Ru has the strongest binding at the B vacancy and Pt the strongest at the N vacancy, while Au has the weakest binding at both vacancies. In addition, Ru's binding at the N vacancy is also very strong and only slightly weaker than that of Pt.

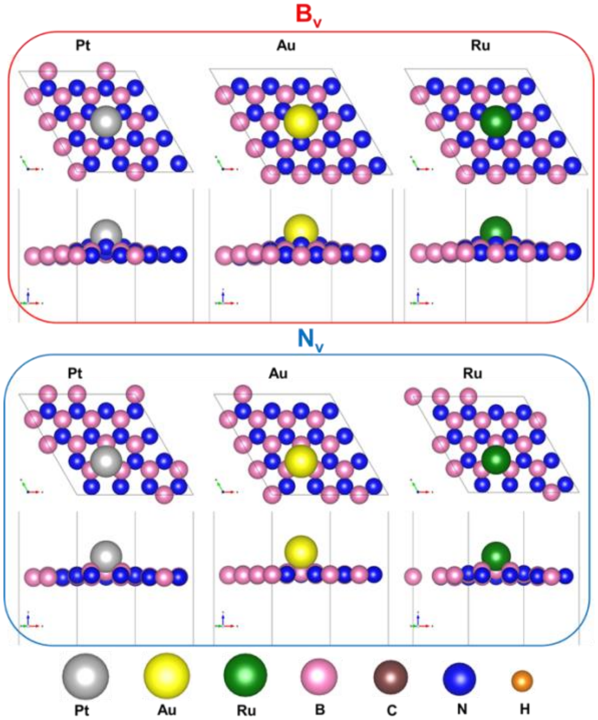

Figure 3.1 DFT-optimized structures of Pt, Au and Ru Single-Atoms anchored on B vacancy (top) and N vacancy (bottom) on h-BN.

Table 3.1 The average M-N (r_{M-N}) distance at the B vacancy and M-B (r_{M-B}) distance at the N vacancy and the height (h) of the Single-Atom M above the h-BN plane in the DFT optimized structures

M	B$_v$		N$_v$	
	r_{M-N} (Å)	h (Å)	r_{M-B} (Å)	h (Å)
Pt	1.97	1.89	2.02	1.81
Au	2.06	2.08	2.27	2.00
Ru	1.92	1.77	2.01	1.91

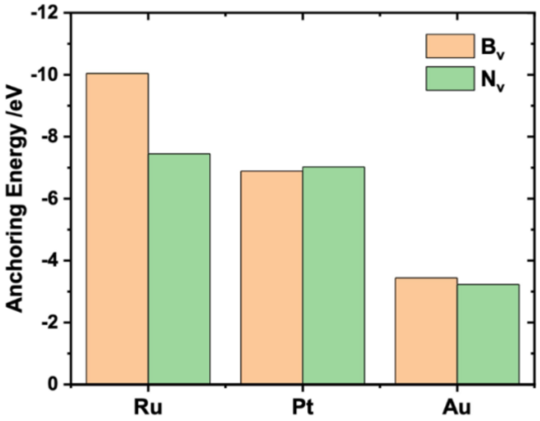

Figure 3.2 Anchoring energy of Pt, Au and Ru Single-Atoms at the B and N vacancies on h-BN.

3.3.2 Dynamic stability of Pt, Au, and Ru Single-Atoms on h-BN

To further examine the dynamic stability of the anchored Single-Atoms, FPMD simulations were carried out at 1000 K to monitor the interaction between the Single-Atoms and h-BN vacancies. As shown in **Figure 3.3**, both Ru and Pt Single-Atoms are more stable at both types of vacancy sites on h-BN than their Au counterparts: the M-B or M-N distances vary within the range of 1.9 to 2.1 Å for Ru and Pt. Au is more stable on the B vacancy than on the N vacancy where the Au-B bond length varies a great deal, from 2.2 to 2.8 Å. The Au-N bond-length at the B vacancy varies from 2.0 to 2.3 Å. In addition, we find that adsorption of C_3H_8 negligibly impacts the stability of the Single-Atoms on the vacancy sites (**Figure 3.10**).

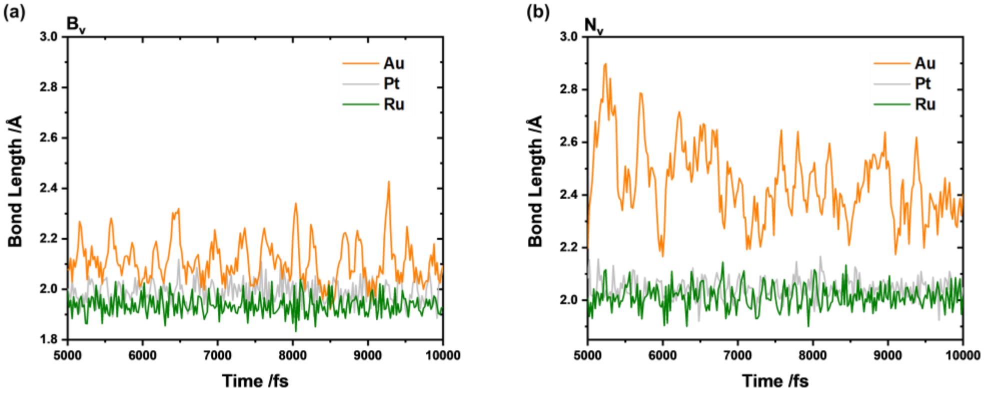

Figure 3.3 Changes in average bond lengths of the Single-Atom (Pt/Au/Ru) to its three nearest N or B atoms on h-BN with time: (a) Single-Atom at the B vacancy; (b) Single-Atom at the N vacancy.

3.3.3 Chemical bonding of Pt, Au, and Ru Single-Atoms on h-BN

To gain a deeper insight into the nature of the chemical bond between the Pt/Au/Ru Single-Atom and the local environment on h-BN, we analyzed the crystal orbital Hamilton population (COHP) for one M-N bond at the B vacancy and one M-B bond at the N vacancy, which partitions the orbital overlapping between two atoms into bonding and antibonding states. The negative -COHP value refers to antibonding states while positive value refers to bonding states. As can be seen in **Figure 3.4**, both Au-B and Au-N bonds have the most antibonding population below the Fermi level, consistent with the weakest binding of Au with h-BN among the three metals. The integrated crystal orbital Hamilton population (ICOHP) up to the Fermi level provides a quantitative measure of the bonding vs antibonding population: the more negative the ICOHP value, the stronger the bonding. Indeed, one can see the overall correlation between the ICOHP values and the anchoring energy of the Single-Atoms on h-BN (**Figure 3.5**). If we compare just Au at B_V and Au at N_V, then the correlation is not good. We think that this is mainly due to the very weak interaction between Au and the defected BN. In other words, because the interaction of Au with h-BN is very weak at both B_V and N_V, variation in ICOHP is not significant enough to differentiate the two sites.

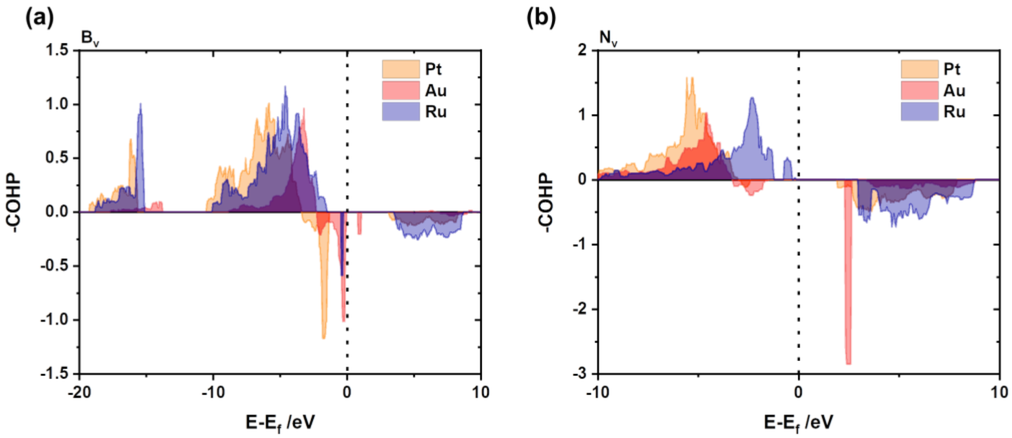

Figure 3.4 Crystal orbital Hamilton population (COHP) analysis of the Single-Atom metal and adjacent N/B atom (Ef denoting the energy of the Fermi level): (a) at the B vacancy; (b) at the N vacancy.

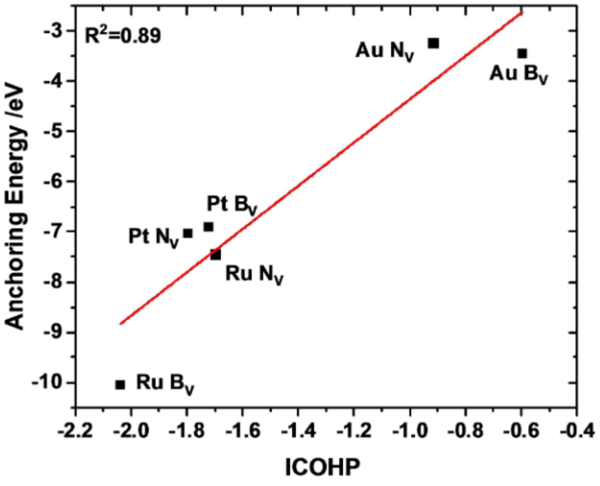

Figure 3.5 Correlation of the Pt/Au/Ru single-atom (M) anchoring energy on the B vacancy (B_V) and N vacancy (N_V) of h-BN with the corresponding integrated crystal orbital Hamilton population (ICOHP) of the M-N and M-B bonds.

We further examined the partial atomic charges of the Pt/Au/Ru Single-Atoms by Bader analysis[37] and found that they are positively charged at the B vacancy but negatively charged at the N vacancy. This is consistent with the electronegativity trend: at the B vacancy, the metal atom is coordinated by the more electronegative N atoms, so loses some of its electrons; at the N vacancy, the metal atom is coordinated by the less electronegative B atoms and gains some electrons. Moreover, Pt is most negative at the N vacancy site, while Ru is most positive at the B vacancy site.

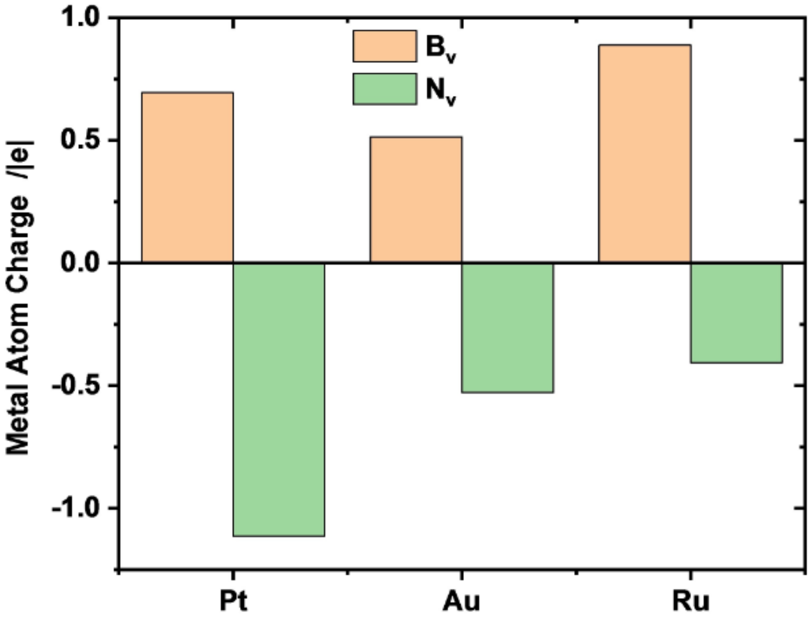

Figure 3.6 Bader charges of the Pt, Au and Ru Single-Atoms anchored at the B vacancy (B_V) and N vacancy (N_V) sites of h-BN.

3.3.4 Propane dehydrogenation activity of the Single-Atom on h-BN

To explore the potential of the M_1-h-BN for catalysis, we chose propane dehydrogenation as a test reaction. **Figure 3.7** shows the energetic profiles and the corresponding key structures during the reaction pathways. The reaction can be divided into three key steps: i. C-H activation at the center carbon; ii. Second dehydrogenation at a terminal carbon; iii. Desorption of H_2 and C_3H_6. For M_1 anchored at the B vacancy (**Figure 3.7a**), Pt is the most active; for M_1 anchored at the N vacancy (**Figure 3.7c**), Ru is the most active, for both dehydrogenation steps. We note that the first dehydrogenation step of propane has a barrier of 0.51 eV at Pt_1-B_V-h-BN; for comparison, the barrier is 0.70 eV on Pt(111) [38] and 0.81 eV on Ru_1-N_V-h-BN. In addition, the intermediate states and transition states are similar on Pt_1-B_V-h-BN (**Figure 3.7b**) and Ru_1-N_V-h-BN (**Figure 3.7d**): C_3H_8 adsorbs on M_1; then C-H cleaves at TS1, leading to CH_3CHCH_3 and H co-adsorbed on M_1; next, second C-H cleaves at TS2, leading to CH_2CHCH_3 (propene) and 2H co-adsorbed on M_1; then, 2H desorbs as H_2, followed by propene desorption. Because propane dehydrogenation usually takes place at high temperatures about 900 K,[24] desorption steps should not be a main concern here. But Au Single-Atom is unlikely to survive such high temperature, considering its anchoring energy and stability (**Figures 3.2** and **3.3**).

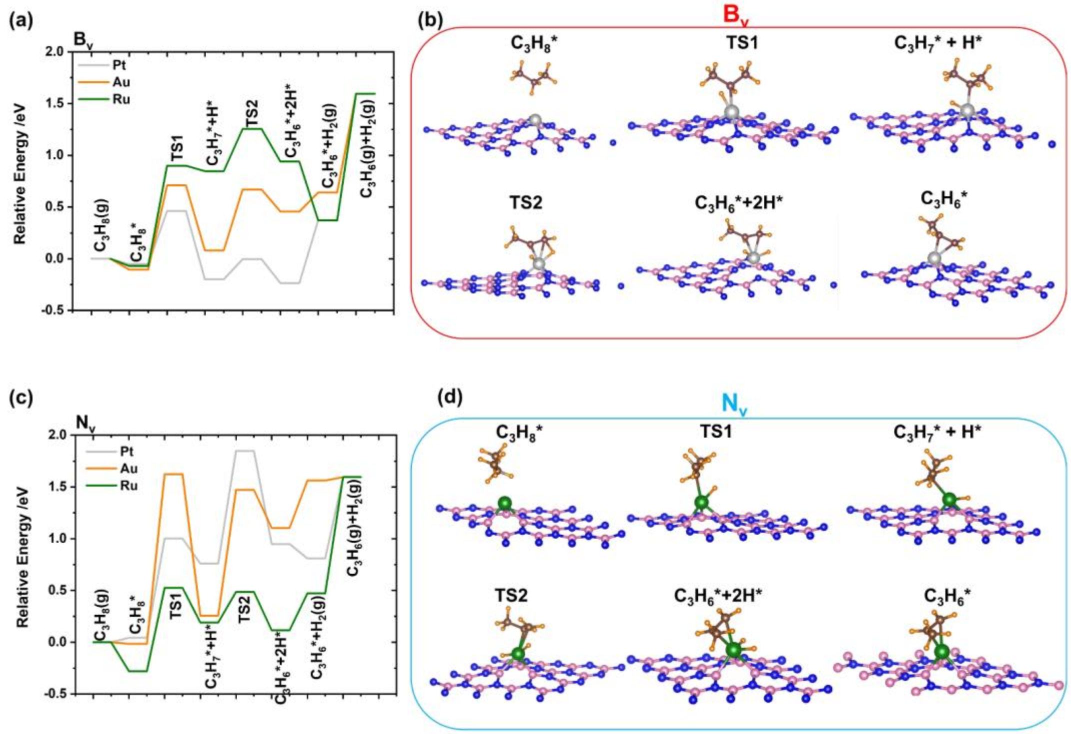

Figure 3.7 Propane dehydrogenation energy profile and the corresponding structures along the pathway: (a) energy profiles for M_1-B_V-h-BN; (b) structures for Pt_1-B_V-h-BN; (c) energy profiles for M_1-N_V-h-BN; (d) structures for Ru_1-N_V-h-BN.

As shown in **Figure 3.7**, the first C-H cleavage and the corresponding activation energy at TS1 are key to propane dehydrogenation. Overall, E_a at TS1 follows the Bell–Evans–Polanyi (BEP) principle: the more favorable the reaction energy (ΔE) is, the lower the activation energy. The only exception is Au_1-N_V-h-BN where E_a is the greatest (~1.6 eV) despite a slightly positive ΔE (~0.25 eV). To understand this exception of Au_1-N_V-h-BN, we have compared its d-band center with others (**Figure 3.8**). One can see that there is a large down shift in the d-band center of Au_1 in Au_1-N_V-h-BN at TS1 (**Figure 3. 8b**), meaning that Au_1 becomes much less reactive during the C-H cleavage process, which we think is the reason for its greatest E_a.

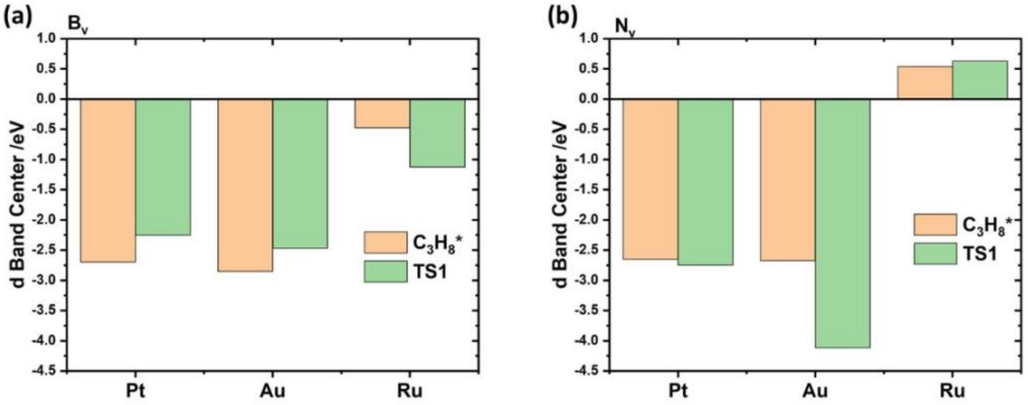

Figure 3.8 The center of the d-band of the metal Single-Atom in the C_3H_8-adsorbed state (C_3H_8*) and at the transition of the first C-H cleavage (TS1): (a) Pt_1-B_V-h-BN; (b) M_1-N_V-h-BN.

3.3.5 Further considerations for experimental relevance

Although Pt_1 at the B vacancy and Ru_1 at the N vacancy of h-BN show great promise for PDH, factors such as sintering, coke formation, and desorption of propylene may negatively impact their experimental realization. Computationally, the sintering question can be addressed by examining the relative stability of metal clusters vs a Single-Atom on defected h-BN, while the susceptibility to coke formation can be addressed by investigating the kinetics of further dehydrogenation tendencies and subsequent formation of aromatic compounds. The importance of propylene desorption is best addressed by microkinetic analysis of the whole PDH pathways. Further studies are warranted.

3.4 Conclusions

We have investigated the stability and propane dehydrogenation reactivity of Pt, Au and Ru singles atoms anchored at vacancy sites of h-BN from first principles DFT calculations. We found that the stability of Au Single-Atom is much lower than that of Pt or Ru. The stability has been correlated to the integrated crystal orbital Hamilton population value, while Bader analysis showed opposite charges on the Single-Atom for B vacancy vs N vacancy as the anchoring site. From the minimum-energy paths of propane dehydrogenation on these single-atom catalysts, we found that Pt_1 at the B vacancy in h-BN and Ru_1 at the N vacancy in h-BN have the lowest barriers for both dehydrogenation steps. Hence, we predict that Pt and Ru Single-Atoms anchored at vacancy sites in h-BN are promising catalysts for propane dehydrogenation.

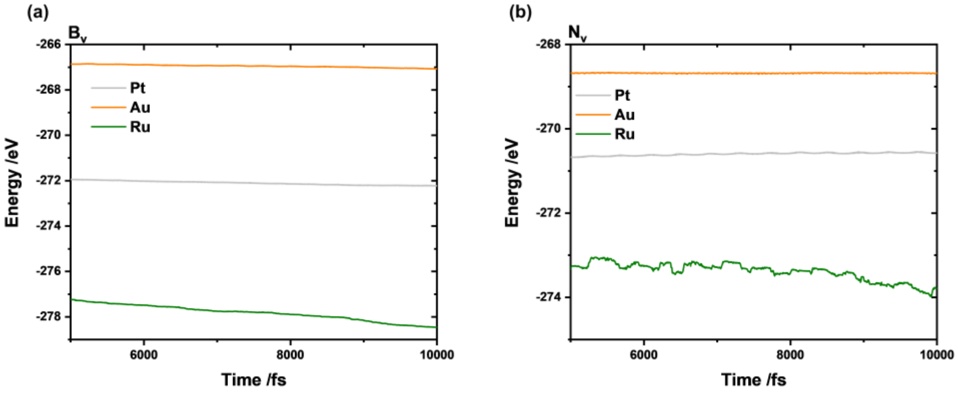

Figure 3.9 Changes in the total energy of the Single-Atom (Pt/Au/Ru) M-BN catalyst in the first principles molecular dynamics simulations: (a) Single-Atom at the B vacancy; (b) Single-Atom at the N vacancy.

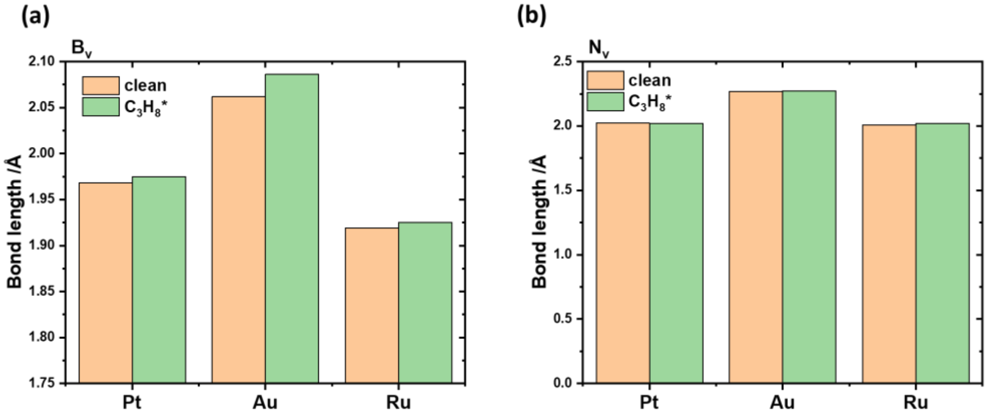

Figure 3.10 Average bond length between the Single-Atom M and B/N atom before (clean) and after the adsorption of C_3H_8: (a) M_1-B_V-h-BN; (b) M_1-N_V-h-BN.

3.5 Computational Methods

First principles density function theory (DFT) calculations were carried out via Vienna Ab initio Simulation Package (VASP).[39] Spin-polarized calculations were performed with the Perdew, Burke, and Ernzerhof (PBE) exchange-correlation functional.[40] The electron-ion interaction was described by projector augmented wave potentials.[41] The cutoff energy of the plane wave basis set was 400 eV. The Brillouin zone sampling was carried out by using a 3×3×1 k-point mesh for a single layer h-BN with a 4×4 lateral unit cell. A vacuum layer ~20 Å along the c-direction was used in our slab models. For density of states calculation, a 5×5×1 k-point mesh was utilized. Convergence criterion was 0.05 eV/Å for both geometry optimization and transition state search. All atoms were relaxed during geometry optimization.

Single-Atom anchoring energy was calculated following $\mathrm{E_{SAC}} = \mathrm{E_{total}}$-$\mathrm{E_{SA}}$-$\mathrm{E_v}$, where $\mathrm{E_{total}}$ denotes the total energy of h-BN-supported Single-Atom, $\mathrm{E_{SA}}$ the energy of a gas-phase Single-Atom, and $\mathrm{E_v}$ the energy of h-BN surface with a B or N vacancy. The climbing-image nudged elastic band (CI-NEB) method[42] was used to search for the transition states.

First principles molecular dynamic (FPMD) simulations were performed in 10 ps timescale at constant 1000 K with the NVT ensemble and a time step of 1 fs. The energy drifts of the systems are shown in **Figure 3.9**. Analysis of crystal orbital Hamiltonian populations was carried out using the Local orbital Basis Suite towards Electronic-Structure Reconstruction (LOBSTER) program (version 3.2.0),[43, 44] which uses as input the charge density and wavefunction files from VASP calculations.

3.6 References

(1) Qiao, B.; Wang, A.; Yang, X.; Allard, L. F.; Jiang, Z.; Cui, Y.; Liu, J.; Li, J.; Zhang, T. Single-atom catalysis of CO oxidation using Pt1/FeOx. *Nature Chemistry* **2011**, *3* (8), 634-641. DOI: 10.1038/nchem.1095.

(2) Wu, D.; Chen, W.; Wang, X.; Fu, X.-Z.; Luo, J.-L. Metal-support interaction enhanced electrochemical reduction of CO2 to formate between graphene and Bi nanoparticles. *Journal of CO2 Utilization* **2020**, *37*, 353-359. DOI: doi.org/10.1016/j.jcou.2020.02.007.

(3) Hu, M.; Yao, Z.; Wang, X. Graphene-Based Nanomaterials for Catalysis. *Industrial & Engineering Chemistry Research* **2017**, *56* (13), 3477-3502. DOI: 10.1021/acs.iecr.6b05048.

(4) Fan, X.; Zhang, G.; Zhang, F. Multiple roles of graphene in heterogeneous catalysis. *Chemical Society Reviews* **2015**, *44* (10), 3023-3035. DOI: 10.1039/C5CS00094G.

(5) Zitolo, A.; Goellner, V.; Armel, V.; Sougrati, M.-T.; Mineva, T.; Stievano, L.; Fonda, E.; Jaouen, F. Identification of catalytic sites for oxygen reduction in iron- and nitrogen-doped graphene materials. *Nature Materials* **2015**, *14* (9), 937-942. DOI: 10.1038/nmat4367.

(6) Fei, H.; Dong, J.; Arellano-Jiménez, M. J.; Ye, G.; Dong Kim, N.; Samuel, E. L. G.; Peng, Z.; Zhu, Z.; Qin, F.; Bao, J.; et al. Atomic cobalt on nitrogen-doped graphene for hydrogen generation. *Nature Communications* **2015**, *6* (1), 8668. DOI: 10.1038/ncomms9668.

(7) Love, A. M.; Thomas, B.; Specht, S. E.; Hanrahan, M. P.; Venegas, J. M.; Burt, S. P.; Grant, J. T.; Cendejas, M. C.; McDermott, W. P.; Rossini, A. J.; et al. Probing the Transformation of Boron Nitride Catalysts under Oxidative Dehydrogenation Conditions. *Journal of the American Chemical Society* **2019**, *141* (1), 182-190. DOI: 10.1021/jacs.8b08165.

(8) Grant, J. T.; Carrero, C. A.; Goeltl, F.; Venegas, J.; Mueller, P.; Burt, S. P.; Specht, S. E.; McDermott, W. P.; Chieregato, A.; Hermans, I. Selective oxidative dehydrogenation of propane to propene using boron nitride catalysts. *Science* **2016**, *354* (6319), 1570-1573. DOI: 10.1126/science.aaf7885.

(9) Uosaki, K.; Elumalai, G.; Noguchi, H.; Masuda, T.; Lyalin, A.; Nakayama, A.; Taketsugu, T. Boron Nitride Nanosheet on Gold as an Electrocatalyst for Oxygen Reduction Reaction: Theoretical Suggestion and Experimental Proof. *Journal of the American Chemical Society* **2014**, *136* (18), 6542-6545. DOI: 10.1021/ja500393g.

(10) Jin, C.; Lin, F.; Suenaga, K.; Iijima, S. Fabrication of a freestanding boron nitride single layer and its defect assignments. *Phys Rev Lett* **2009**, *102* (19), 195505. DOI: 10.1103/PhysRevLett.102.195505.

(11) Zhu, W.; Gao, X.; Li, Q.; Li, H.; Chao, Y.; Li, M.; Mahurin, S. M.; Li, H.; Zhu, H.; Dai, S. Controlled Gas Exfoliation of Boron Nitride into Few-Layered Nanosheets. *Angewandte Chemie International Edition* **2016**, *55* (36), 10766-10770. DOI: 10.1002/anie.201605515.

(12) Zhu, W.; Wu, Z.; Foo, G. S.; Gao, X.; Zhou, M.; Liu, B.; Veith, G. M.; Wu, P.; Browning, K. L.; Lee, H. N.; et al. Taming interfacial electronic properties of platinum nanoparticles on vacancy-abundant boron nitride nanosheets for enhanced catalysis. *Nature Communications* **2017**, *8* (1), 15291. DOI: 10.1038/ncomms15291.

(13) Abdel Aal, S. CO catalytic oxidation on Pt-doped single wall boron nitride nanotube: first-principles investigations. *Surface Science* **2016**, *644*, 1-12. DOI: 10.1016/j.susc.2015.08.024.

(14) Mao, K.; Li, L.; Zhang, W.; Pei, Y.; Zeng, X. C.; Wu, X.; Yang, J. A theoretical study of single-atom catalysis of CO oxidation using Au embedded 2D h-BN monolayer: a CO-promoted O_2 activation. *Sci Rep* **2014**, *4*, 5441. DOI: 10.1038/srep05441.

(15) Lu, Z.; Lv, P.; Liang, Y.; Ma, D.; Zhang, Y.; Zhang, W.; Yang, X.; Yang, Z. CO oxidation catalyzed by the single Co atom embedded hexagonal boron nitride nanosheet: a DFT-D study. *Phys Chem Chem Phys* **2016**, *18* (31), 21865-21870. DOI: 10.1039/c6cp02221a.

(16) Lin, S.; Ye, X.; Johnson, R. S.; Guo, H. First-Principles Investigations of Metal (Cu, Ag, Au, Pt, Rh, Pd, Fe, Co, and Ir) Doped Hexagonal Boron Nitride Nanosheets: Stability and Catalysis of CO Oxidation. *The Journal of Physical Chemistry C* **2013**, *117* (33), 17319-17326. DOI: 10.1021/jp4055445.

(17) Huang, C.; Ye, X.; Chen, C.; Lin, S.; Xie, D. A computational investigation of CO oxidation on ruthenium-embedded hexagonal boron nitride nanosheet. *Computational and Theoretical Chemistry* **2013**, *1011*, 5-10. DOI: 10.1016/j.comptc.2013.02.004.

(18) Zhao, P.; Su, Y.; Zhang, Y.; Li, S.-J.; Chen, G. CO catalytic oxidation on iron-embedded hexagonal boron nitride sheet. *Chemical Physics Letters* **2011**, *515* (1-3), 159-162. DOI: 10.1016/j.cplett.2011.09.034.

(19) Zhao, J.; Chen, Z. Single Mo Atom Supported on Defective Boron Nitride Monolayer as an Efficient Electrocatalyst for Nitrogen Fixation: A Computational Study. *J Am Chem Soc* **2017**, *139* (36), 12480-12487. DOI: 10.1021/jacs.7b05213.

(20) Deng, C.; He, R.; Wen, D.; Shen, W.; Li, M. Theoretical study on the origin of activity for the oxygen reduction reaction of metal-doped two-dimensional boron nitride materials. *Physical Chemistry Chemical Physics* **2018**, *20* (15), 10240-10246. DOI: 10.1039/C8CP00838H.

(21) Jiménez, I.; Jankowski, A.; Terminello, L. J.; Carlisle, J. A.; Sutherland, D. G. J.; Doll, G. L.; Mantese, J. V.; Tong, W. M.; Shuh, D. K.; Himpsel, F. J. Near-edge x-ray absorption fine structure study of bonding modifications in BN thin films by ion implantation. *Applied Physics Letters* **1996**, *68* (20), 2816-2818. DOI: 10.1063/1.116334.

(22) Wang, Y.; Wang, J.; Zheng, P.; Sun, C.; Luo, J.; Xie, X. Boosting selectivity and stability on Pt/BN catalysts for propane dehydrogenation via calcination & reduction-mediated strong metal-support interaction. *Journal of Energy Chemistry* **2022**, *67*, 451-457. DOI: 10.1016/j.jechem.2021.10.008.

(23) Wang, L.; Wang, Y.; Zhang, C.-W.; Wen, J.; Weng, X.; Shi, L. A boron nitride nanosheet-supported Pt/Cu cluster as a high-efficiency catalyst for propane dehydrogenation. *Catalysis Science & Technology* **2020**, *10* (5), 1248-1255. DOI: 10.1039/C9CY02313E.

(24) Sattler, J. J.; Ruiz-Martinez, J.; Santillan-Jimenez, E.; Weckhuysen, B. M. Catalytic dehydrogenation of light alkanes on metals and metal oxides. *Chem Rev* **2014**, *114* (20), 10613-10653. DOI: 10.1021/cr5002436.

(25) Bradley, S. A.; Sinkler, W.; Blom, D. A.; Bigelow, W.; Voyles, P. M.; Allard, L. F. Behavior of Pt Atoms on Oxide Supports During Reduction Treatments at Elevated Temperatures, Characterized by Aberration Corrected Stem Imaging. *Catal. Lett.* **2012**, *142* (2), 176-182. DOI: 10.1007/s10562-011-0756-2.

(26) Chen, S.; Chang, X.; Sun, G.; Zhang, T.; Xu, Y.; Wang, Y.; Pei, C.; Gong, J. Propane dehydrogenation: catalyst development, new chemistry, and emerging technologies. *Chemical Society Reviews* **2021**, *50* (5), 3315-3354. DOI: 10.1039/D0CS00814A.

(27) Hannagan, R. T.; Giannakakis, G.; Réocreux, R.; Schumann, J.; Finzel, J.; Wang, Y.; Michaelides, A.; Deshlahra, P.; Christopher, P.; Flytzani-Stephanopoulos, M.; et al. First-principles design of a single-atom-alloy propane dehydrogenation catalyst. *Science* **2021**, *372* (6549), 1444-1447. DOI: 10.1126/science.abg8389.

(28) Qi, L.; Babucci, M.; Zhang, Y.; Lund, A.; Liu, L.; Li, J.; Chen, Y.; Hoffman, A. S.; Bare, S. R.; Han, Y.; et al. Propane Dehydrogenation Catalyzed by Isolated Pt Atoms in ≡SiOZn–OH Nests in Dealuminated Zeolite Beta. *Journal of the American Chemical Society* **2021**, *143* (50), 21364-21378. DOI: 10.1021/jacs.1c10261.

(29) Sun, X.; Han, P.; Li, B.; Zhao, Z. Tunable Catalytic Performance of Single Pt Atom on Doped Graphene in Direct Dehydrogenation of Propane by Rational Doping: A Density Functional Theory Study. *The Journal of Physical Chemistry C* **2018**, *122* (3), 1570-1576. DOI: 10.1021/acs.jpcc.7b09736.

(30) Jiang, Z.; Feng, X.; Deng, J.; He, C.; Douthwaite, M.; Yu, Y.; Liu, J.; Hao, Z.; Zhao, Z. Atomic-Scale Insights into the Low-Temperature Oxidation of Methanol over a Single-Atom Pt_1-Co_3O_4 Catalyst. *Advanced Functional Materials* **2019**, *29* (31), 1902041. DOI: 10.1002/adfm.201902041.

(31) Moses-DeBusk, M.; Yoon, M.; Allard, L. F.; Mullins, D. R.; Wu, Z.; Yang, X.; Veith, G.; Stocks, G. M.; Narula, C. K. CO Oxidation on Supported Single Pt Atoms: Experimental and ab Initio Density Functional Studies of CO Interaction with Pt Atom on θ-Al_2O_3(010) Surface. *Journal of the American Chemical Society* **2013**, *135* (34), 12634-12645. DOI: 10.1021/ja401847c.

(32) Qiao, B.; Liang, J.-X.; Wang, A.; Xu, C.-Q.; Li, J.; Zhang, T.; Liu, J. J. Ultrastable single-atom gold catalysts with strong covalent metal-support interaction (CMSI). *Nano Research* **2015**, *8* (9), 2913-2924. DOI: 10.1007/s12274-015-0796-9.

(33) Qiao, B.; Liang, J.-X.; Wang, A.; Liu, J.; Zhang, T. Single-Atom gold catalysts for low-temperature CO oxidation. *Chin. J. Catal.* **2016**, *37* (10), 1580-1586. DOI: 10.1016/S1872-2067(16)62529-9.

(34) Tao, H.; Choi, C.; Ding, L.-X.; Jiang, Z.; Han, Z.; Jia, M.; Fan, Q.; Gao, Y.; Wang, H.; Robertson, A. W.; et al. Nitrogen Fixation by Ru Single-Atom Electrocatalytic Reduction. *Chem* **2019**, *5* (1), 204-214. DOI: 10.1016/j.chempr.2018.10.007.

(35) Wang, D.; Li, Q.; Han, C.; Xing, Z.; Yang, X. Single-atom ruthenium based catalyst for enhanced hydrogen evolution. *Applied Catalysis B: Environmental* **2019**, *249*, 91-97. DOI: 10.1016/j.apcatb.2019.02.059.

(36) Lian, Z.; Si, C.; Jan, F.; Zhi, S.; Li, B. Coke Deposition on Pt-Based Catalysts in Propane Direct Dehydrogenation: Kinetics, Suppression, and Elimination. *ACS Catalysis* **2021**, *11* (15), 9279-9292. DOI: 10.1021/acscatal.1c00331.

(37) Tang, W.; Sanville, E.; Henkelman, G. A grid-based Bader analysis algorithm without lattice bias. *Journal of Physics: Condensed Matter* **2009**, *21* (8), 084204. DOI: 10.1088/0953-8984/21/8/084204.

(38) Yang, M.-L.; Zhu, Y.-A.; Fan, C.; Sui, Z.-J.; Chen, D.; Zhou, X.-G. DFT study of propane dehydrogenation on Pt catalyst: effects of step sites. *Physical Chemistry Chemical Physics* **2011**, *13* (8), 3257-3267. DOI: 10.1039/C0CP00341G.

(39) Kresse, G.; Furthmüller, J. Efficient iterative schemes for ab initio total-energy calculations using a plane-wave basis set. *Physical Review B* **1996**, *54* (16), 11169-11186. DOI: 10.1103/PhysRevB.54.11169.

(40) Perdew, J. P.; Burke, K.; Ernzerhof, M. Generalized gradient approximation made simple. *Physical review letters* **1996**, *77* (18), 3865. DOI: 10.1103/PhysRevLett.77.3865

(41) Blöchl, P. E. Projector augmented-wave method. *Physical review B* **1994**, *50* (24), 17953. DOI: 10.1103/PhysRevB.50.17953

(42) Henkelman, G; Uberuaga, B. P.; Jónsson, H. A climbing image nudged elastic band method for finding saddle points and minimum energy paths. The Journal of Chemical Physics **2000**, 113 (22), 9901-9904. DOI: 10.1063/1.1329672

(43) Maintz, S.; Deringer, V. L.; Tchougréeff, A. L.; Dronskowski, R. LOBSTER: A tool to extract chemical bonding from plane-wave based DFT. *Journal of Computational Chemistry* **2016**, *37* (11), 1030-1035. DOI: 10.1002/jcc.24300.

(44) Dronskowski, R.; Bloechl, P. E. Crystal orbital Hamilton populations (COHP): energy-resolved visualization of chemical bonding in solids based on density-functional calculations. *The Journal of Physical Chemistry* **1993**, *97* (33), 8617-8624. DOI: 10.1021/j100135a014.

Chapter 4. First-Principles investigation of the Stability and CH_4 activation capability of defective h-BN

4.1 Abstract

The hexagonal boron nitride (h-BN) material has been widely applied to the catalysis. Nevertheless, most of the research works purely focus on utilizing the h-BN as a substrate to anchor the active transition metals without probing the intrinsic activity of the h-BN defects. This work investigated the stability and activity on 8 different defects. We found that the B terminated vacancies are easier to exposed in the static condition. The N_v, BN_2 vacancy and BN_3 vacancy have intermediate C-H bond activation reaction energy. The B-N pair over BN_2 vacancy model though has lowest barrier to activate CH_4, the negative reaction energy could lead to high potential of surface poisoning. Interestingly, the unsaturated B-B pair over N_v is optimum site for C-H bond activation. Further COHP analysis imply the high C-H bond homolytic cleavage activity of B-B pair due to its weak interaction which can promote the H insertion.

4.2 Introduction:

Since the first successful synthesis by Balmain in 1842[1], the boron nitride material has been gradually broad to the attention of the public. The boron nitride materials contain three crystalline forms: the hexagonal form, cubic form and wurtzite form[2]. Among which, the hexagonal boron nitride (h-BN) is the most popular owing to its stability. In addition, the flourishing of the 2 dimensional material[3,4] also make h-BN been studied extensively in the last decades[5]. Like graphene, the h-BN is layered structure and has hybridized sp^3 B-N covalent bond which makes h-BN possess high thermal conductivity along the layer. Moreover, the h-BN has significant high thermal stability and can survive under 1000°C[6]. The high stability makes the h-BN a promising material for catalysis.

The pristine BN is inert for chemical reaction owing to its high stability. The common way to functionalize h-BN is by creating the defect sites over the BN surface[7, 8]. Prof. Jin's group fabricated the defective h-BN by energetic electron irradiation and by combining the High-resolution transmission electron microscopy (HRTEM) with the exit-wave (EW) reconstruction, and they successfully resolved the N edge defect sites[9]. In contrast to Prof. Jin's finding, Ovidiu Cretu's group observed the B terminated defect over h-BN at high temperature by the high-resolution electron energy loss spectroscopy (EELS) mapping[10]. As for the catalytic application for the h-BN, researchers using the defects site as the anchoring point for the active center for the CO oxidation reaction[11, 12]. The defect over the h-BN can selectively allow the small reactants go through[13]. In addition, a bunch of computational work were carried out to probe the reaction over Single-Atom doped

BN[14-18]. All these studies focus on the auxiliary role of BN defect for chemical reactions while seldom discuss the catalytic effect of defect itself.

Herein, this paper focuses on both N terminated vacancy and B terminated vacancy over h-BN. A bunch of h-BN defects with different size were created expressed as the mono N vacancy (N_v), mono B vacancy (B_v), BN V_c, BN_2 V_c, BN_3 V_c, NB_2 V_c, NB_3 V_c and B_3N_3 V_c, which were shown in the **Figure 4.1**. The shape of the BN, BN_2, BN_3, and B_3N_3 vacancies are learned from our previous work[19], but they are reconstructed using the 7×7 h-BN unit cell instead of 6×6 unit cell employed in our prior work. The stability of these vacancies was first analyzed, then we utilized CH_4 activation as the probe reaction to investigate the activity of different defeats. The homolytic activation and heterotic activation were both studied on different terminations followed by the deeper insight of the electronical effect.

4.3 Computational Methods

Spin polarized calculation were carried out using the Vienna Ab initio Simulation Package (VASP)[20]. For the exchange-correlation function, Perdew, Burke, and Ernzerhof (PBE)[21] were utilized with the projector augmented wave potentials[22]. For the Vander Waals correction, D3[23] method was used. A 1×1×1 k-point mesh sampling was chosen for the 7×7 h-BN lateral unit cell with a vacuum layer of ~20Å. For the single point calculation, a 5×5×1 k-point grid was adapted. The transitional states were located by the climbing-image nudged elastic band method (CI-NEB)[24]. Convergence limitation was set as 0.05 eV/Å for structural optimization and transition state search.

Normalized vacancy formation energy was calculated as the following equation:

$$\mathrm{E_f^*} = \frac{\mathrm{E_{BN\ defect}\text{-}n_{B\ defect}\mu_B\text{-}n_{N\ defect}\mu_N}}{\mathrm{n}} \qquad (4.1)$$

$$\mathrm{E_{pristine\ BN}} = \mathrm{n_{B\ pristine}\mu_B + n_{N\ pristine}\mu_N} \qquad (4.2)$$

Where the $\mathrm{E_{BN\ defect}}$ is the energy of the h-BN defect models, $\mathrm{n_B}$ and $\mathrm{n_N}$ are the atom number of B and N, respectively. n is the total number of atoms missing in the defect sites. $\mathrm{E_{pristine\ BN}}$ is the energy of pristine h-BN surface. μ_B and μ_N are the chemical potential of B and N, respectively. In the B rich scenario, the bulk phase B energy were used as the reference state ($\mu_\mathrm{B} = \mathrm{E_{bulk\ B}}$). In the N rich scenario, the gas phase N_2 energy were used as the reference state ($\mu_\mathrm{N} = \frac{1}{2}\mathrm{E_{N_2}}$). As is shown in equation (4.2), the energy pristine h-BN surface was adapted as the energy reserva.

Crystal orbital Hamiltonian populations analysis was performed by the Local orbital Basis Suite towards Electronic-Structure Reconstruction (LOBSTER 3.2.0) program[25, 26].

4.4 Results and discussion

4.4.1 Formation energy of different h-BN defects

The stability of the active site is of vital importance to the catalyst. Therefore, we first investigate the normalized formation energy based on the number of atoms removed from the surface. The formation energy was calculated based on the B rich condition, in which we took the bulk phase boron as reference and the N rich condition which we took the gas phase N_2 as the reference state. As we can see in **Figure 4.2**, the mono B/N vacancy normalized formation energies are larger than the bigger vacancy. At B rich condition, the mono N vacancy is easier to form while at N rich condition, the mono B vacancy is easier to form. Interestingly, we also observe a general trend that with the increase of the defect size (number of atoms removed), the normalized formation energy drop. Also, the formation energy of BN_2 vacancy is lower than that of NB_2 vacancy in both B rich condition and N rich condition, although they possess the same defect size. The same is true of the comparison between BN_3 and NB_3 vacancy. For both B rich and N rich scenario, the BN_3 vacancy formation energies are always lower than NB_3 vacancy. This phenomenon suggests that for medium sized vacancy, the B edge is thermodynamically favorable as both BN_2 and BN_3 has more B termination than N termination (**Figure 4.1**). As for the mono vacancy, the B_v formation energy is only slightly lower than N_v at N rich condition. This finding also imply that the B terminated vacancy has the tendency to expose.

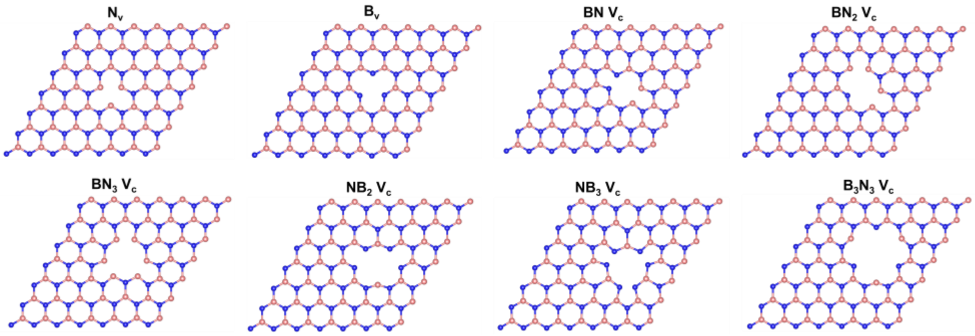

Figure 4.1 Structures of N_V, B_V, BN, BN_2, BN_3, NB_2, NB_3 and B_3N_3 vacancy.

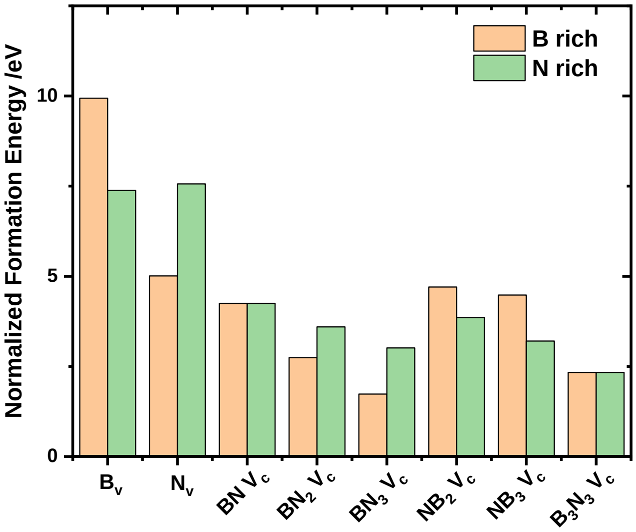

Figure 4.2 Normalized formation energy of different boron nitride defect.

4.4.2 Activity of h-BN defects

In recent years, a bunch of researchers using H binding strength as quick descriptor for fast screening the activity of catalysis surface in various chemical reaction like CH_4 activation[27], HER[28] and OER[29] reaction. Therefore, we applied the H_2 adsorption energy $(\mathrm{E_{adsorption}} = \mathrm{E_{surface+H}} - \mathrm{E_{surface}} - \frac{1}{2}\mathrm{E_{H_2}})$ as the descriptor for screening the activity of the B/N termination in the defective h-BN. As we can see in **Figure 4.3**, the pristine boron nitride is inert for H_2 adsorption. As for each defective site, the unsaturated N is always more reactive than unsaturated B. Especially for the BN_2 vacancy, the H_2 dissociation energy on the unsaturated N over BN_2 vacancy has already reached to -3.03eV, suggesting that the unsaturated N site over BN_2 vacancy is highly active.

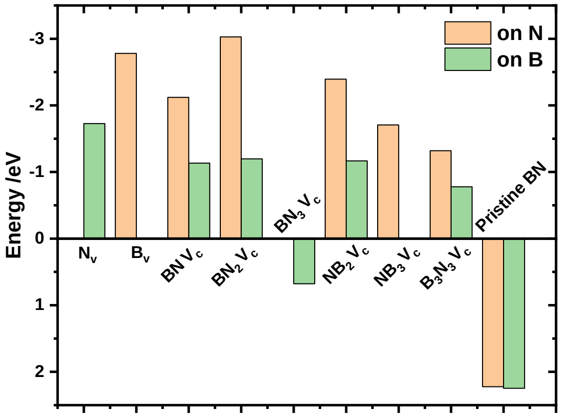

Figure 4.3 H_2 dissociation energy over defective boron nitride and pristine BN.

We further exam the CH_4 activation reaction over our BN defect models in that the CH_4 activation[30, 31] is an epidemic reaction and activating the light alkane is a critical issue in the last decades[32]. The thermodynamic screening of the first C-H bond activation were conducted first followed by the NEB searching. The intermediate level of reaction energy (ΔE) was preferred in that the positive ΔE will make the reaction unfavorable to happen while the excessively negative ΔE will make the final states too stable to proceed the following reaction. The different final states were investigated for each of our BN defect models. As is shown in **Figure 4.4**, for N_v and B_v, the final states are both CH_3 and H attached to B termination and N termination, respectively. As for BN and B_3N_3 vacancy, they both have 4 scenarios: both CH_3 and H attached to B termination; both CH_3 and H attached to B termination; CH_3 on N while H on B; CH_3 on B while H on N. As for BN_2 vacancy, it has 4 unsaturated B and 1 unsaturated N site, we hereby consider 4 scenarios:

CH_3 and H on adjacent B-B pair; CH_3 on N while H on B; CH_3 on B while H on N; CH_3 and H on B atoms which are not adjacent. For the BN_3 vacancy, owing to its pure B termination, 2 scenarios were investigated: CH_3 and H on adjacent B-B pair; CH_3 and H on B atoms which are not adjacent. For the NB_2 vacancy, three scenarios were investigated: both CH_3 and H on N; CH_3 on N while H on B; CH_3 on B while H on N. For the NB_3 vacancy, we consider both CH_3 and H on N-N pair. As for NB_3 vacancy, because of the sole N termination, 1 scenario was considered: CH_3 and H on adjacent N-N pair.

As is shown in **Figure 4.5**, we found that the unsaturated N is very active for binding CH_3 and H. It will lead to the very negative reaction energy (lower than -2eV). In contrast, the B sites are less active, the reaction energies are more positive if both CH_3 and H on B sites. In addition, CH_3 radical is more favorable on B site while H radical is more favorable on N site. By the screening of all the defects models we found the N_v and BN_2 V_c have the medium level of C-H bond activation reaction energy (between 0 eV and -2 eV). We also observe that the over BN_3 defect, although the farther B-B pair cannot stabilize the final state (CH_3 and H on surface), the adjacent B-B pair still can make the final state stable. Therefore, we also include the BN_3 defect into follow-up barrier calculation.

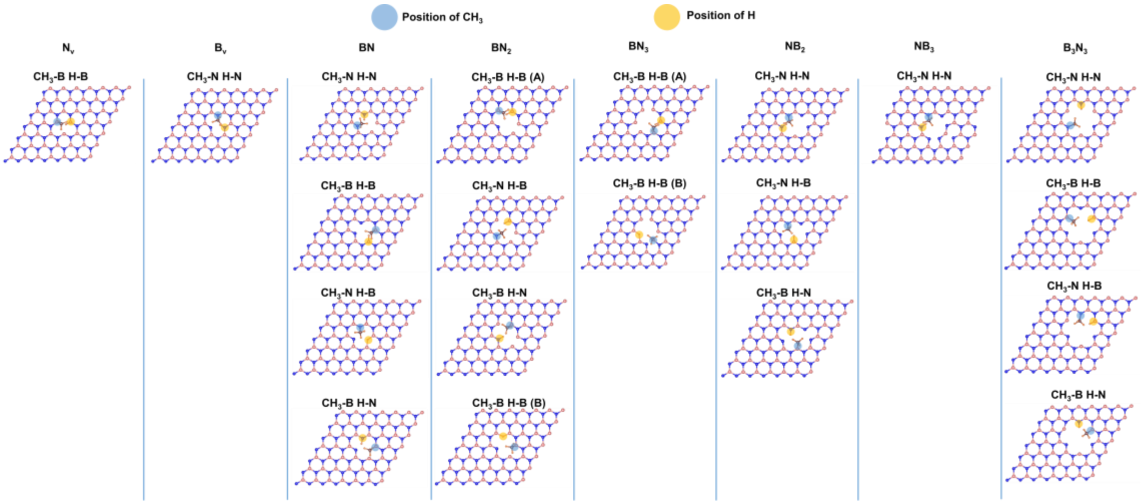

Figure 4.4 Structure of the CH_4 activation final states over different BN defects.

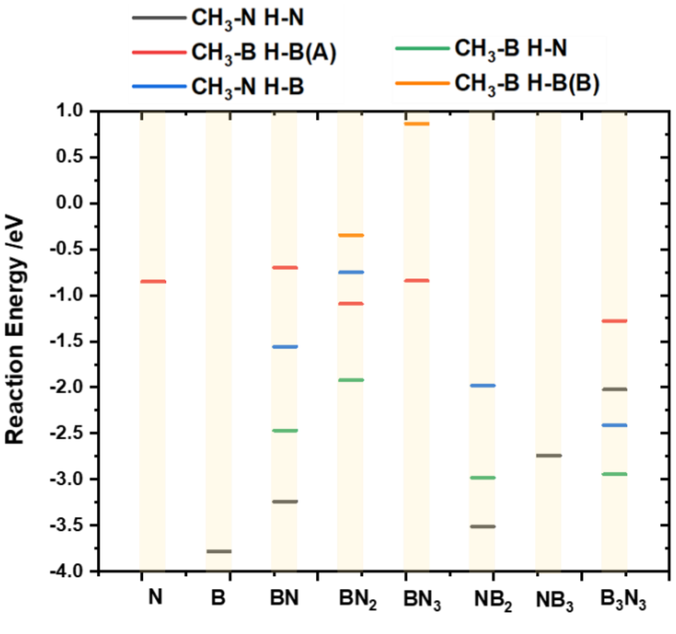

Figure 4.5 CH_4 cleavage reaction energy on N_V, B_V, BN, BN_2, BN_3, NB_2, NB_3 and B_3N_3 vacancy.

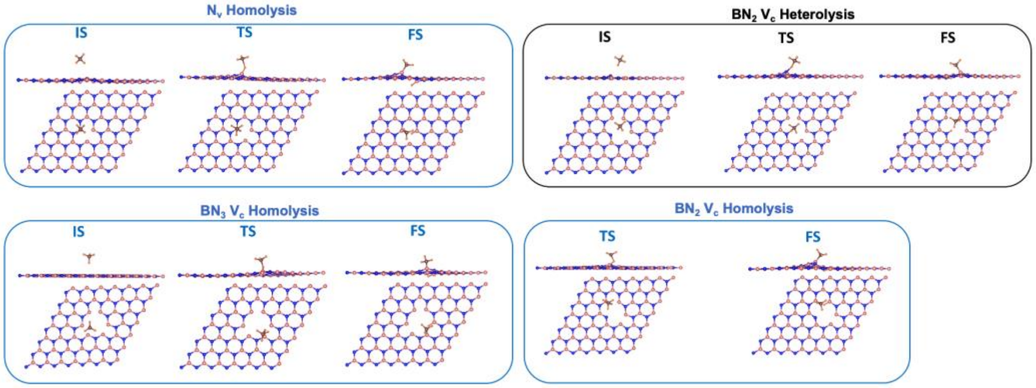

Figure 4.6 CH_4 homolytic and heterolytic cleavage structures over N_v, BN_2 V_c and BN_3 V_c.

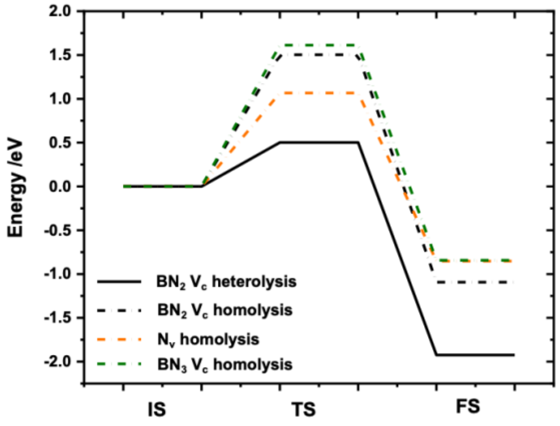

Figure 4.7 Energy profile of CH_4 cleavage over N_v, BN_2 V_c and BN_3 V_c.

As for the N_v and BN_3 V_c defect, owing their pure B termination, they can activate CH_4 by the homolytic cleavage on the adjacent B-B pair. For the BN_2 V_c, it can activate CH_4 by homolysis on its unsaturated B-B pair or activate CH_4 heterolysis on its unsaturated B-N pair. Owing to the very negative reaction energy of CH_4 heterolysis activation over BN_2 V_c, the barrier is as low as 0.5 eV, which is much lower than the homolysis over the adjacent B-B pair of the N_v, BN_2 V_c and BN_3 V_c. The high activity of the B-N pair over the BN_2 defect can be attributed to the frustrated Lewis Acid base pair which are commonly active for C-H bond activation reaction[33, 34]. However, the reaction energy is still as negative as -1.92eV, which has the tendency to poison the surface.

Interestingly, we found that the adjacent unsaturated B-B pair over N_v, BN_2 V_c and BN_3 V_c can activate C-H bond by homolytic cleavage. Moreover, the reaction energy of homolytic cleavage is between -0.5eV and -1.25eV which is an optimal value for C-H activation, especially the B-B pair over N_v, the C-H activation barrier is only 1.07eV, which make it the best active site for C-H bond cleavage.

4.4.3 Intrinsic nature of the unsaturated B-B pair

To gain a deeper insight about the unsaturated B-B pair, we investigated the structure of the transitional states of CH_4 homolytic cleavage on these vacancies. As we can see in **Figure 4.8**, the bond length of B-B pair in the transition states over N_v is larger than that of BN_2 and BN_3 vacancy. Similarly, the in the original surface, the B-B pair bond length is 2.27 Å, which is also larger than that of BN_2 and BN_3 vacancies. The farther unsaturated B-B pair make it easier for H to be inserted which account for the lower barrier on N_v.

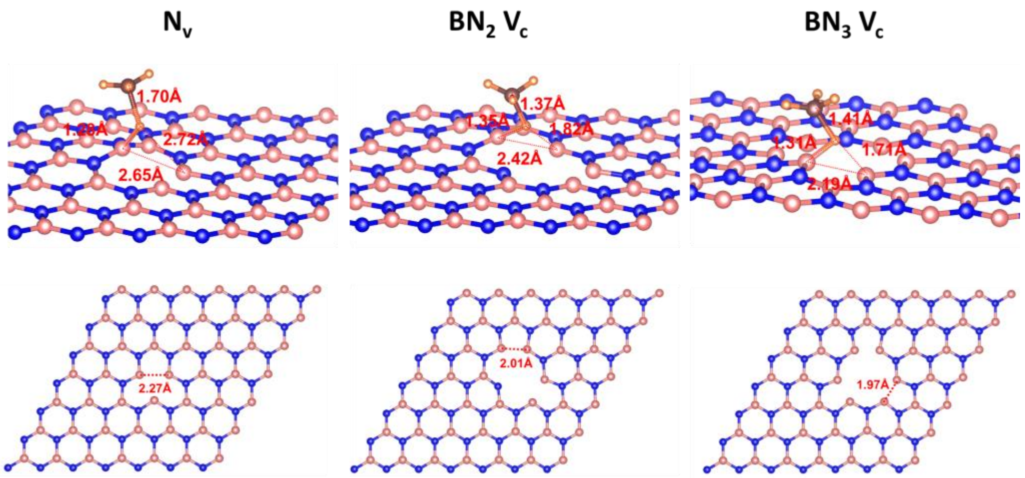

Figure 4.8 Transitional state structures of the CH_4 homolytic cleavage (up) and clean defect surface (down) over the N, BN_2 and BN_3 vacancy.

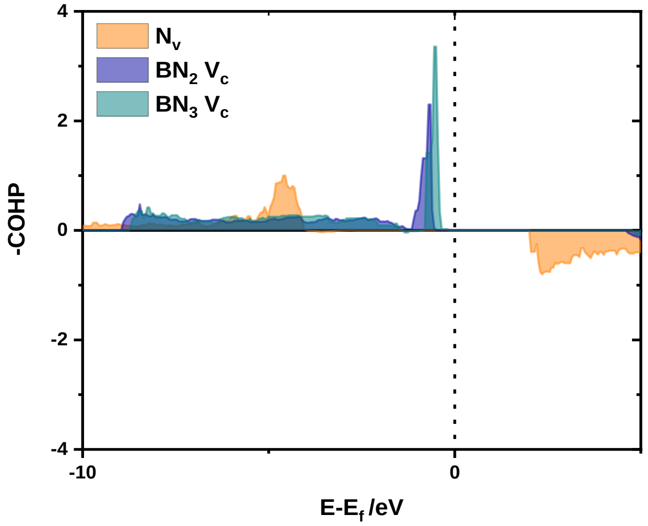

Figure 4.9 –COHP plot of the B-B pair interaction over the N, BN_2 and BN_3 vacancy.

In order to probe the electronical interaction between the B-B pair, the crystal orbital Hamilton population (COHP) analysis were carried out which can give the bonding contributions that promote the bonding interaction between atom pairs and antibonding contributions that decrease the bonding interaction. As we can see the -COHP curve in **Figure 4.9**, the for the BN_2 and BN_3 defect, there are high bonding state peak below the fermi level, below which there are electrons that can fill these bonding states which can promote the B-B interaction making it harder for H insertion. The integration of -COHP curve (ICOHP) also quantify B-B interaction over the N_v, BN_2 V_c and BN_3 V_c. The more negative ICOHP value corresponds to more stable bonding between B-B pairs. As is listed in **Table 4.1**, the ICOHP of N_v is less negative than that of BN_2 V_c and BN_3 V_c which imply that B-B pair over N_v has less electronical interaction than that of BN_2 V_c and BN_3 V_c.

Table 4.1 ICOHP value over N_v, BN_2 V_c and BN_3 V_c.

Defect	ICOHP
N_v	-1.03
BN_2 V_c	-2.30
BN_3 V_c	-2.47

4.5 Conclusion

The stability and activity of different defects on h-BN were investigated systematically. we found that the B terminated BN_2 V_c and BN_3 V_c are more stable than other equal-atom vacancies in both N rich condition and B rich condition (NB_2 V_c and NB_3 V_c). As for the monomeric vacancy, in B rich condition the N_v is more stable and in N rich condition B_v is slightly more stable than N_v. These findings imply that the B terminated defects is more stable in the static thermodynamic equilibrium condition. By investigating the CH_4 activation, we found the B-N pair though is highly active for the C-H activation, the excessively negative reaction energy will make defect surface poisoned which can impair the subsequent reaction. The unsaturated B-B pair over the N_v has the optimal reaction energy and the barrier is still low. The weak interaction between B-B pair over the N_v contribute to the H insertion which promote the homolytic cleavage of CH_4 happening over the surface.

4.6 References

(1) Balmain, W. H. Bemerkungen über die Bildung von Verbindungen des Bors und Siliciums mit Stickstoff und gewissen Metallen. *Journal für Praktische Chemie* **1842**, *27* (1), 422-430. DOI: 10.1002/prac.18420270164.

(2) Weng, Q.; Wang, X.; Wang, X.; Bando, Y.; Golberg, D. Functionalized hexagonal boron nitride nanomaterials: emerging properties and applications. *Chemical Society Reviews* **2016**, *45* (14), 3989-4012. DOI: 10.1039/C5CS00869G.

(3) Yu, S.; Wu, X.; Wang, Y.; Guo, X.; Tong, L. 2D Materials for Optical Modulation: Challenges and Opportunities. *Advanced Materials* **2017**, *29* (14), 1606128. DOI: 10.1002/adma.201606128.

(4) Luo, B.; Liu, G.; Wang, L. Recent advances in 2D materials for photocatalysis. *Nanoscale* **2016**, *8* (13), 6904-6920. DOI: 10.1039/C6NR00546B.

(5) Pakdel, A.; Bando, Y.; Golberg, D. Nano boron nitride flatland. *Chemical Society Reviews* **2014**, *43* (3), 934-959. DOI: 10.1039/C3CS60260E.

(6) Kostoglou, N.; Polychronopoulou, K.; Rebholz, C. Thermal and chemical stability of hexagonal boron nitride (h-BN) nanoplatelets. *Vacuum* **2015**, *112*, 42-45. DOI: 10.1016/j.vacuum.2014.11.009.

(7) Lin, Y.; Williams, T. V.; Cao, W.; Elsayed-Ali, H. E.; Connell, J. W. Defect Functionalization of Hexagonal Boron Nitride Nanosheets. *The Journal of Physical Chemistry C* **2010**, *114* (41), 17434-17439. DOI: 10.1021/jp105454w.

(8) Beheshtian, J.; Peyghan, A. A.; Bagheri, Z. Functionalization of BN nanosheet with N_2H_4 may be feasible in the presence of Stone–Wales defect. *Structural Chemistry* **2013**, *24* (5), 1565-1570. DOI: 10.1007/s11224-012-0189-6.

(9) Jin, C.; Lin, F.; Suenaga, K.; Iijima, S. Fabrication of a Freestanding Boron Nitride Single Layer and Its Defect Assignments. *Physical Review Letters* **2009**, *102* (19), 195505. DOI: 10.1103/PhysRevLett.102.195505.

(10) Cretu, O.; Lin, Y.-C.; Koshino, M.; Tizei, L. H. G.; Liu, Z.; Suenaga, K. Structure and Local Chemical Properties of Boron-Terminated Tetravacancies in Hexagonal Boron Nitride. *Physical Review Letters* **2015**, *114* (7), 075502. DOI: 10.1103/PhysRevLett.114.075502.

(11) Li, L.; Liu, X.; He, H.; Zhang, N.; Liu, Z.; Zhang, G. A novel two-dimensional MgO-h-BN nanomaterial supported Pd catalyst for CO oxidation reaction. *Catalysis Today* **2019**, *332*, 214-221. DOI: 10.1016/j.cattod.2018.07.025.

(12) Zhu, W.; Wu, Z.; Foo, G. S.; Gao, X.; Zhou, M.; Liu, B.; Veith, G. M.; Wu, P.; Browning, K. L.; Lee, H. N.; et al. Taming interfacial electronic properties of platinum nanoparticles on vacancy-abundant boron nitride nanosheets for enhanced catalysis. *Nature Communications* **2017**, *8* (1), 15291. DOI: 10.1038/ncomms15291.

(13) Bi, W.; Hu, Y.; Li, W.; Jiang, H.; Li, C. Construction of Nanoreactors Combining Two-Dimensional Hexagonal Boron Nitride (h-BN) Coating with Pt/Al_2O_3 Catalyst toward Efficient Catalysis for CO Oxidation. *Industrial & Engineering Chemistry Research* **2018**, *57* (40), 13353-13361. DOI: 10.1021/acs.iecr.8b02547.

(14) Mananghaya, M. R. Hydrogen saturation limit of Ti-doped BN nanotube with B-N defects: An insight from DFT calculations. *International Journal of Hydrogen Energy* **2018**, *43* (22), 10368-10375. DOI: 10.1016/j.ijhydene.2018.04.037.

(15) Zhao, J.; Chen, Z. Single Mo Atom Supported on Defective Boron Nitride Monolayer as an Efficient Electrocatalyst for Nitrogen Fixation: A Computational Study. *Journal of the American Chemical Society* **2017**, *139* (36), 12480-12487. DOI: 10.1021/jacs.7b05213.

(16) Sredojević, D. N.; Belić, M. R.; Šljivančanin, Ž. Hydrogen Evolution Reaction over Single-Atom Catalysts Based on Metal Adatoms at Defected Graphene and h-BN. *The Journal of Physical Chemistry C* **2020**, *124* (31), 16860-16867. DOI: 10.1021/acs.jpcc.0c01151.

(17) Gao, M.; Lyalin, A.; Taketsugu, T. Catalytic Activity of Au and Au_2 on the h-BN Surface: Adsorption and Activation of O_2. *The Journal of Physical Chemistry C* **2012**, *116* (16), 9054-9062. DOI: 10.1021/jp300684v.

(18) Datta, J.; Majumder, C. Stabilizing Co, Ni and Cu on the h-BN surface: Using OO bond activation to probe their performance as Single-Atom catalyst. *Catalysis Today* **2021**, *370*, 75-82. DOI: 10.1016/j.cattod.2020.10.021.

(19) Chen, H.; Xiong, C.; Moon, J.; Ivanov, A. S.; Lin, W.; Wang, T.; Fu, J.; Jiang, D.; Wu, Z.; Yang, Z.; Dai, S. Defect-Regulated Frustrated-Lewis-Pair Behavior of Boron Nitride in Ambient Pressure Hydrogen Activation. *Journal of the American Chemical Society* **2022**, *144* (24), 10688-10693. DOI: 10.1021/jacs.2c00343.

(20) Kresse, G.; Furthmüller, J. Efficient iterative schemes for ab initio total-energy calculations using a plane-wave basis set. *Physical Review B* **1996**, *54* (16), 11169-11186. DOI: 10.1103/PhysRevB.54.11169.

(21) Perdew, J. P.; Burke, K.; Ernzerhof, M. Generalized Gradient Approximation Made Simple. *Physical Review Letters* **1996**, *77* (18), 3865-3868. DOI: 10.1103/PhysRevLett.77.3865.

(22) Blöchl, P. E. Projector augmented-wave method. *Physical Review B* **1994**, *50* (24), 17953-17979. DOI: 10.1103/PhysRevB.50.17953.

(23) Grimme, S.; Antony, J.; Ehrlich, S.; Krieg, H. A consistent and accurate ab initio parametrization of density functional dispersion correction (DFT-D) for the 94 elements H-Pu. *The Journal of Chemical Physics* **2010**, *132* (15), 154104. DOI: 10.1063/1.3382344.

(24) Henkelman, G.; Uberuaga, B. P.; Jónsson, H. A climbing image nudged elastic band method for finding saddle points and minimum energy paths. *The Journal of Chemical Physics* **2000**, *113* (22), 9901-9904. DOI: 10.1063/1.1329672.

(25) Maintz, S.; Deringer, V. L.; Tchougréeff, A. L.; Dronskowski, R. LOBSTER: A tool to extract chemical bonding from plane-wave based DFT. *Journal of Computational Chemistry* **2016**, *37* (11), 1030-1035. DOI: 10.1002/jcc.24300.

(26) Dronskowski, R.; Bloechl, P. E. Crystal orbital Hamilton populations (COHP): energy-resolved visualization of chemical bonding in solids based on density-functional calculations. *The Journal of Physical Chemistry* **1993**, *97* (33), 8617-8624. DOI: 10.1021/j100135a014.

(27) Latimer, A. A.; Kulkarni, A. R.; Aljama, H.; Montoya, J. H.; Yoo, J. S.; Tsai, C.; Abild-Pedersen, F.; Studt, F.; Nørskov, J. K. Understanding trends in C-H bond activation in heterogeneous catalysis. *Nature Materials* **2017**, *16* (2), 225-229. DOI: 10.1038/nmat4760.

(28) Dubouis, N.; Grimaud, A. The hydrogen evolution reaction: from material to interfacial descriptors. *Chemical Science* **2019**, *10* (40), 9165-9181. DOI: 10.1039/C9SC03831K.

(29) Zheng, J.; Nash, J.; Xu, B.; Yan, Y. Perspective—Towards Establishing Apparent Hydrogen Binding Energy as the Descriptor for Hydrogen Oxidation/Evolution Reactions. *Journal of The Electrochemical Society* **2018**, *165* (2), H27-H29. DOI: 10.1149/2.0881802jes.

(30) Taifan, W.; Baltrusaitis, J. CH_4 conversion to value added products: Potential, limitations and extensions of a single step heterogeneous catalysis. *Applied Catalysis B: Environmental* **2016**, *198*, 525-547. DOI: 10.1016/j.apcatb.2016.05.081.

(31) Saillard, J. Y.; Hoffmann, R. Carbon-hydrogen and hydrogen-hydrogen activation in transition metal complexes and on surfaces. *Journal of the American Chemical Society* **1984**, *106* (7), 2006-2026. DOI: 10.1021/ja00319a020.

(32) Sattler, J. J.; Ruiz-Martinez, J.; Santillan-Jimenez, E.; Weckhuysen, B. M. Catalytic dehydrogenation of light alkanes on metals and metal oxides. *Chemical Reviews* **2014**, *114* (20), 10613-10653. DOI: 10.1021/cr5002436.

(33) Wischert, R.; Copéret, C.; Delbecq, F.; Sautet, P. Optimal Water Coverage on Alumina: A Key to Generate Lewis Acid–Base Pairs that are Reactive Towards the C-H Bond Activation of Methane. *Angewandte Chemie International Edition* **2011**, *50* (14), 3202-3205. DOI: 10.1002/anie.201006794.

(34) Liu, L. L.; Stephan, D. W. Radicals derived from Lewis acid/base pairs. *Chemical Society Reviews* **2019**, *48* (13), 3454-3463. DOI: 10.1039/C8CS00940F.

Chapter 5. First-Principles study of the methane selective oxidation to acetic acid over Single-Atom Rh pMOF catalyst

5.1 Abstract

Rh SACs have been reported as promising catalysts for direct CH_4 oxidation to CH_3COOH, which is a substitutive process for CH_4 indirect transfer via syngas. This CH_4 direct oxidation significantly reduces pollution and simplifies the pathway of chemical transfer. However, the mechanism of the CH_4 direct oxidation over Rh SACs is unknown. We utilized the gaussian calculations to illuminate the working mechanism of Rh Single-Atom dispersed on porphyrin-based MOF catalyst and unveil the effect of light on the selectivity of the catalyst that the dark condition favors the CH_3OH production while the light condition facilitates the CH_3COOH production. By investigating the two different models with different Rh coordination environments: (1) Single-Atom Rh anchored in the porphyrin plane; (2) Single-Atom Rh out-of-plane geometry, we found that the out-of-plane model has lower barrier facilitating the CH_3COOH formation while the in-plane model has lower barrier facilitating the CH_3OH formation.

5.2 Introduction

Owing to the shale gas revolution, driven by the technological breakthrough of the hydraulic fracturing[1] and horizontal drilling[2] in recent years , the production of shale gas skyrocketed, making the United States one of the world's largest natural gas producers. The effective transfer and utilization of the overproduced nature gas remains a hot topic and a significant challenge in the energy industry. Methane, as one of the major components of natural gas, has been widely used as a raw material for the production of value-added chemicals such as methanol[3] and acetic acid[4]. However, due to the high C-H bond energy in methane, effectively activating C-H bond in methane is a world-wide challenge[5]. To efficiently activate methane, initially, researchers utilized the noble metal catalysts, such as Rh, Ru, Pt and Pd, to transfer the methane in the oxidation condition to the synthesis gas[6]. Later scientists began to explore the possibility of non-noble materials for the methane activation. Ni based catalyst has been proven to be highly active for methane activation[7]. However, the large bulk Ni nanoparticles would lead to the coking and deactivation of the catalysts. To tackle this issue, Dr. Sheng Dai collaborated with Dr. Huiyuan Zhu leveraged the spatial confinement strategy to control the size of the Ni nanoparticles below 5nm, they found that their prepared catalyst has long-term stability in 700 °C reaction atmosphere[8]. Upon the characterization, they concluded that their catalyst possesses excellent sintering and coking resistance[8].

In terms of the acetic acid formation by methane transformation, the current industrial method utilized the indirect strategy to produce CH_3COOH[9]: (1) steam reforming of methane to produce syngas (CO and H_2 gas mixtures); (2) carbonylation reaction from syngas to acetic acid. The conventional process is highly energy-intensive and inefficient with its long chemical process pathway. Thus, it's of vital importance to develop the substitutive method for the current syngas route. Previous literatures[10-12] found that the Single-Atom dispersed Ru catalysts could well catalyze the selective oxidation of CH_4

towards CH_3COOH. Nevertheless, due to the concerns that the aggregation would happen in the reaction atmosphere, which reduces the catalytic capability of Rh, the loading of the Rh is low and this limitation confines the overall conversion rates and yield of the catalysts. The current milestone performance of CH_4 selective oxidation to CH_3COOH by Single-Atom Rh catalysts was achieved by Dr. Maria Flytzani-Stephanopoulos's group with 13000 μmol g_{cat}^{-1} and around 60% CH_3COOH selectivity[10]. However, the interactions between the zeolites and the Rh is still weak and researchers cannot further increase the loading of the Rh on zeolites. Recently, the porphyrin materials has been widely used to anchor Single-Atom catalysts[13]. Dr. Hai-Long Jiang's group utilized the N doped porphyrinic MOF to disperse Single-Atom Fe[14]. Their Fe loading can reach to 1.76 wt%, and the excellent ORR performance was achieved thanks to the highly concentrated Single-Atom Fe active sites.

To tackle this issue, our collaborators Dr. Haoyi Li and Dr. Dunwei Wang successfully synthesized the high Rh loading catalysts with the metal organic framework (MOF) support by making use of highly concentrated porphyrin groups over the linkers. By leveraging the Gaussian simulations, we built up the cluster model of Single-Atom Rh dispersed on the porphyrin skeleton. Also, we illuminated the reaction mechanism of the CH_3COOH formation and the phenomenon of CH_3COOH selectivity switch owing to the light excitations.

5.3 Computational Methods

The ground state calculation based on DFT was conducted by GAUSSIAN16 package [15]. The default Berny algorithm by GEDIIS was used for local optimizations and transition states search [16]. The hybrid PBE0 function [17] was employed with 6-31G(d) [18] basis set for the elements of C, H, N, O, and LANL2DZ basis set and effective potentials for the Rh atom [19, 20]. The frequency scaling factor was chosen as 0.95 according to the previous work [21]. The simulated DRIFTS spectrum was achieved by Multiwfn program [22]. To simplify the calculation process, the model of Rh-tetraphenylporphyrin (Rh_1/TPP) complex was deployed to stand for Rh_1/pMOF. The temperature used for the calculations of the catalytic cycles was 0 K. No solvation effect by H_2O was considered, either.

5.4 Experimental Findings

Experimentally, our collaborators utilized the wet impregnation method to load Rh onto the porphyrin-based MOF (pMOF)[23]. Also, by using the extended X-ray absorption fine structure (EXAFS) characterization, they found that isolated Rh atoms are well-dispersed on the pMOF[23]. Also, from the catalytic performance results, we found that the catalyst is sensitive to light. In the reaction condition without light, the catalyst will favor the formation of CH_3OH while in the light condition, the CH_3COOH formation will be favored.

5.5 Results & Discussion

While the high performance of Rh_1/pMOF in the CH_3COOH synthesis by direct CH_4 oxidation may be expected owing to the high density of atomically dispersed Rh sites, the switch of product selectivity between CH_3COOH and CH_3OH with and without light, respectively, is new and intriguing. To gain insights into the possible origin of this switch, we turned to density functional theory (DFT) calculations. In doing so, we examined two reported coordination environments of Rh in a porphyrin binding site (**Figure 5.1**)[24],namely, the in-plane geometry and the out-of-plane one. Our calculations suggest that the in-plane Rh_1 site favors CH_3OH formation, whereas CH_3COOH production is favored by the out-of-plane Rh_1 site. As shown in **Figures 5.3 and 5.5**, the difficulty of CH_3COOH formation at the in-plane Rh_1 site lies in the high activation energy of CO coadsorption next to CH_3 on Rh_1 in preparation for the insertion step (TS10 in **Figure 5.2a**). For the out-of-plane Rh_1 site, the key differentiating step between CH_3OH formation and that of CH_3COOH is methyl migration, as shown in **Figure 5.2b** (see also **Figures 5.4 and 5.6**), where CH_3COOH production is favored. It is further noted that the DFT calculations were conducted with simplifications, and the activation barriers reported here should be treated qualitatively for the purpose of comparing different product selectivities (see the **Supporting Discussion**). While additional research will be required to fully understand the process, we hypothesize that light-induced ligand-to-metal charge transfer (LMCT) is the key factor that leads to the changes of the Rh coordination environment under reaction conditions.[25-27] LMCT was indeed observed by transient ultraviolet–visible (UV–vis) absorption spectroscopy[23]. Moreover, the selectivity is dependent on light intensity in a monotonic fashion, suggesting that the portion of active sites that adopts the out-of-plane coordination environment is proportional to light intensities.

5.5.1 Supporting Discussion

The best way to understand the energy diagram as shown in **Figure 5.4** is to focus on the bifurcating points. For this purpose, we replot the energy diagram in two separate graphs as separated by the release of the first and the second target molecules. From c0 to c6, the steps describe the activation of the first CH_4 molecule. These steps are shared by both reaction pathways. Indeed, the activation of C-H in CH_4 is a difficult step; this is manifested by the high activation barrier that leads to the formation of TS14 (1.62 eV); it is also corroborated by the experimental observation that the apparent reaction order relative to CH_4 partial pressure is 2. From c6, the reaction could proceed to release either CH_3OH (through TS20, 0.89 eV) or CH_3COOH (through TS15 (0.58 eV) & TS16 (0.08 eV)), which are the energy barrier of the CH_3-O and CH_3-CO coupling, respectively. It can be readily concluded that the formation of CH_3OH is more difficult than that of CH_3COOH on the out-of-plane Rh_1 sites.

Next, we arrive at the next bifurcating point, which is c14. The pathway that leads to the release of CH_3OH involves another transition state (TS21) featuring a high energy (0.84 eV), whereas the pathway that produces CH_3COOH (TS18, 0.73 eV) is favored. Taken as a whole, while the overall reaction appears to be limited by methane activation, the selectivity of the products is controlled by the key steps at the bifurcating points, where the mechanisms favor CH_3COOH formation for the out-of-plane coordination.

Lastly, we note that simplifications have been taken in the computational calculations. For instance, the calculations of energy barriers in the two catalytic cycles (**Figures 5.3 and 5.4**) were performed at 0 K (-273.15 °C), whereas the experiments were conducted between 130 °C and 160 °C. Moreover, we employed a molecular model of Rh-tetraphenylporphyrin (Rh_1/TPP) complex but not the solid-state MOF structure (Rh_1/pMOF) for the calculations. Moreover, our calculations did not consider solvent effects, whereas the experiments were conducted in aqueous solution. These simplifications were made to make the problem more tractable; they serve the purpose to qualitatively understand how the change of coordination configuration could alter the relative energetics for different reaction pathways. These results set the stage for more refined calculations by future research. Nevertheless, these values should not be directly compared with the experimentally obtained activation barriers[23].

5.6 Conclusion

In conclusion, we adapted two Rh Single-Atoms doped pMOF models with different Rh coordinates to explain the selectivity switch phenomenon due to the existence of the lights. We found that the Rh in-plane model is more favorable for the production of the CH_3OH while the Rh out-plane model is more favorable for the CH_3COOH production.

5.7 References

(1) Osiptsov, A. A. Fluid Mechanics of Hydraulic Fracturing: a Review. *Journal of Petroleum Science and Engineering* **2017**, *156*, 513-535. DOI: 10.1016/j.petrol.2017.05.019.

(2) Ishak, I. B.; Steele, R. P.; Macaulay, R. C.; Stephenson, P. M.; Al Mantheri, S. M. Review of Horizontal Drilling. *In Middle East Oil Show*, 1995; SPE-29812-MS, Vol. All Days. DOI: 10.2118/29812-ms.

(3) Tomkins, P.; Ranocchiari, M.; van Bokhoven, J. A. Direct Conversion of Methane to Methanol under Mild Conditions over Cu-Zeolites and beyond. *Accounts of Chemical Research* **2017**, *50* (2), 418-425. DOI: 10.1021/acs.accounts.6b00534.

(4) Rabie, A. M.; Betiha, M. A.; Park, S.-E. Direct synthesis of acetic acid by simultaneous co-activation of methane and CO_2 over Cu-exchanged ZSM-5 catalysts. *Applied Catalysis B: Environmental* **2017**, *215*, 50-59. DOI: 10.1016/j.apcatb.2017.05.053.

(5) Shang, R.; Ilies, L.; Nakamura, E. Iron-Catalyzed C–H Bond Activation. *Chemical Reviews* **2017**, *117* (13), 9086-9139. DOI: 10.1021/acs.chemrev.6b00772.

(6) York, A. P. E.; Xiao, T.; Green, M. L. H. Brief Overview of the Partial Oxidation of Methane to Synthesis Gas. *Topics in Catalysis* **2003**, *22* (3), 345-358. DOI: 10.1023/A:1023552709642.

(7) Liu, Z.; Grinter, D. C.; Lustemberg, P. G.; Nguyen-Phan, T. D.; Zhou, Y.; Luo, S.; Waluyo, I.; Crumlin, E. J.; Stacchiola, D. J.; Zhou, J. Dry reforming of methane on a highly-active Ni-CeO_2 catalyst: effects of metal-support interactions on C−H bond breaking. *Angewandte Chemie International Edition* **2016**, *55* (26), 7455-7459. DOI: 10.1002/anie.201602489.

(8) Peng, H.; Zhang, X.; Han, X.; You, X.; Lin, S.; Chen, H.; Liu, W.; Wang, X.; Zhang, N.; Wang, Z.; et al. Catalysts in Coronas: A Surface Spatial Confinement Strategy for High-Performance Catalysts in Methane Dry Reforming. *ACS Catalysis* **2019**, *9* (10), 9072-9080. DOI: 10.1021/acscatal.9b00968.

(9) Meng, X.; Cui, X.; Rajan, N. P.; Yu, L.; Deng, D.; Bao, X. Direct Methane Conversion under Mild Condition by Thermo-, Electro-, or Photocatalysis. *Chem* **2019**, *5* (9), 2296-2325. DOI: 10.1016/j.chempr.2019.05.008.

(10) Shan, J.; Li, M.; Allard, L. F.; Lee, S.; Flytzani-Stephanopoulos, M. Mild oxidation of methane to methanol or acetic acid on supported isolated rhodium catalysts. *Nature* **2017**, *551* (7682), 605-608. DOI: 10.1038/nature24640.

(11) Tang, Y.; Li, Y.; Fung, V.; Jiang, D.-e.; Huang, W.; Zhang, S.; Iwasawa, Y.; Sakata, T.; Nguyen, L.; Zhang, X.; et al. Single rhodium atoms anchored in micropores for efficient transformation of methane under mild conditions. *Nature Communications* **2018**, *9* (1), 1231. DOI: 10.1038/s41467-018-03235-7.

(12) Kolesnichenko, N. V.; Batova, T. I.; Stashenko, A. N.; Obukhova, T. K.; Khramov, E. V.; Sadovnikov, A. A.; Zavelev, D. E. The role of the spatial arrangement of single rhodium sites on ZSM-5 in the oxidative methane carbonylation to acetic acid. *Microporous and Mesoporous Materials* **2022**, *344*, 112239. DOI: 10.1016/j.micromeso.2022.112239.

(13) Yang, H.; Shi, R.; Shang, L.; Zhang, T. Recent Advancements of Porphyrin-Like Single-Atom Catalysts: Synthesis and Applications. *Small Structures* **2021**, *2* (6), 2100007. DOI: 10.1002/sstr.202100007.

(14) Jiao, L.; Wan, G.; Zhang, R.; Zhou, H.; Yu, S. H.; Jiang, H. L. From metal–organic frameworks to single-atom Fe implanted N-doped porous carbons: efficient oxygen reduction in both alkaline and acidic media. *Angewandte Chemie* **2018**, *130* (28), 8661-8665. DOI: 10.1002/ange.201803262.

(15) Frisch, M.; Trucks, G.; Schlegel, H.; Scuseria, G.; Robb, M.; Cheeseman, J.; Scalmani, G.; Barone, V.; Petersson, G.; Nakatsuji, H. Gaussian 16 Rev. C. 01, Wallingford, CT. 2016.

(16) Li, X.; Frisch, M. J. Energy-represented direct inversion in the iterative subspace within a hybrid geometry optimization method. *Journal of Chemical Theory and Computation* **2006**, *2* (3), 835-839. DOI: 10.1021/ct050275a.

(17) Vetere, V.; Adamo, C.; Maldivi, P. Performance of the `parameter free' PBE0 functional for the modeling of molecular properties of heavy metals. *Chemical Physics Letters* **2000**, *325* (1), 99-105. DOI: 10.1016/S0009-2614(00)00657-6.

(18) Kristyán, S.; Ruzsinszky, A.; Csonka, G. I. Accurate thermochemistry from corrected Hartree–Fock results: rapid estimation of nearly experimental quality total energy using the small 6-31G(d) basis set. *Theoretical Chemistry Accounts* **2001**, *106* (5), 319-328. DOI: 10.1007/s002140100282.

(19) Chiodo, S.; Russo, N.; Sicilia, E. LANL2DZ basis sets recontracted in the framework of density functional theory. *Journal of Chemical Physics* **2006**, *125* (10), 104107. DOI: 10.1063/1.2345197.

(20) Hay, P. J.; Wadt, W. R. Ab initio effective core potentials for molecular calculations. Potentials for K to Au including the outermost core orbitals. *Journal of Chemical Physics* **1985**, *82* (1), 299-310. DOI: 10.1063/1.448975.

(21) Tantirungrotechai, Y.; Phanasant, K.; Roddecha, S.; Surawatanawong, P.; Sutthikhum, V.; Limtrakul, J. Scaling factors for vibrational frequencies and zero-point vibrational energies of some recently developed exchange-correlation functionals. *Journal of Molecular Structure: THEOCHEM* **2006**, *760* (1), 189-192. DOI: 10.1016/j.theochem.2005.12.007.

(22) Lu, T.; Chen, F. Multiwfn: a multifunctional wavefunction analyzer. *Journal of Computational Chemistry* **2012**, *33* (5), 580-592. DOI: 10.1002/jcc.22885.

(23) Li, H.; Xiong, C.; Fei, M.; Ma, L.; Zhang, H.; Yan, X.; Tieu, P.; Yuan, Y.; Zhang, Y.; Nyakuchena, J.; et al. Selective Formation of Acetic Acid and Methanol by Direct Methane Oxidation Using Rhodium Single-Atom Catalysts. *Journal of the American Chemical Society* **2023**, *145* (20), 11415-11419. DOI: 10.1021/jacs.3c03113.

(24) Thompson, S. J.; Brennan, M. R.; Lee, S. Y.; Dong, G. Synthesis and applications of rhodium porphyrin complexes. *Chemical Society Reviews* **2018**, *47* (3), 929-981. DOI: 10.1039/C7CS00582B.

(25) Leng, F.; Liu, H.; Ding, M.; Lin, Q.-P.; Jiang, H.-L. Boosting Photocatalytic Hydrogen Production of Porphyrinic MOFs: The Metal Location in Metalloporphyrin Matters. *ACS Catalysis* **2018**, *8* (5), 4583-4590. DOI: 10.1021/acscatal.8b00764.

(26) Kim, D.; Whang, D. R.; Park, S. Y. Self-Healing of Molecular Catalyst and Photosensitizer on Metal–Organic Framework: Robust Molecular System for Photocatalytic H2 Evolution from Water. *Journal of the American Chemical Society* **2016**, *138* (28), 8698-8701. DOI: 10.1021/jacs.6b04552.

(27) Horváth, O.; Valicsek, Z.; Harrach, G.; Lendvay, G.; Fodor, M. A. Spectroscopic and photochemical properties of water-soluble metalloporphyrins of distorted structure. *Coordination Chemistry Reviews* **2012**, *256* (15), 1531-1545. DOI: 10.1016/j.ccr.2012.02.011.

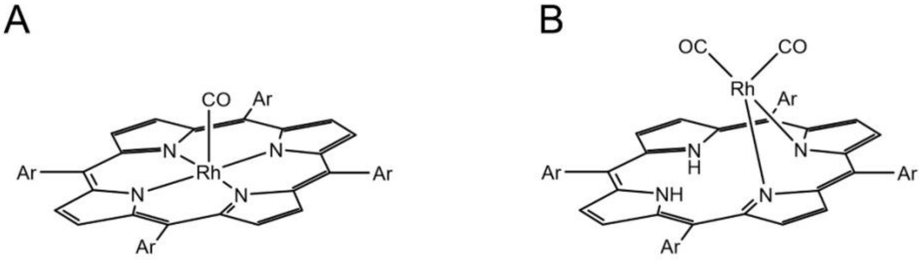

Figure 5.1 The structures of (A) in-plane and (B) out-of-plane Rh_1 sites enter the catalytic cycles based on the Rh_1/TPP model for DFT calculations.

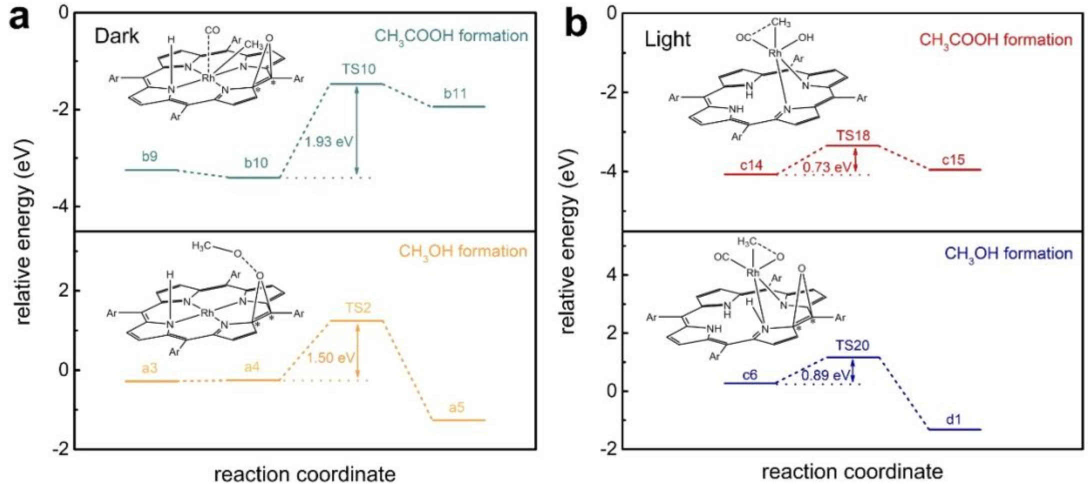

Figure 5.2 (a) Pre-insertion step of CO for the formation of CH_3COOH (upper) and O_2 dissociation step for the formation of CH_3OH (bottom) at the in-plane Rh_1 site. (b) Methyl migration to CO for the formation of CH_3COOH (upper) and methyl migration to O for the formation of CH_3OH (bottom) at the out-of-plane Rh_1 site. The steps in a and b are referred to those in the overall catalytic cycles as shown in **Figure 5.5** and **Figure 5.6**, respectively. Inset structures in a and b show the corresponding transition states.

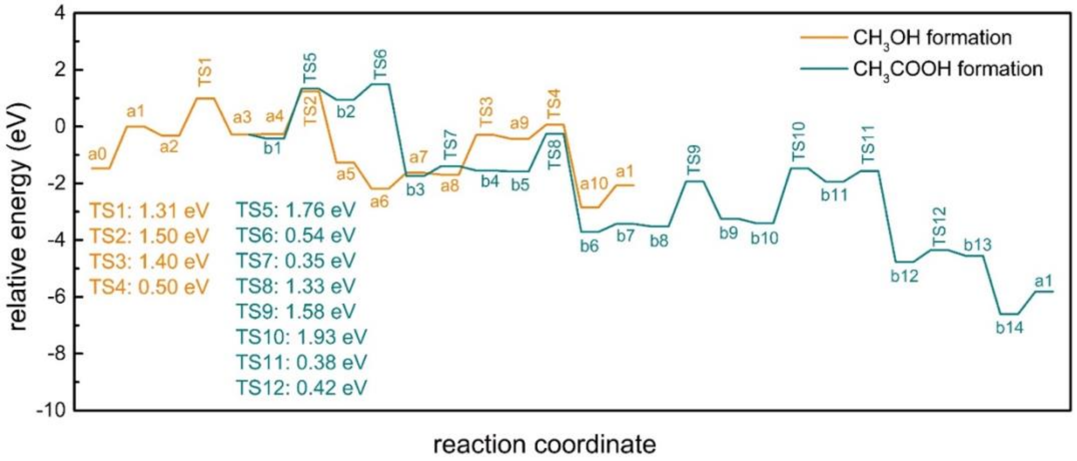

Figure 5.3 Energy plots of intermediates and transition states for the catalytic cycles over in-plane Rh$_1$ sites based on DFT calculations. Transition states are denoted as "TS".

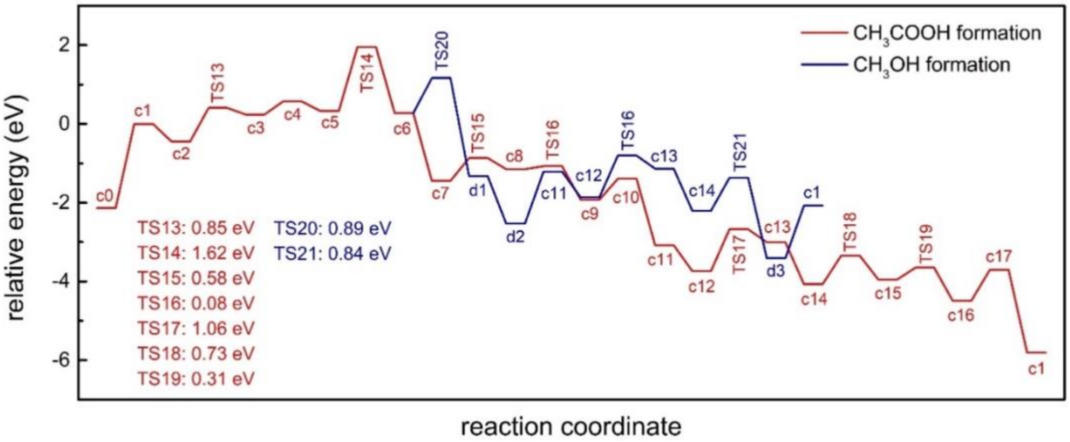

Figure 5.4 Energy plots of intermediates and transition states for the catalytic cycles over out-of-plane Rh$_1$ sites based on DFT calculations. Transition states are denoted as "TS".

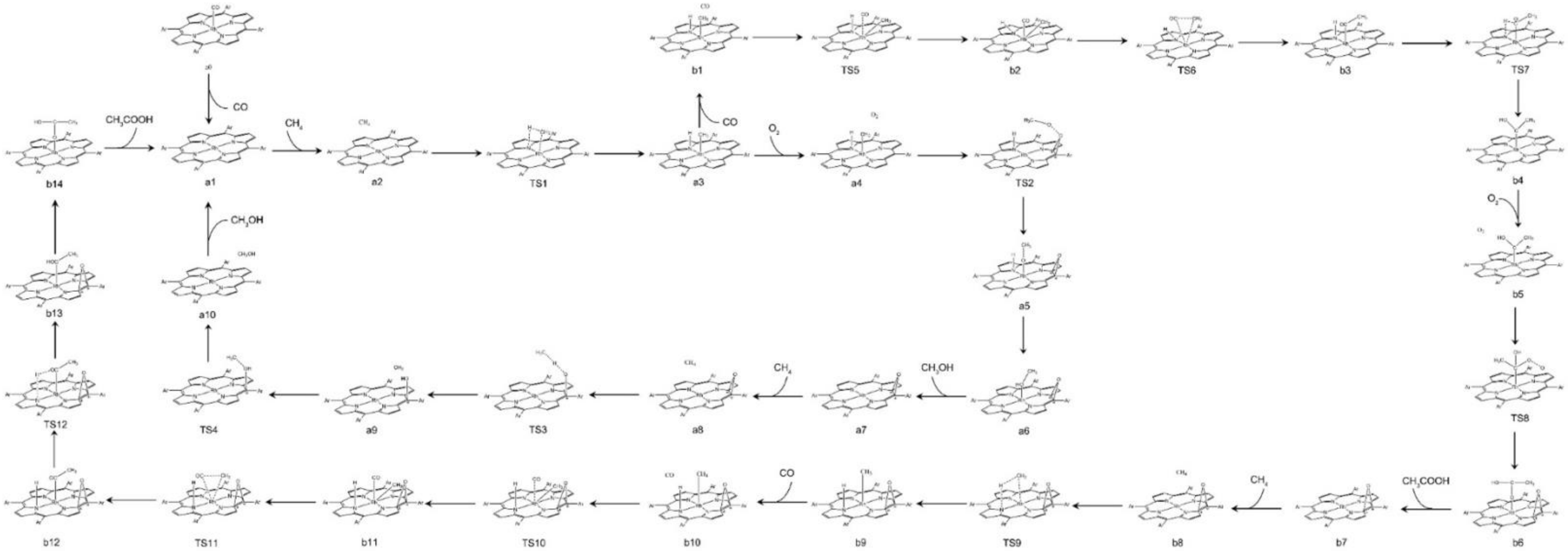

Figure 5.5 Catalytic cycles of selective CH_4 oxidation toward CH_3COOH and CH_3OH in dark with in-plane Rh_1 sites. Schematic reaction pathways for the formation of CH_3COOH (**outer circle**) and CH_3OH (**inner circle**) from CH_4, CO, and O_2 on the Rh_1/TPP model. The overall reactions to form CH_3COOH and CH_3OH are illustrated as $2CH_4+2CO+O_2\rightarrow2CH_3COOH$ and $2CH_4+O_2\rightarrow2CH_3OH$, respectively.

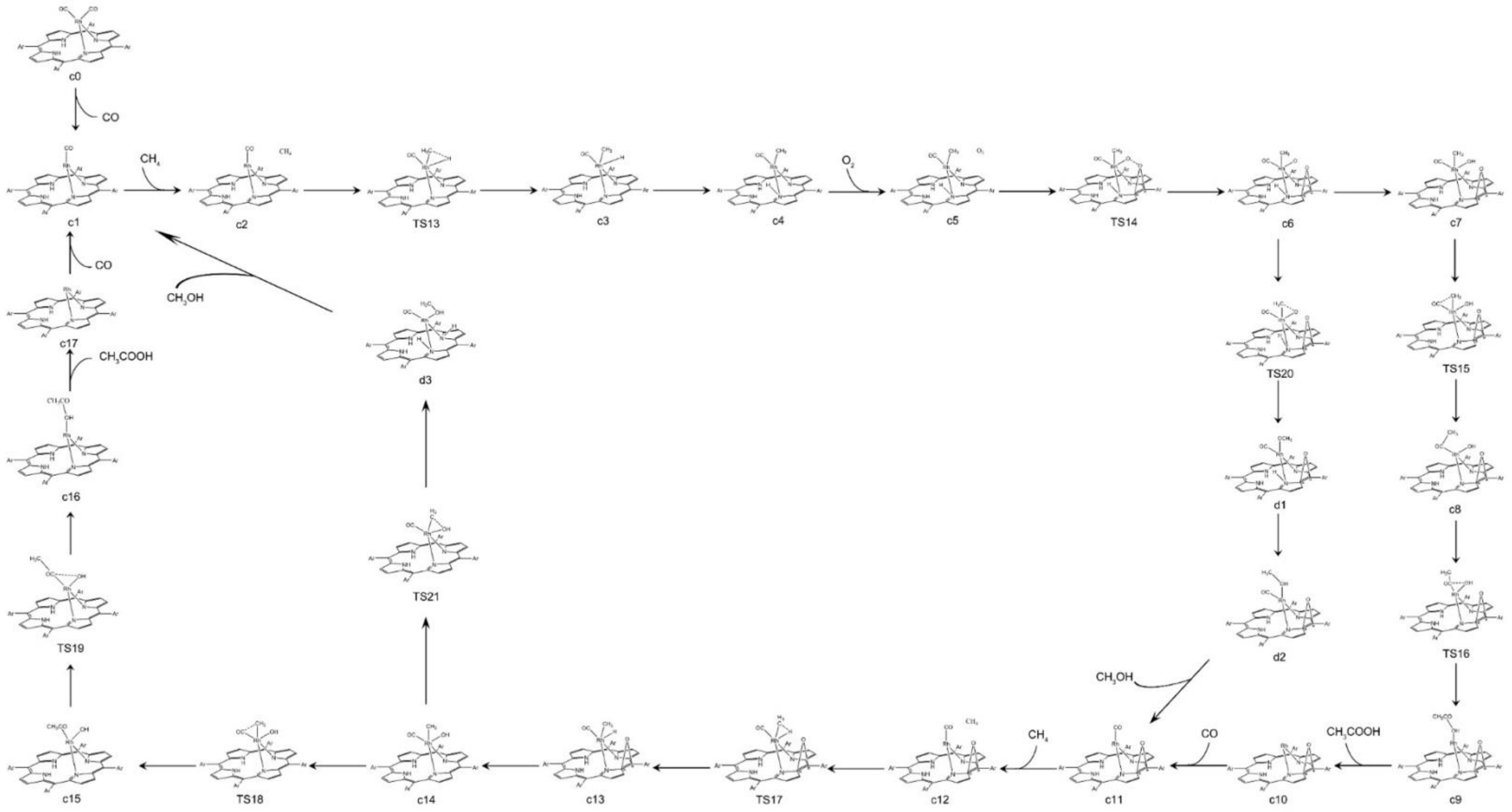

Figure 5.6 Catalytic cycles of selective CH_4 oxidation toward CH_3COOH and CH_3OH in light with out-of-plane Rh_1 sites. Schematic reaction pathways for the formation of CH_3COOH (**outer circle**) and CH_3OH (**inner circle**) from CH_4, CO, and O_2 on the Rh_1/TPP model. The overall reactions to form CH_3COOH and CH_3OH are illustrated as $2CH_4+2CO+O_2 \rightarrow 2CH_3COOH$ and $2CH_4+O_2 \rightarrow 2CH_3OH$, respectively.

Chapter 6. Conclusions and Future Outlook

6.1 Conclusions

In this Ph.D. thesis, we combined the density functional theory with ab *initio* molecular dynamic (AIMD) simulations to investigate the activity, stability, and selectivity of the Single-Atom catalysts. We aim at building up the structural-performance relationships of the Single-Atom catalysts (SACs) to assist the readers to better understand the intrinsic nature of the SACs. The focuses of this thesis are such two aspects: (1) Investigating the geometric and electronic properties of the catalysts and further probing the reaction mechanism based on this information; (2) Conducting the screenings of the catalysts and design for better SACs with excellent catalytic capability.

In chapter 3, we investigate the activity, stability and selectivity of the Single-Atom Ru, Au, Pt over 2-dimensional hexagonal boron nitride material (h-BN). From the anchoring energy calculations and the AIMD simulations, we found that the SAC Au is not stable on the defect sites of h-BN. From the energy calculations of propane dehydrogenation reaction, we concluded that the Single-Atom Pt at B vacancy in h-BN and Single-Atom Ru at N vacancy in h-BN are promising catalysts.

In chapter 4, we mainly focused on the defect site of the 2-dimensional h-BN, we screened a set of defects sites with different sizes. We found that the normalized formation energy of the defect site decreases with the increase of the defect size. In terms of the catalytic activity, the BN_2 vacancy, BN_3 vacancy, and the N vacancy possess reasonable CH_4 activation reaction energy. The BN_2 vacancy could activate the CH_4 with unsaturated B-N pair while the N and BN_3 vacancies could activate the CH_4 with unsaturated B-B pair. Upon COHP analysis, we found that the interaction between the B-B pair in the N vacancy is weak, which makes it easier for CH_4 to insert.

In chapter 5, we leveraged the Gaussian calculations to investigate the methane selective oxidation over Single-Atom Rh on porphyrin-bases MOF (pMOF) catalyst. Experimentally, our collaborators found that light is the pivot factor for the selectivity switch phenomenon. In light conditions, the Single-Atom Rh pMOF catalyst favors the formation of CH_3COOH while in dark conditions, the catalyst favors the formation of CH_3OH. By using the DFT calculations, we examined two models with different Rh coordinates (i.e., Rh in-plane model and Rh out-of-plane model), We found that the Rh in-plane model favors the formation of CH_3OH while the Rh out-plane model favors the formation of CH_3COOH owing to the lower activation barrier.

6.2 Future Outlook

The trend of the computational catalysis should follow the direction of modeling larger catalytic system. At current stage, the DFT calculations with GGA method can barely handle the system with more than 500 atoms. Which limits the computational model to simulate large and complex catalysts surfaces and clusters. Also, the AIMD method is inefficient compared to the classical molecular dynamic's methods. In the future, the machine learning techniques would assist the DFT and AIMD calculations by boosting the calculations speed by using machine learning predictions value rather than the first principle calculated values. However, when utilizing the machine learning models to predict the behaviors of chemical reactions or intrinsic properties of the catalyst materials, some researcher simply leveraged the fine-tuned models to do the predictions without understanding the physical meanings of these models. Such as the physical meanings of the weight parameters in the deep neural network (DNN). To unveil the ‘black box’ effect of the machine learning models, chemist and machine learning researchers are supposed to collaborated with each other to understand the physical meanings behind the parameters.